SPECTRAL AND TEMPORAL HARMONIC STUDIES OF LASER-PRODUCED PLASMAS.

by

Peter Duncan Carter

Thesis submitted in fulfilment of the requirements for the degree of Doctor of Philosophy in the University of London.

Royal Holloway College,
June 1980

Acknowledgement.

I wish to acknowledge the continual motivation and encouragement of my supervisor, Dr E R Wooding, throughout the course of this work, and the financial support of the Science Research Council together with the UKAEA Culham Laboratory, through Dr N J Peacock.

I am also deeply indebted to the entire staff of the Laser Division at the Rutherford Laboratory; for experimental time in a very heavy schedule, and for advice and encouragement. In particular, I owe thanks to Dr R G Evans, whose patience I must have tried on several occasions.

Finally, but in no way least, I thank my wife Margaret, for her exceptional tolerance and understanding during this time.

ABSTRACT

Studies of emission corresponding to the second ($2\omega_o$) and three-halves ($\frac{3}{2}\omega_o$) harmonics are reported from laser produced plasmas. These plasmas were produced by means of a neodymium laser with an irradiance up to 2.10^{16} $W.cm^{-2}$, in pulses of nominally 100ps duration. The spectral resolution of these harmonics from a range of targets has enabled various theories to be verified and the location of the interaction identified. A computer code has been used to account for refraction of the emerging radiation in the plasma density profile. The expansion velocity and temporal variation of this profile has also been taken into account. Temporal resolution of the $2\omega_o$ and $\frac{3}{2}\omega_o$ spectra has shown both harmonics to occur in pulses of less than the instrumental resolution limit which was ~10ps. This result gives some indication of the timescale for growth and saturation of parametrically excited instabilities.

Contents.

-Chapter 1-

1.1 Introduction

The ability of a high power laser beam to achieve spatial and temporal coherence of an electromagnetic wave at power densities greater than 10^{12} $W.cm^{-2}$ onto solid targets, thus forming high density, transient plasmas, has revealed a wide range of new physical phenomena. A solid target, exposed to an intense focussed laser beam, first ablates, and produces a plasma density profile extending from zero to solid density in a short distance. Further radiation incident on the plasma may then be absorbed up to the critical density region, and raises the temperature up to several hundred eV. Close to critical, remaining radiation may drive waves in the plasma which are then pumped parametrically until they are highly unstable. In particular, the potential of such a scheme to produce thermonuclear reactions by virtue of the Lawson criterion being exceeded[1-3] is under intensive study in several laboratories, such that the mechanisms responsible for absorption and scattering of laser light are of primary concern.[4-9] The observation of the harmonic frequencies of the incident laser light, which are generated by linear and non-linear mechanisms in the plasma corona, is essentially an energy loss to the system, but at the low conversion efficiencies experimentally determined, the characteristics of the radiated light offer a non-perturbing diagnostic technique, of electron temperature, density scalelength, bulk plasma motion, and the behaviour of excited waves. In this thesis, the observation of the second and

three-halves harmonics occuring from the interaction of a neodymium doped glass laser beam with solid targets at high intensities is reported, the relevance of each of these harmonics being that their generation is localised in the plasma density profile. In the case of $2\omega_o$ emission, this is the region in the profile close to the critical surface, where the laser frequency equals the local plasma frequency, and classical reflection takes place. In the case of the three-halves harmonic, this region in the density profile is less than a quarter of the critical density.

In Chapters 3 and 5 are developed the theories of generation of these two harmonics respectively, whilst Chapter 2 provides the background of material pertinent to the general scheme of laser plasma interaction. Chapter 4 describes the experimental arrangement and the results of experiments to observe and record $2\omega_o$ emission, with particular emphasis upon confirming theoretically observable features. The harmonic is situated in the optical region of the spectrum at 5320 Å. Of particular note is the extension of this work to include time resolution of the $2\omega_o$ spectrum, and the observation of phenomena occuring within the 10ps resolution of the streak camera / spectrograph system used. Chapter 6 deals likewise with the three-halves harmonic which was centred on 7093 Å, again with inclusion of work on the temporal dependence of the spectrum obtained from microballoon targets. Each of these Chapters also draws conclusions from the level of agreement between experiment and theory. Portions of the

experimental data however, are enhanced in accuracy somewhat by the use of computer simulations, primarily to provide values of critical and quarter critical expansion velocities, which can give rise to Doppler shifts of the observed spectra. These simulation studies involving computer techniques are recorded in Chapter 7, the overall interaction simulation being studied by use of a published 1-d computer code, after amendments relevant to the work in hand, whilst refraction of the observed light in the inhomogeneous plasma was treated by using a specific ray trace code.

Chapter 8 collates the independent conclusions drawn earlier and summarises the important features of the experimental data, with reference to the aforementioned theories.

The use of SI (MKS) units is followed where possible, but it is accepted that several non standard units command everyday usage, particularly in publications. Hence the use of the Ångstrom($1\mathring{A} = 10^{-10}$ m) for the unit of wavelength, and the electron Volt (1eV = 11594 $^{\circ}$K) for temperature.

Chapter 1 - References.

1. J Nuckolls, L Wood, A Thiessen & G Zimmerman, Nature, 239, 139, 1972

2. S Glasstone & R H Lovberg, 'Controlled Thermonuclear Reactions', D.van Nostrand Inc. 1960

3. D J Rose & M Clarke, 'Plasmas and Controlled Fusion', J Wiley Inc. 1961

4. J M Dawson, Phys. Fluids, 7, 7, 1964

5. N G Basov & O N Krokhin, Sov. Phys. JETP, 19, 123, 1964
   N G Basov et al, Engl. trans. JETP Lett. 8, 14, 1968

6. P K Kaw & J M Dawson, Phys. Fluids, 12, 12 1969

7. M N Rosenbluth & R Z Sagdeev, Comm. on Plasma Phys. & Contr. Fusion, 1, p129, 1972

8. K A Brueckner & S Jorna, Rev. Mod. Phys. 46, 2, 1974

9. K Boyer, 'Review of Laser-induced Fusion', - Paper presented at the APS meeting, Monterey, Calif. 1971

-Chapter 2-

Laser - plasma interaction.

2.1 In describing the mechanisms by which a high intensity laser beam interacts with plasma, a natural division occurs between linear and non-linear processes. The former, also known as classical absorption, may be described using fundamental hydrodynamics together with linear transport and absorption effects, and applies to the regime where the induced electron ('quiver') velocity due to the electric field of the laser beam is inferior to the electron thermal velocity. However, beyond the point where these two velocities are comparable the absorption becomes strongly non-linear and the so-called parametric instabilities are excited.[1,2] These are collective plasma effects which generate plasma waves of large amplitude, often besides re-radiating laser light at a different frequency. It is the properties of these waves which are of particular interest in the generation of second and three-halves harmonic frequencies of the incident light, and although actual generation mechanisms are examined in detail in Chapters 3 and 5 they are mentioned briefly in the latter half of this Chapter.

2.2 Collisional absorption

Collisional absorption is the process whereby an electromagnetic wave incident on a plasma causes the electrons to oscillate with increased velocity and then this momentum gained by the electrons is transferred to the ions upon collision. Since the actual scattering per electron-ion encounter is small due to

the effective long range Coulomb forces, and the collisions are many, an assessment of this absorption may be made by assuming one parameter for momentum transfer, the electron-ion collision frequency, ν_{ei}. Using this, the force acting on a single electron in an electric field $\underline{E}$ may be represented by

$$\underline{F} = m_e \frac{d\underline{v}}{dt} = -e\underline{E} - m_e \underline{v}_e \nu_{ei} \qquad - 2.2.1$$

where m_e, v_e, and e are the electron mass, thermal velocity and charge respectively.

Using Maxwell's equations to develop a generalised wave equation for a plasma, as shown in Appendix A, an expression for the complex refractive index of the plasma may be obtained. This is the ratio of the velocity of light in vacuo to the phase velocity of a propagating wave; v_{ph}. i.e.

$$v_{ph} = \frac{\omega}{|k|}$$

where k = complex propagation vector; and if the complex refractive index, μ_c, is given by:

$$\mu_c = (\mu + iK)^2$$

then the real part is a real refractive index and the imaginary part an absorption index. Thus

$$\mu_{real} = \frac{c}{\omega} Re.(k)$$

$$K = \frac{c}{\omega} Im.(k)$$

In determining an expression for the spatial absorption of an electromagnetic wave in a plasma, the linear absorption coefficient (k_a) may be defined by :

$$\frac{dI_\omega}{dz} = -k_a I_\omega \qquad -2.2.2.$$

where I_ω = the spectral intensity of the wave travelling in the z direction. As intensity is proportional to the square of the amplitude, then

$$k_a = -2.\mathrm{Im.}(k) = -2\frac{\omega}{c}K \qquad -2.2.3.$$

The dielectric constant (ε_t) of the medium for transverse waves is given by (as in Appendix A)

$$\mu_c^2 = \varepsilon_t$$

$$(\mu + iK)^2 = \varepsilon_t$$

$$\mu^2 - K^2 = \mathrm{Re.}(\varepsilon_t)$$

$$-2\mu K = \mathrm{Im.}(\varepsilon_t) \qquad -2.2.4.$$

Combining 2.2.3 and 2.2.4

$$k_a = \frac{\omega}{\mu c}\mathrm{Im.}(\varepsilon_t) \qquad -2.2.5.$$

To determine the imaginary part of this dielectric constant, a primary assumption is that the contribution of the ion motion is negligible. (Lorentz plasma). Thus

$$\underline{J} = -n_e e \underline{v}_e$$

where $\underline{J}$ = current density. The only electron velocity is that due to the applied electromagnetic wave, so using 2.2.1 with a general wave,

$$\underline{E} = \underline{E}_o(\exp(i[\omega t - \underline{k}\underline{r}]))$$

gives $\underline{J} = n_e e \underline{v}_e = \dfrac{n_e e^2 \underline{E}}{m_e(\nu_{ei} + i\omega)} = \sigma \underline{E}$ - 2.2.6.

where σ = conductivity. If however, wave damping is ignored, then eqn. 2.2.1 becomes

$$m \frac{d\underline{v}_e}{dt} = -e\underline{E}$$

then

$$\underline{J} = \frac{n_e e^2}{m_e i\omega} \underline{E} = \sigma \underline{E}$$

The dielectric constant is related to the conductivity by

$$\varepsilon_r = 1 - \frac{\sigma}{i m_e \omega} \qquad - 2.2.7.$$

so that in this case

$$\varepsilon_r = (1 - \frac{\omega_{pe}^2}{\omega^2}) \qquad \text{where} \qquad \omega_{pe} = \frac{n_e e^2}{\varepsilon_o m_e}$$

and ε_o = the permittivity of free space. Here, ω_{pe} is known as the electron plasma frequency, an important parameter which is the natural undamped frequency of oscillation resulting from charge neutrality. Thus classically, electromagnetic wave propagation is forbidden if the wave angular frequency is greater than the plasma frequency, and the wave is reflected. In an inhomogeneous plasma the electron density corresponding to the boundary where $\omega_{pe} = \omega_o$ is known as the critical density, and for a neodymium laser this corresponds to $9.93\ 10^{20}$ particles per cm^{-3}.

The dispersion relation for a transverse wave in a cold plasma is

$$k^2 c^2 = \omega^2 \varepsilon_t$$

as shown from the general wave equation, (Appendix A), and substituting for ε_t from 2.2.6 and 2.2.7 leads to the expression for the propagation vector as

$$k = \frac{1}{c^2}\left(\omega^2 - \frac{\omega^2 \omega_{pe}^2}{(\nu_{ei}^2 + \omega^2)} - \frac{i\omega\,\omega_{pe}^2\,\nu_{ei}}{(\nu_{ei}^2 + \omega^2)}\right) \qquad - 2.2.8.$$

So a real refractive index and an absorption index can be obtained from the real and imaginary terms and are as below.

$$\mu = \left[\frac{1}{2}\left(1 - \frac{\omega_{pe}^2}{\nu_{ei}^2 + \omega^2}\right) + \frac{1}{2}\left[\left(1 - \frac{\omega_{pe}^2}{\nu_{ei}^2 + \omega^2}\right)^2 + \left(\frac{\omega_{pe}^2}{\nu_{ei}^2 + \omega^2}\,\frac{\nu_{ei}}{\omega}\right)^2\right]^{1/2}\right]^{1/2}$$

and

$$k_a = \frac{\nu_{ei}}{\mu c}\,\frac{\omega_{pe}^2}{(\nu_{ei}^2 + \omega^2)} \qquad - 2.2.9.$$

The real refractive index may be approximated at frequencies well above the plasma frequency, and for the condition $\nu_{ei} << \omega^2 - \omega_{pe}^2$ to give

$$\mu \simeq \left(1 - \frac{\omega_{pe}^2}{\omega^2}\right) \qquad - 2.2.10.$$

The expression for the absorption coefficient assumes that the collision frequency is velocity independent. In practice this is not so and more accurate expressions for absorption use the quantum-mechanical approach of inverse bremsstrahlung where absorption by an electron takes place in the vicinity of an ionic field. This will involve integration of the energy absorbed per

electron over the electron distribution function and the period of the laser beam, assuming that T_e > 10 eV so that electron-ion inverse bremsstrahlung is the only significant absorption mechanism. Several authors have derived similar expressions[4-9], a recent one by Pert[9] being quoted here. (for the high field case)

$$k_a = \frac{n_e n_i e^3 Z^2 \nu}{4\pi^2 (\varepsilon_0 E)^3} \left(\ln\left(\frac{m u_o^2}{2 k_B T_e}\right) \ln\left(\frac{4 (8 k_B T_e)^3 (\varepsilon_0 \pi)^4}{Z^2 \omega^2 e^4 m}\right)\right)$$

where u_o = the amplitude of the 'quiver velocity' = $\frac{eE_o}{m\omega^2}$

A simple calculation may be carried out to estimate the total classical absorption by a plasma due to a normally incident laser beam on to a density gradient of the form

$$n_e = n_{cr}\left(1 + \frac{z}{L_n}\right)$$

where n_e is the critical density, and L_n is the distance between the points where the electron density rises from zero to critical. From 2.2.2 , the transmitted intensity of a general wave through a plasma is:

$$I_t = I_o \exp - \int_o^s k_a \, ds$$

where s is the ray path, and $I_t = I_o - I_{abs}$ = transmitted intensity.

$$\therefore \quad I_t = I_o \exp \frac{2\nu_{ei}}{c} \int_{-L}^{o} \frac{(1 + z/L_n)^2}{(z/L)^{1/2}} \, dz$$

after using expressions 2.2.9 and 2.2.10, the subscript 'cr' denoting parameters at the critical surface. Therefore ——

$$I_{abs} = I_o \left(1 - \exp\left(-\frac{32}{15} L_n c \nu_{cr}\right)\right) \qquad 2.2.11.$$

where c is the velocity of light in vacuo.

As the collision frequency is temperature dependent, an assessment can be made of the fall in classical absorption as the plasma gets hotter. The minimum temperature the plasma must reach in order not to get any hotter is when the energy input from the laser is balanced by the limit on the thermal conduction, the maximum for this being known as the 'free streaming limit'. Essentially, this limit is derived from kinetic theory considerations which show that the maximum electron flux across a boundary is $0.25\, n_e \bar{v}_e$, and each of these has an energy of $2 k_B T_e$. In practice, a return flux, Q, must exist to prevent an accumulation of particles, this being:[10]

$$Q_{max} = \frac{1}{32} n_e m_e v_{hot}^3$$

The return particles do work in colliding, which appears as heat, this being due to the space-charge field derived from the 'hot' electrons leaving the absorption zone driving the cold electrons against a collisional resistance. 'Hot', or suprathermal electrons with temperatures well in excess of thermal, are a feature of the heating of plasmas by resonant absorption and also parametric processes, as described later. This is because the large amplitude electron plasma waves produced by these mechanisms accelerate particles out to their phase velocity and the non-Maxwellian energy distribution which follows has a

suprathermal component, as determined from X-ray spectra, and from microwave experiments .

To take this into account a lengthy analysis is necessary, but in simple terms a flux limiting factor is used. The thermal conduction equation, $Q = -K_e \nabla T_e$

becomes $$Q_{max} = f\, n_e\, v_e\, k_B\, T_e \qquad 2.2.12.$$

where f is the flux limiting constant. This limit is attributed to ion acoustic turbulence enhancing the resistance of the return flux, and results in experimental values of $f \sim 0.03$.[11] A theoretical estimate may be made after adopting Spitzer's expression for the collision frequency:[12]

$$\nu_{ei} = \frac{\omega_{pe}}{2\pi n_e} \frac{\ln \Lambda}{\lambda_D}$$

There is no net accumulation of electronic charge over a distance greater than the Debye length, λ_D, where

$$\lambda_D = \sqrt{\frac{\varepsilon_0 k_B T_e}{n_e e^2}}$$

Thus ν_{ei} at the critical surface is given by :

$$\nu_{cr} = \frac{\omega_0 n_{cr}^{1/2} e^3 \ln \Lambda}{2\pi \varepsilon_0^{3/2} (k_B T_e)^{3/2}}$$

Therefore $$\frac{1}{(k_B T_e)^{3/2}} \times \text{constant}, \simeq \frac{\nu_{cr}}{\omega_0} \qquad 2.2.13.$$

As expression 2.2.12 is assumed equal to the rate of absorbed energy (I_{abs}), combining 2.2.11, 2.2.12 and 2.2.13 gives

$$\frac{I_{abs}}{I_o} = 1 - \left(\exp - \left(\frac{32}{15} k_b L_n \times \frac{\text{constant}}{I_{abs}}\right)\right) \qquad 2.2.14.$$

which shows the absorbed fraction to be independent of plasma temperature, in a simple approximation. Inserting numerical values of constants, a graphical plot of the absorbed fraction for increasing intensity is shown in Fig. 2.2.1(a), for the free streaming limit as the maximum limit on thermal conduction. Reducing this to a 3% thermal flux limit shows the absorption to fall for lower intensities, as shown in Fig. 2.2.1(b). Although gross simplifications have been employed, it can be seen that classical absorption makes a diminishing contribution to absorption as the laser intensities increase beyond 10^{12} W.cm^{-2}. This absorption may be increased slightly by an increase in target atomic number, which also increases radiation losses due to bremsstrahlung, but at these intensities other processes become dominant.

2.3 Resonant Absorption

If the incident laser beam is inclined at an angle θ to the plasma density gradient, classical reflection, or a turning point is reached at the plane where the dielectric constant is equal to $\sin^2\theta$.

i.e. $\varepsilon = \sin^2\theta = 1 - \frac{\omega_{pe}^2(z)}{\omega^2}$, $\therefore$ $n_{e(T.P.)} = n_{cr}\cos^2\theta$.

The modulus of the electric field up to this point, for a linear ramp, has been shown to exhibit an Airy function form[13,14], as in

Fig. 2.2.1

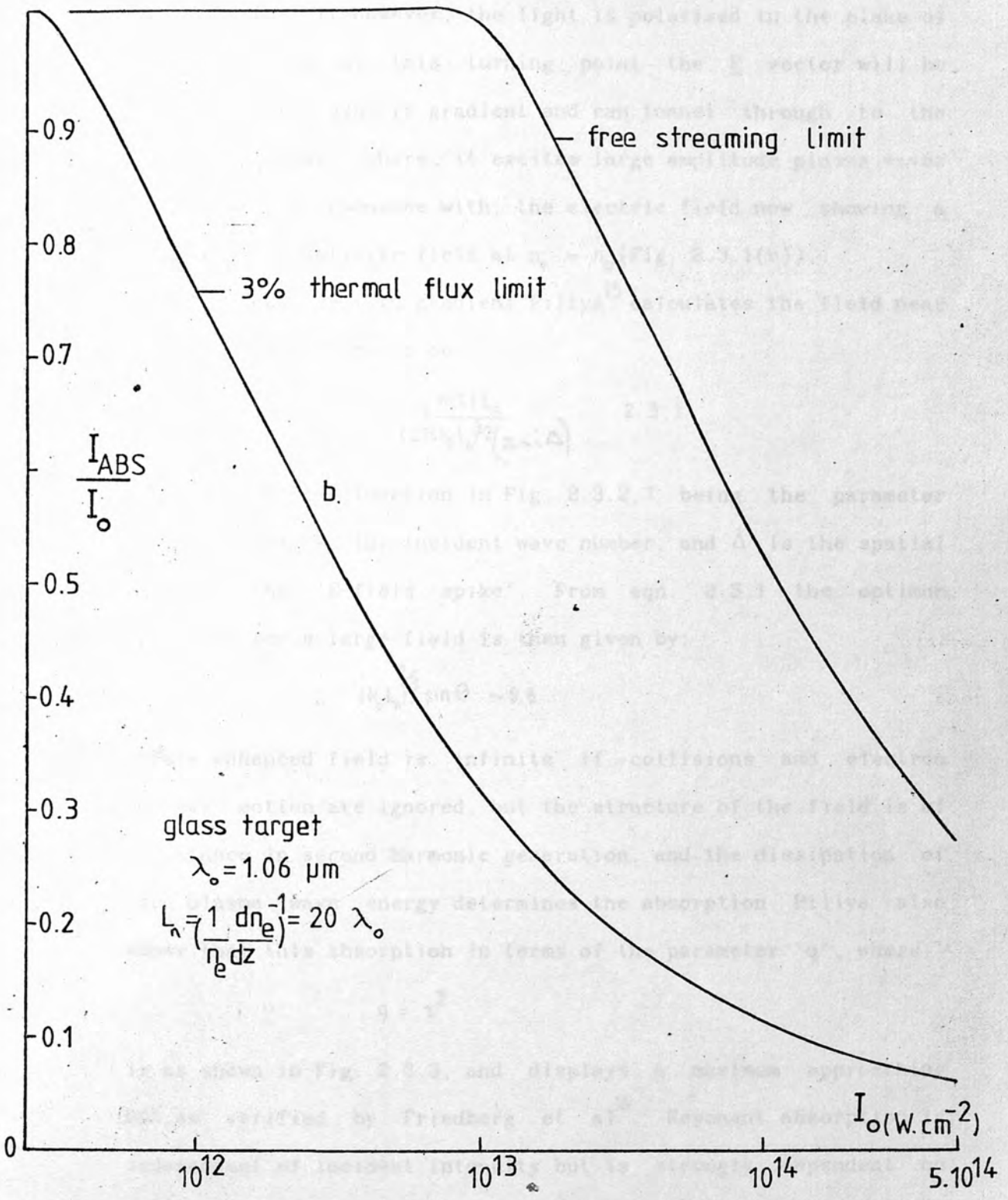

absorption efficiency v. irradiance

(classical maximum)

Fig. 2.3.1(a). If however, the light is polarised in the plane of incidence then at this turning point the $\underline{E}$ vector will be parallel to the density gradient and can tunnel through to the critical surface where it excites large amplitude plasma waves which it is in resonance with; the electric field now showing a theoretically infinite field at $n_e = n_{cr}$ (Fig. 2.3.1(b)).

For a linear density gradient Piliya[15] calculates the field near the critical surface to be:

$$E(z) = \frac{E_o \phi(\tau) L_n}{(2\pi k_o L_n)^{1/2}(z + i\Delta)} \qquad 2.3.1$$

where $\phi(\tau)$ is the function in Fig. 2.3.2, τ being the parameter $(k_o L_n)^{1/3} \sin\theta$, k_o the incident wave number, and Δ is the spatial extent of the 'E-field spike'. From eqn. 2.3.1 the optimum condition for a large field is then given by:

$$(k_o L_n)^{1/3} \cdot \sin\theta \sim 0.8$$

This enhanced field is infinite if collisions and electron thermal motion are ignored, but the structure of the field is of importance in second harmonic generation, and the dissipation of the plasma wave energy determines the absorption. Piliya also shows that this absorption in terms of the parameter 'q', where

$$q = \tau^2$$

is as shown in Fig. 2.3.3, and displays a maximum approaching 50%, as verified by Friedberg et al[16]. Resonant absorption is independent of incident intensity but is strongly dependent on scalelength, and its effect may be less at very high intensities

Fig. 2.3.1

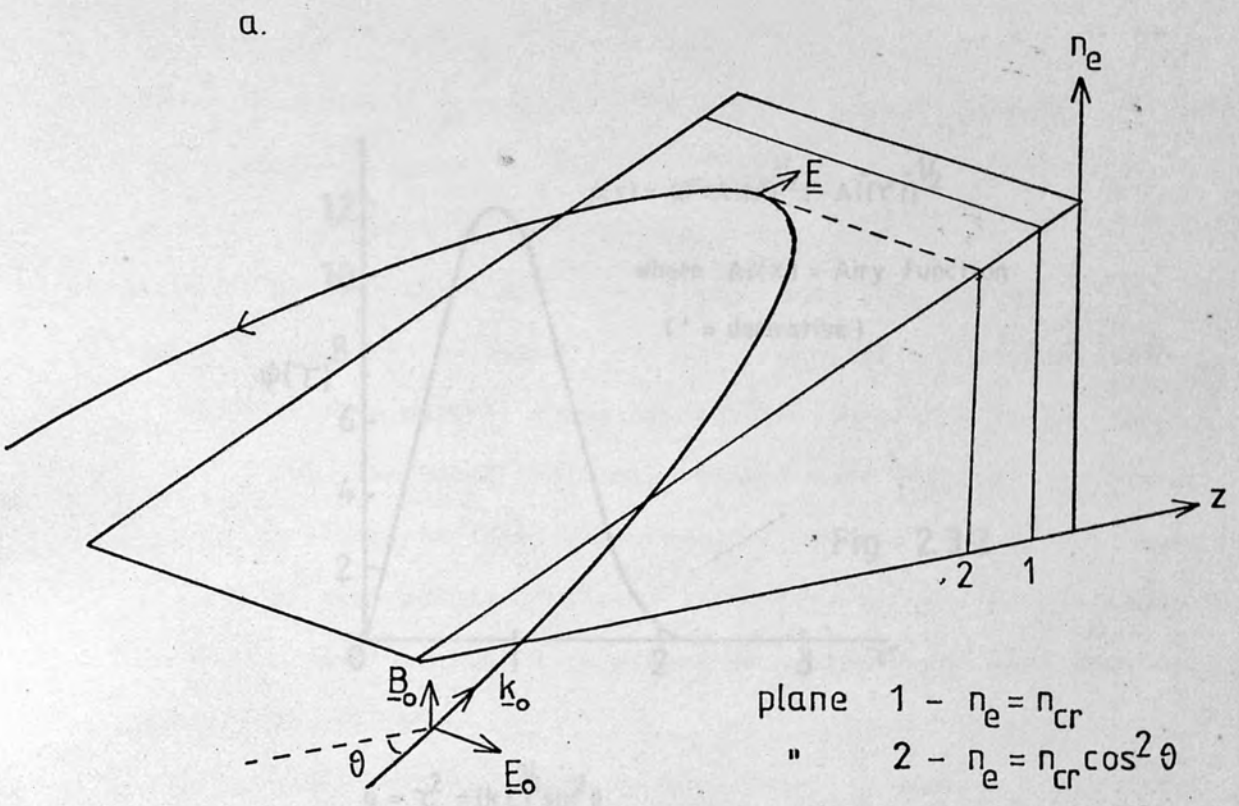

plane 1 – $n_e = n_{cr}$

" 2 – $n_e = n_{cr} \cos^2 \theta$

$n_e(z) = n_{cr}(1 + z/L)$

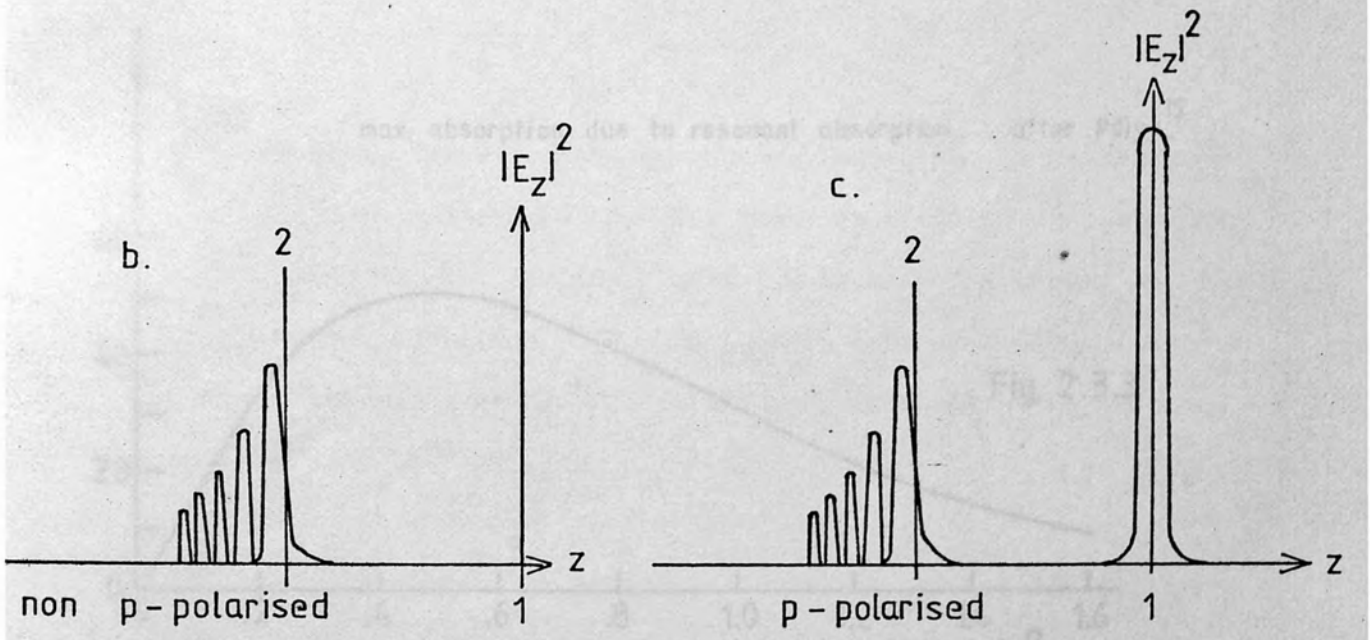

resonant absorption E-field enhancement at $n_e = n_{cr}$.

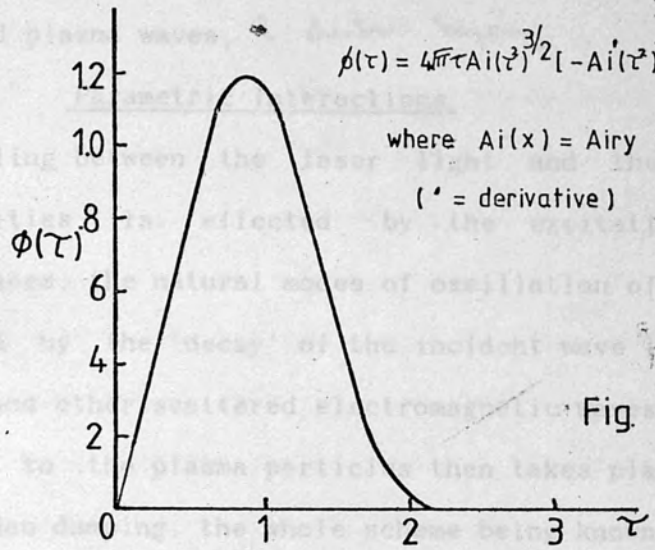

Fig. 2.3.2

$$q = \tau^2 = (k_o L_n)^{2/3} \sin^2\theta$$

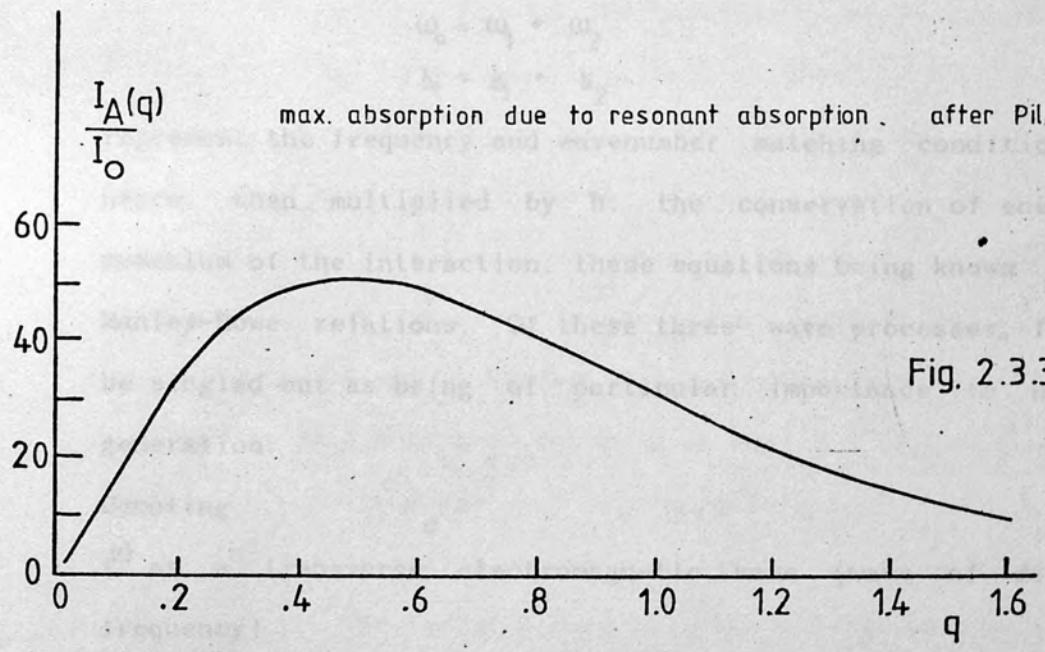

Fig. 2.3.3

where collective effects are present. This however is only valid for convective, collisional and weak Landau damping of the excited plasma waves, & electron trapping

2.4 Parametric Interactions.

Coupling between the laser light and the plasma at high intensities is effected by the excitation of parametric resonances, the natural modes of oscillation of the plasma being excited by the 'decay' of the incident wave into various plasma waves and other scattered electromagnetic waves. Tranfer of wave energy to the plasma particles then takes place via collisional or Landau damping, the whole scheme being known as anomalous or non-linear absorption.

Of interest primarily are the three-wave processes such that the laser ('pump') wave $(\omega_o, \underline{k}_o)$ decays into two product waves $(\omega_1, \underline{k}_1)$ and $(\omega_2, \underline{k}_2)$. Thus

$$\omega_o = \omega_1 + \omega_2$$
$$\underline{k}_o = \underline{k}_1 + \underline{k}_2$$

represent the frequency and wavenumber matching conditions and hence, when multiplied by $\hbar$, the conservation of energy and momentum of the interaction; these equations being known as the Manley-Rowe relations. Of these three- wave processes, four may be singled out as being of particular importance to harmonic generation.

Denoting

$t^{(\prime)}$ as a transverse electromagnetic wave (wave of different frequency),

ℓ as an electron plasma wave (electrostatic), and

s as an ion acoustic wave (acoustic)

these are

1	$t \rightarrow \ell + s$	Parametric Decay Instability
2	$t \rightarrow \ell + \ell$	Two-Plasmon Instability
3	$t \rightarrow t' + \ell$	Stimulated Raman Scattering (SRS)
4	$t \rightarrow t' + s$	Stimulated Brillouin Scattering (SBS)

The latter two mechanisms represent an energy loss to the interaction region due to the scattered wave, and need to be controlled if optimum energy coupling to the plasma is envisaged, particularly SBS. Parametric instabilities in general are characterised by a threshold pump intensity, exponential growth from noise, a directional dependence of the scattered wave(s), and a finite region of interaction. For the parametric decay instability and SBS this corresponds to a region just prior to the critical surface, and for the two-plasmon decay and SRS this is the region up to quarter- critical, as shown in Fig. 2.4.1.

Theoretical studies of parametric instability using different approaches have been made by several authors[17-27]. Of note, Nishikawa[18] has developed the coupled equations for electron plasma and ion acoustic waves using hydrodynamic methods, including the effect of Landau damping. However, most of the studies to date have been based on an analysis of the linearised dispersion relations where no allowance is made for spatial gain. Hence the instabilities cannot properly be described as absolute or convective. The former occurs when the wave grows at a fixed

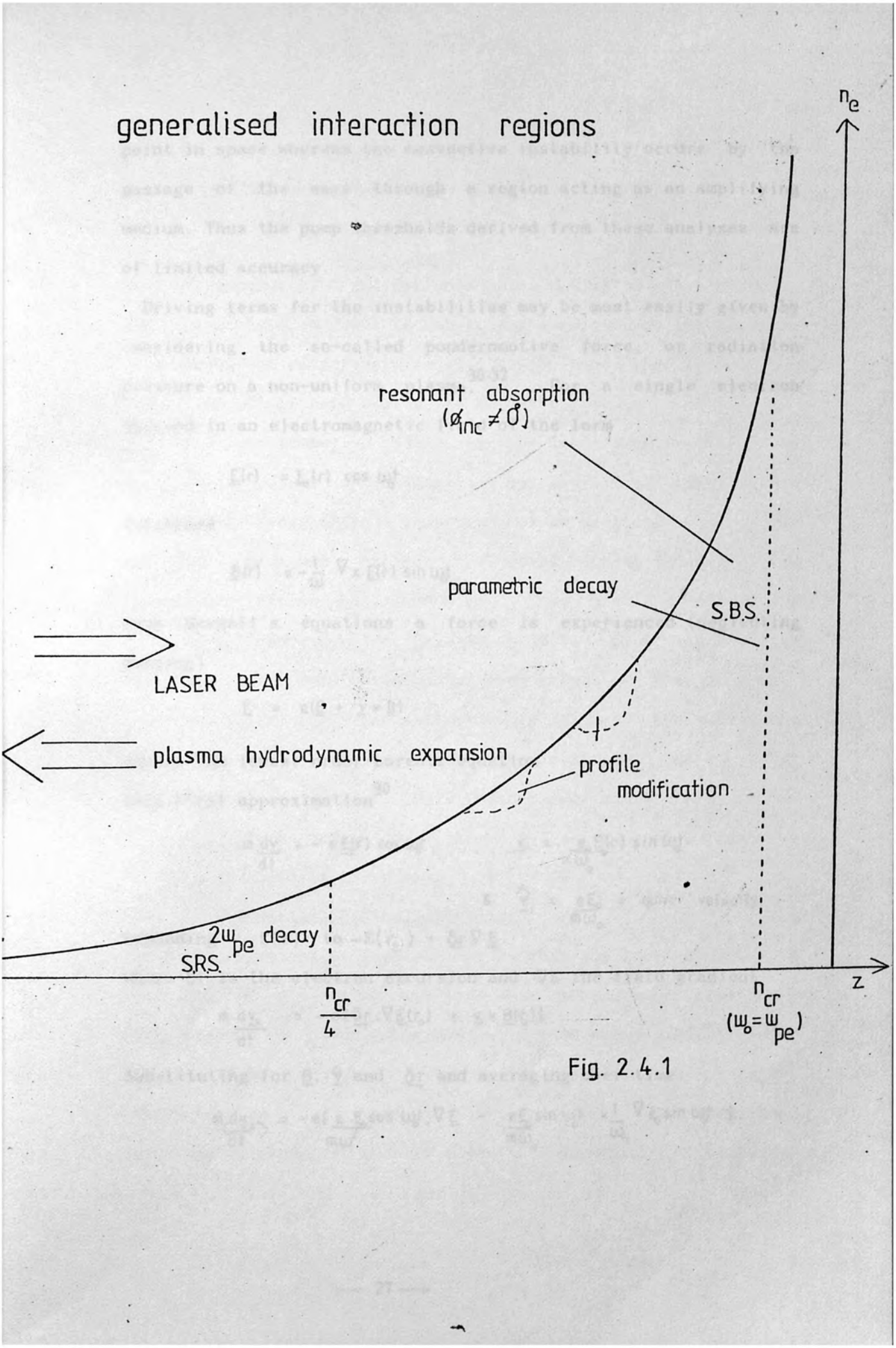
generalised interaction regions
n_e
resonant absorption
($\phi_{inc} \neq 0$)
parametric decay
S.B.S.
LASER BEAM
plasma hydrodynamic expansion
profile
modification
$2\omega_{pe}$ decay
S.R.S.
$\frac{n_{cr}}{4}$
n_{cr}
($\omega_o = \omega_{pe}$)
z

Fig. 2.4.1

point in space whereas the convective instability occurs by the passage of the wave through a region acting as an amplifying medium. Thus the pump thresholds derived from these analyses are of limited accuracy.

Driving terms for the instabilities may be most easily given by considering the so-called ponderomotive force, or radiation pressure on a non-uniform plasma,[30-32] . For a single electron imposed in an electromagnetic field of the form

$$\underline{E}(r) = \underline{E}_0(r) \cos \omega_0 t$$

Therefore

$$\underline{B}(r) = -\frac{1}{\omega} \nabla \times \underline{E}(r) \sin \omega_0 t$$

from Maxwell's equations a force is experienced, (neglecting damping)

$$\underline{F} = e(\underline{E} + \underline{v} \times \underline{B})$$

due to the lowest order Lorentz equation

To a first approximation[30]

$$m \frac{d\underline{v}_1}{dt} = - e \underline{E}_0(r) \cos \omega_0 t , \quad \therefore \quad \underline{v}_1 = \frac{e}{m\omega_0} \underline{E}_0(r) \sin \omega_0 t$$

$$\& \quad \hat{\underline{v}}_1 = \frac{eE_0}{m\omega_0} = \text{'quiver' velocity}$$

Expanding $E(r)$ to $\sim E(r_0) + \delta r \nabla \underline{E}$

where δr is the electron excursion and ∇E the field gradient

$$m \frac{d\underline{v}_2}{dt} = - e [\delta \underline{r} . \nabla \underline{E}(r_0) + \underline{v}_1 \times \underline{B}(r_0)]$$

Substituting for $\underline{B}$, $\underline{v}$ and $\delta \underline{r}$ and averaging over time:

$$m \left\langle \frac{d\underline{v}_2}{dt} \right\rangle = -e \left[\frac{e \underline{E}_0}{m\omega^2} \cos \omega_0 t . \nabla \underline{E} - \frac{e\underline{E}_0}{m\omega_0} \sin \omega_0 t \times \frac{1}{\omega_0} \nabla \underline{E}_0 \sin \omega_0 t \right]$$

$$\therefore \quad m\frac{d\underline{v}}{dt} = \frac{e^2}{2m\omega^2}(\underline{E}_o.\nabla\underline{E}_o + \underline{E}_o \times \nabla \times \underline{E}_o) \qquad 2.4.1.$$

This corresponds to a net non-zero force acting on the electrons. The first term in 2.4.1 is due to the excursion of the electron into regions of differing electric field, and the second the distortion of the path due to the magnetic field.

As the ponderomotive force is the manifestation of the radiation pressure on a plasma, it may explain the modification of the density due to this pressure. For an Nd-glass laser, the radiation pressure exceeds the local plasma pressure for intensities greater than $\sim 10^{16} W.cm^{-2}$. This has the effect of severely disturbing the density profile, producing density depressions with substantial local steepening of the gradient. This behaviour in turn will strongly influence the subsequent absorption of laser light and experiments to date using interferometric methods[33-35] have determined density profiles at different times during the laser pulse, and show positive evidence for profile steepening.

2.5 Stimulated Compton Scattering

A furthur process of interest occurs when the incident wave is scattered by an electron such that when the scattered wave has a frequency and direction coincident with a second incident beam, the scattering will be stimulated. The scattering rate into the second beam is proportional to the product of the two beam intensities, and the energy difference on going from beam 1 to

beam 2 at a lower frequency is given to the scattering electron. This process is known as Stimulated Compton Scattering and its effect could be apparent in an incident converging beam of finite bandwidth. Its existence has been deduced from experiment by Decroisette et al[37] who determined a small red-shifted sideband on the spectral profile of a laser beam transmitted through a plasma.

Chapter 2 - References.

1.K A Brueckner & S Jorna, Rev. Mod. Phys, 46, 2, 1974

2.T P Hughes, 'Plasmas & Laser Light', Adam Hilger London 1975.

3.J M Dawson, Phys. Fluids, 7, 7, 1964

4.T W Johnston & J M Dawson, Phys. Fluids, 16, 5, 1973

5.K W Billman & J R Stallcop, Appl. Phys. Letts, 28, p704, 1976

6.S Rand, Phys. Rev. B, 136, p231, 1964

7.H Brehme, Phys. Rev. C, 3, p337, 1971

8.R K Osborn, Phys.Rev. A, 5, p1660, 1972

9.G J Pert, J. Phys. B, 8, 18, 1975, and 9, 3, 1976 - J. Phys. A

10.R L Morse & C W Nielson, Phys. Fluids, 16, p909, 1973

11.D R Gray, J D Kilkenny, M S White, P Blyth & D Hull, Phys. Rev. Letts, 39, 20, 1977

12. L Spitzer, 'Physics of fully Ionised Gases', J Wiley (Interscience) London 1962

13. N G Denisov, Zh. Eksp. Teor. Fiz, 31, p609, 1956

14. V L Ginzburg, 'Propagation of e-m waves in plasma', North Holland 1970

15. A D Piliya, Sov. Phys. Tech. Phys, 11, p609, 1966

16. J P Friedberg, R W Mitchell, R L Morse & L I Rudsinski, Phys. Rev. Letts, 28, 13, 1972

17. V P Silin, Sov. Phys. JETP, 21, 6, 1965

18. K Nishikawa, J. Phys. Soc Japan, 24, p926 & 1152, 1968

19. D F DuBois & M V Goldman, Phys. Rev. 164, 1, 1967

20. E A Jackson, Phys. Rev. 153, p235, 1967

21. J R Sanmartin, Phys. Fluids, 13, p1533, 1970

22. F W Perkins & J Flick, Phys. Fluids, 14, 9, 1971

23. M N Rosenbluth, Phys. Rev. Letts, 29, p565, 1972

24. M N Rosenbluth & R Z Sagdeev, Comm. Plasma Phys. & Contr. Fusion, 1, p129, 1972

25. D Pesme, G Laval & R Pellat, Phys. Rev. Letts, 31, 4, 1973

26. A A Galeev & R Z Sagdeev, Nucl. Fusion, 13, p603, 1973

27. D W Forslund, J M Kindel & E L Lindman, Phys. Fluids, 18, 8, 1975

28. V P Silin & A N Starodub, Sov. J. Plasma Phys, 3, 2, 1977

29. V Fuchs & G Beaudry, Phys. Fluids, 21, 2, 1978

30. F F Chen, in 'Laser Interaction with Matter' ed Schwarz & Hora, Vol 3a 1973

31. M R Siegrist, Opt. Comm, 16, p407, 1976

32. M R Siegrist, J. Appl. Phys, 48, 3, 1977

33. R Fedosejevs, I V Tomov, N H Burnett, G D Enright & M C Richardson, Phys. Rev. Letts, 39, 15, 1977

34. D T Attwood et al, Phys. Rev. Letts, 40, p184, 1978

35. A Raven, O Willi & P T Rumsby, Phys. Rev. Letts, 41, 8, 1978

36. H Dreicer, Phys. Fluids, 7, p735, 1964

37. M Decroisette, J Peyraud & G Piar, Phys. Rev. A, 5, 3, 1972

-Chapter 3-

The theory of second harmonic generation.

3.1 Second harmonic generation in laser produced and laser heated plasmas is associated with the coalescence of two waves, being either the incident laser or an electron plasma wave generated by the incident laser. Constraints on this are due to frequency and wavenumber matching and therefore in an isotropic, homogeneous plasma, the recombination of two transverse (e-m.) waves is forbidden. The permitted schemes are either an incident wave with a plasma wave, or two plasma waves, viz.

$$\ell + t \rightarrow t' \qquad \underline{k}^{t}(\omega) + \underline{k}^{t}(\omega) \rightarrow \underline{k}^{t}(2\omega)$$

$$\ell + \ell \rightarrow t' \qquad 2\times\underline{k}^{\ell}(\omega) \rightarrow \underline{k}^{t}(2\omega)$$

t and ℓ referring to transverse and longitudinal waves respectively. In an inhomogeneous plasma the matching conditions are only satisfied in well-defined regions dependent on the plasma density.

Since the formation of electron plasma waves at a frequency approximating the laser frequency is a fundamental process in $2\omega_o$ generation, the mechanisms for generating these are described. A threshold exists for the onset of parametric instability so that again different processes may be categorised as linear or non-linear, the former being explained using a geometric optics approach of the linear wave equation, the latter described by several methods. Fundamental differences in expected $2\omega_o$ emission result from the two regimes, and an analysis of both here aims to pinpoint these differences where they are experimentally

observable.

3.2 $2\omega_o$ generation due to linear transformation

In Chapter 2 it was shown that p-polarised light incident obliquely on a linear plasma density gradient has an E-field singularity centred on the critical surface although the turning point is at a distance $-L_n \sin^2\theta$ from the surface. Here, L_n is the distance in which the density rises from zero to critical and is the angle between the initial incident beam and the normal to the gradient. This is shown diagrammatically in Figs 2.3.1(a & b). This E-field at the critical surface is theoretically infinite in the absence of electron thermal motion or collisions[1]. The actual structure that this field adopts is important in determining the non-linear source terms for the field equations of the second harmonic wave, and this structure has been determined by several authors. Amongst them, Vinogradov and Pustuvalov[2] have developed the field structure using the assumption that the major factor limiting this field is the electron thermal motion such that

$$\frac{\nu_{ei}}{\omega_o} << \left[\frac{\beta c}{L_n \omega_o}\right]^{2/3}$$

where ν_{ei} is the electron-ion collision frequency, and

$$\beta^2 = \frac{3 v_{th}}{c}$$

Alternatively, Erokhin et al[3] have found the field structure when the dominant factor in limiting the field is electron-ion collisions. The general wave equation used in both approaches is developed from Maxwell's equations as shown in Appendix A, and is

of the form:

$$\nabla^2 \underline{E} + \nabla(\nabla . \underline{E}) - (\frac{\omega}{c})^2 \varepsilon . \underline{E} = 0 \qquad 3.2.1.$$

where ε is the dielectric constant.

If $\underline{E}$ is a function of one dimension only, then equation 3.2.1 reduces to a simpler form for which several solutions have been found.

$$\frac{d^2 \underline{E}}{dz^2} + \frac{\omega^2}{c^2} \varepsilon . \underline{E} = 0 \qquad 3.2.2.$$

However, for oblique incidence a general equation for p-polarised light in the y-z plane incident originally at an angle Θ to the density gradient in the z-plane is of the form

$$\frac{d^2 G}{dz^2} - \frac{1}{\varepsilon(z)} \frac{d\varepsilon(z)}{dz} \frac{dG}{dz} + \frac{\omega^2}{c^2} (\varepsilon(z) - \sin^2\Theta) G = 0 \qquad 3.2.3.$$

where the magnetic field

$$H_x = G(z) \exp[i(\omega t - \frac{\omega}{c} \sin\Theta \, y)]$$

such that the electric field vectors in both the y and z directions may be obtained from the relations:

$$E_y = \frac{-ic}{\omega \varepsilon(z)} \frac{dH_x}{dz} \qquad E_z = \frac{+ic}{\omega \varepsilon(z)} \frac{dH_x}{dy}$$

Solutions of equation 3.2.3 for the linear density gradient have been extensively studied by Denisov[4], and an approximate value for the enhanced electric field at the critical surface (z=0) is, including collisional damping:

$$E_z(0) = \sqrt{\frac{2c}{\pi \omega_0 L_n}} \frac{e^{-\frac{2}{3} \omega_0 L_n \sin^3\Theta}}{\frac{\nu_{ei}}{\omega_0}}$$

where the angle of incidence is not small, or too large such that

the turning point is a large distance from the critical surface.

Having shown the existence of a finite electric field in the critical surface region due to the incident laser light, the co-existence of electron plasma waves (assuming ion immobility) can also be shown to be driven by the enhanced electric field.

Again from Appendix A

$$\nabla.(\varepsilon.\underline{E}) = 0$$

$$\therefore \quad \underline{E}(\nabla\varepsilon) + \varepsilon\,\nabla.\underline{E} = 0$$

which in the z-dimension becomes

$$E_z \frac{d\varepsilon}{dz} + \varepsilon \nabla.\underline{E} = 0$$

$$\therefore \quad \nabla.E = \frac{-E_z \frac{d\varepsilon}{dz}}{\varepsilon} = \frac{\rho_q}{\varepsilon_0}$$

where ρ_q = charge density = $e\,\Delta n_e$ with Δn_e the density perturbation from equilibrium. For non-normal incidence $E_z \neq 0$ and $\frac{d\varepsilon}{dz} \neq 0$ as the plasma is inhomogeneous in the z-direction.

Hence the charges $\bar{\rho}$ appear in the electromagnetic wave and at $\varepsilon = 0$, the density of these charges varies with the plasma frequency, an electromagnetic wave approaching this point giving rise to plasma oscillations increasing in amplitude. These oscillations are not independent, as taking thermal motion into account energy is transferred to neighbouring regions and this process corresponds to an electron plasma wave.

Ultimately, collisions will result in a calculable portion of this wave energy being dissipated, so that the whole process is

an absorption mechanism, but the approximations used in determining the electric field structure and subsequent energy dissipation are important in assessing the characteristics of the produced plasma waves which possess a frequency closely matching the laser frequency. It is these waves which may recombine to form observable $2\omega_o$ emission.

3.3 Recombination of linearly generated plasma waves.

As noted previously, the only two permissible schemes for the recombination of these longitudinal electron plasma waves and the incident wave are:

$$\ell + \ell \rightarrow t'$$
$$\ell + t \rightarrow t'$$

For wavenumber and frequency matching of these two conditions in inhomogeneous plasma, a z-dependence is introduced of the region in which these criteria are satisfied. From the dispersion relations of the interacting waves, the equation of wavenumber matching can yield the approximate position in the density profile where recombination takes place.

a. $\ell + t \rightarrow t$.

If $\varepsilon(\omega_o)$ is the dielectric constant at the recombination plane then

$$\varepsilon(\omega_o) = 1 - \frac{n_e(z)}{n_{cr}} \qquad \text{and} \qquad \varepsilon(2\omega_o) = 1 - \frac{n_e(z)}{4\,n_{cr}}$$

and the wavenumber matching is... (± denoting the wave direction)

Taking the relevant dispersion relations into account

$$\pm\left(\varepsilon(\omega_o) - \sin^2(\theta)\right)^{1/2} - \frac{1}{\beta}(\varepsilon(\omega_o)) = -2(\varepsilon(2\omega_o) - \sin^2\theta)^{1/2}.$$

then this reduces to:

$$(\varepsilon(\omega_o)^{1/2} = 2\beta(\varepsilon(2\omega_o) - \sin^2\theta)^{1/2} .$$

if $\sin^2\theta << 1$ and $\beta << 1$.

Therefore the plane where

$$\Delta z = -3L_n\beta^2 \qquad - \quad 3.3.1$$

if $n_e = n_{cr}(1 + z/L_n)$; and Δz is the distance between the critical surface and the plane of recombination.

b. $\ell + \ell \rightarrow t$.

Similarly the wavenumber matching for this mechanism gives:

$$-2(\varepsilon(\omega_o))^{1/2} = -2\beta(\varepsilon(2\omega_o) - \sin^2\theta)^{1/2} .$$

which leaves

$$\Delta z \simeq -\frac{3L_n}{4}\beta^2$$

As the resonance region of the enhanced electric field extends in a realistic plasma to encompass both these planes, then it is possible to place an approximate value on the maximum red shift of the observed $2\omega_o$ spectrum, since the interacting electron plasma wave will have a down-shifted frequency from the incident laser, if it is assumed that $k_o \sim 0$.

For the $\ell + t \rightarrow t$ process the downshift in frequency is

$\Delta\omega = \frac{\omega_o}{2}\frac{\Delta n_e}{n_e}$ and as the corresponding shift in $\lambda_o/2$ is

$$\Delta\lambda_{2\omega} = \frac{\Delta\omega}{4\omega_o}\lambda_o$$

then

$$\Delta\lambda_{2\omega} = \frac{\lambda_o}{8}\frac{\Delta n_e}{n_e} = \frac{\lambda_o}{8} 3\beta^2 \times 2 \text{ waves}$$

$$\therefore \Delta\lambda_{2\omega} = \frac{3\lambda_o\beta^2}{4} \qquad 3.3.3.$$

and similarly for the $\ell + \ell \longrightarrow t$ process

$$-2(\varepsilon(\omega_o))^{1/2} = -2\beta(\varepsilon(2\omega_o) - \sin^2\theta)^{1/2}$$

from which is obtained

$$\Delta\lambda_{2\omega} = \frac{3}{16}\lambda_o\beta^2 \qquad - 3.3.4$$

As the former is the far more probable mechanism, as shown by both Vinogradov & Pustuvalov[2] and Erokhin et al[3], a typical anticipated time integrated red shift of the spectral peak may be estimated as a maximum of ~12 Å. This is if the thermal electron temperature is ~0.8 keV, as predicted from computer simulation and also measurements performed using the X-ray emission simultaneously attenuated by different thicknesses of beryllium foil[5].

3.4 <u>$2\omega_o$ generation due to parametric instability</u>

Above the threshold irradiance for parametric instability, second harmonic generation can result from the production of parametrically excited electron plasma waves, and their subsequent recombination; either with themselves or an incident photon which is incoming or scattered. the actual mechanism of interest here is the parametric decay instability where an incident photon 'decays' into a plasmon and an ion acoustic phonon.

viz $\omega_o \longrightarrow \omega_{pe} + \omega_{ia}$ $\qquad t \longrightarrow \ell + s$

& $\underline{k}_o \longrightarrow \underline{k}_{pe} + \underline{k}_{ia}$

Determination of the threshold for this instability in an homogeneous plasma has been given by many authors. Silin[6] used hydrodynamic equations for a cold plasma to obtain the growth rate for a transverse wave well above threshold, and this work was modified and extended by Nishikawa[7] to include damping. For an incident laser beam whose electric field gives rise to an electron 'quiver' velocity less than the electron thermal velocity, he shows that the threshold criterion and the growth rate, or time for the amplitude of the excited wave to increase by the exponential e, to be as below.

Threshold

$$\phi > \frac{4\, m_e \omega_o^2 c\, \varepsilon_o k_B\, T_e}{e^2} \frac{\nu_{ed}}{\omega_{pe}} \frac{\nu_{id}}{\omega_{ia}} \quad W.cm^{-2}$$

Growth rate

$$\gamma_{max} = \frac{1}{3} \left| \frac{m_e}{m_i} \right|^{1/3} \omega_{pe}$$

where ν_{ed} and ν_{id} are the electron and ion damping rates respectively, and m_i is the ionic mass and ε_o the permittivity of free space.

However in an inhomogeneous plasma, these conditions are complicated by the fact that the instability is confined to a finite spatial region over which matching conditions may be satisfied and energy loss due to convection occurs. Where the density scale length is less than the mean free path of the electrons, the result is to increase the threshold. The unstable region then acts as an amplifying medium, increasing the intensity of plasma waves passing through it, and is known as a

convective instability. This is in comparison to an absolute instability, where a mode with positive growth rate exists and whose amplitude decreases with distance away from the unstable region. A treatment of the parametric decay threshold in inhomogeneous plasma has been given by Perkins & Flick[8] using fluid equations with damping of the ion acoustic and electron plasma waves by both Landau and collisional means.

In their terms of the threshold being defined as the incident intensity required to raise the electron plasma wave amplitude by a factor of exp(5), they obtain the following:

$$\phi > 4.14 \cdot 10^{-13} \left(\frac{8}{k_e L_n} \left(1 + \frac{3T_e}{T_i} \right) \left(\frac{\nu_{id}}{\omega_{ia}} \right) + 3.2 \left(\frac{\nu_{id}}{\omega_{ia}} \frac{\nu_{ed}}{\omega_{pe}} \right) \right) n_e \, k_s \, T_e \quad W.cm^{-2}$$

-3.4.1

where k_e is the wave vector, the subscripts i and e denoting ionic and electronic parameters only.

To avoid strong Landau damping, the criterion

$k\lambda_D > \frac{1}{4}$ applies, where λ_D = the Debye shielding distance,

$$= \sqrt{\frac{\varepsilon_0 k_B T_e}{n_e e^2}},$$

and is satisfied for plasmas of interest in experiments here. From parameters determined from computer simulation, as in Chapter 7, equation 3.4.1 becomes,

$$\phi > 3.8 \cdot 10^{12} \ W.cm^{-2} \qquad (T_e = 0.8 \ keV)$$

for an Nd laser incident upon a spherical glass target. This irradiance was easily exceeded by the focussed laser in the majority of experiments, so that parametric generation was

expected to be the predominant generation mechanism for $2\omega_o$ emission. Also equation 3.4.1 refers to the necessary irradiance at the critical surface, whereas as shown previously, the electric field vector adopts an Airy function form up to the turning point[1], irrespective of whether the light is s or p-polarised. Hence an enhancement or difference between the vacuum electric field of the laser beam, and the maximum field at the turning point which is available. This difference, or 'swelling factor' can reduce the calculated threshold by as much as an order of magnitude, since

$$\phi_{vac} = \phi_{pl}\sqrt{\varepsilon(z)}$$

where $\varepsilon(z)$ is the local dielectric constant and at the turning point is equal to $\sin^2\theta$. This process is clearly far less effective for processes close to the quarter critical surface, where the E-field enhancement is much less.

3.5 Recombination of parametrically excited waves.

The recombination of a parametrically excited plasmon with an incident photon to form a $2\omega_o$ photon is far more probable than the recombination of two excited plasmons to form a similar photon, and hence the spectral shift of the generated $2\omega_o$ spectrum will be dependent on the peak shift of the plasmon spectrum from the fundamental frequency. This shift is equal to the ion acoustic frequency, since

$$\delta\omega = 2\omega_o - (\omega_o - \omega_{pe}) = 2\omega_o - (\omega_o - (\omega_o - \omega_{ia})) = \omega_{ia}$$

From the appropiate dispersion relations of the two recombining waves, and the wavenumber and frequency matching conditions, the dispersion relation of the generated $2\omega_o$ wave can be seen to be

$$(2\omega_o - \omega_{ia})^2 = \omega_{pe}^2 + (2\underline{k}_o - \underline{k}_{ia})^2 c^2 \qquad - 3.5.1$$

since $\underline{k}_{ia} = \underline{k}_o - \underline{k}_{pe} = 2\underline{k}_o - \underline{k}_{ia}$.

In the region close to the critical surface, $\omega_{ia} << \omega_o$ and $\omega_{pe} \simeq \omega_o$,

hence 3.5.1 may be approximated to

$$4\omega_o^2 \simeq \omega_o^2 + (2\underline{k}_o - \underline{k}_{ia})^2 c^2 .$$

Also the incident wave vector $\underline{k}_o \sim 0$, so

$$3\omega_o^2 = \underline{k}_{ia}^2 c^2 .$$

$$\underline{k}_{ia} = \frac{\sqrt{3}\omega_o}{c} \qquad - 3.5.2$$

The red shift is $\omega_{ia} = \underline{k}_{ia} c_s$

Therefore $$\delta\omega = \sqrt{3}\,\frac{\omega_o}{c}\, c_s \qquad - 3.5.3$$

An estimate of the second harmonic peak shift can be made from 3.5.3 for typical plasma parameters. As the ion acoustic sound velocity is given by [9]

$$c_s^2 = \frac{\omega_{pe}^2 v_i^2 + \omega_{pi}^2 v_{th}^2}{\omega_{pe}^2}$$

where ω_{pe} and ω_{pi} are the electron and ion plasma frequencies and v_{th} and v_i are the respective thermal velocities,

For $\frac{\omega_{pe}^2}{v_{th}^2} << \frac{\omega_{pi}^2}{v_i^2}$, $\quad c_s^2 \simeq \frac{\omega_{pi}^2 v_{th}^2}{\omega_{pe}^2}$

therefore near the critical surface ($\omega_{pe} \simeq \omega_o$), $c_s \simeq \frac{\omega_{pi} v_{th}}{\omega_o}$

For a plasma formed from a glass target ($\bar{Z} \simeq 9.6$), with a mean electron temperature of 0.8 keV,

$$\delta\omega = 4\frac{\delta\lambda}{\lambda_o}\omega_o = \sqrt{3}\frac{\omega_o}{c}\frac{\omega_{pi}v_{th}}{\omega_o} = \sqrt{3}\frac{\omega_{pi}v_{th}}{c} \qquad - 3.5.4$$

$$= 3.94 \ .10^{13} \text{ rads/sec.}$$

$$\delta\lambda = \frac{\delta\omega\,\lambda_o}{\omega_o} \simeq 18.9 \text{ Å} \quad \text{red shift.}$$

However, at high irradiances, the induced electron quiver velocity becomes comparable with the thermal velocity in expression 3.5.4 and also the turning point ($\varepsilon = \sin^2\theta$) will govern the local electron plasma frequency which may mean that the position of this plane is more instrumental in governing the $2\omega_o$ spectral shift than the ion acoustic frequency.

Silin[10] has taken both these factors into account and has shown that in the case where the detuning or difference in frequency between the incident laser and local plasma frequency, ($\Delta\omega(z) = \omega_o - \omega_{pe}(z)$) is larger than the long wave ion acoustic oscillation, then expression 3.5.4 is modified by another term, so that

$$\delta\omega = 3\omega_{pi}\left[\frac{v_{th}^2}{c^2} + \frac{1}{4}\frac{v_o^2}{c^2}\frac{\omega_o}{\Delta\omega(z)}\right] \qquad - 3.5.5$$

where v_o is the quiver velocity $= \frac{eE_o}{m\omega_o} = \frac{e}{m\omega_o}\sqrt{\frac{\phi}{\varepsilon_o c}}$

Since the field up to the turning point may be represented by an Airy function, the distance to the point where $\omega_{pe}(z) = \omega_o - \Delta\omega_{pe}(z)$ from the critical surface in a linear density profile may be the distance to the first maximum of this function and therefore is

$$\left(\frac{c^2 L_n}{\omega_o^2}\right)^{1/3}.$$

Combining this with the parameters for an incident neodymium laser beam gives a final expression for the second harmonic peak spectral shift as: (Krokhin)[11] –

$$\Delta\lambda_{2\omega} = \frac{\delta\omega\,\lambda_o}{4\omega_o} = \left(\frac{Z}{A}\right)^{1/2}\left(20\ T_e + 7.0\ .10^{-15}\phi\left(\frac{L_n}{\lambda_o}\right)^{2/3}\right)^{1/2} \qquad - 3.5.6$$

where ϕ is the incident irradiance in $W.cm^{-2}$

A(Z) are the ~~target~~ Mass number(mean charge)

and T_e the electron temperature in keV.

From an assumption that the second term is not insignificant in comparison with the first, an electron temperature estimation may be obtained from experimentally observed $2\omega_0$ spectra,as suggested by Krokhin et al.[11] However, at high irradiances, the $2\omega_0$ spectrum is no longer dependent upon the electron temperature, as the second term in 3.5.6 predominates.

3.6 Effect of Doppler shift

The mechanisms of $2\omega_0$ generation described are active in plasma whose position relative to the incident laser was assumed stationary. Due to the conservation of energy and momentum the material ablated by the laser from a solid target will increase in temperature due to absorbed energy, and expand outwards. The equations for motion and continuity are, for equal electron and ion temperatures; i.e. a single fluid in motion:

$$m_i n\left(\frac{d}{dt} + v\frac{d}{dz}\right) v = -2\, k_B T \frac{dn}{dz}$$

Z=1 isothermal condition

and

$$\frac{dn}{dt} + \frac{d(nv)}{dz} = 0 .$$

for one dimension (z) only, where z is the distance from the ablation surface, and v the expansion velocity. Solutions to these two equations are of the form:

$$n = n_o \exp -\left(\frac{z}{c_s t}\right)$$

$$v_{out} = c_s + \frac{z}{t}$$

where c_s is the ion sound speed of the order of $\left(\frac{2\, k_B T_i}{m_i}\right)^{1/2}$ (m/s). At the rate of outwards bulk motion of the plasma, the spectral shift due to the Doppler effect will be observable, and for measurements taken in the backward direction, will correspond to a blue shift rather than the red shift due to the mechanisms of interaction with frequencies less than the laser frequency. Using a typical plasma temperature of 0.8 keV, an anticipated spectral blue shift due to the Doppler effect is as below, for a nominal outward expansion velocity of 10^5 m/s.

$$\frac{\Delta\lambda}{\lambda} = \frac{2\, v_{out}}{c} = 0.06\% .$$

At $2\omega_0$, this corresponds to 3.5 Å at 5320 Å, which was not negligible with the resolution available on film recorded spectra.

3.7 Previous experimental work on the observation of emission near $2\omega_0$.

Probably the first observation of second harmonic emission from laser produced plasma was made by Caruso et al[12], using the mode-locked pulse from an Nd laser to give 10^{12} W.cm^{-2} on target. Spectral resolution was poor, and no detail was apparent; either within the spectrum or within the subsequent time resolution using a rotating mirror streak camera. With the advent of large laser installations for the study of thermonuclear plasmas, several observations of spectrally resolved $2\omega_0$ emission were recorded[13-20] and also values for the conversion efficiency of

incident into $2\omega_0$ light. Of these reports, all were observed using neodymium doped glass or YAG, or gaseous CO_2 as the lasing medium, since these represent the state of the art with regard to high power availability and efficiency respectively. The $2\omega_0$ spectra almost all had an asymmetric broadening to the red, and the peak red shifted also, whilst some showed a peak coincident with the true harmonic wavelength. Of note, Yamanaka et al[15] observed spectral sidebands which departed from the true harmonic by frequencies proportional to the target Z number, as seen for solid hydrogen and deuterium. The results of experiments to date to observe $2\omega_0$ spectra are presented in Fig. 3.7.1, and although not comprehensive, experimental details are recorded where they are known. Of these, Bychenkov et al[21] have also temporally resolved the $2\omega_0$ spectrum with a resolution of 100ps within an incident pulse length of 2ns. Again, no detail was apparent or gross shift to either direction. However, Decroisette et al[14] used an image converter to observe spectra at a particular point of 3ns after the start of the laser pulse, and found a preferential component coincident with the true $2\omega_0$ position, amid a broadened spectrum to the red.

Studies of laser irradiated targets to observe the spatial regions of $2\omega_0$ emission have also been reported. Since the $2\omega_0$ light emerges from a region in the vicinity of the critical surface, bulk motion of this surface may be seen by following the $2\omega_0$ light, particularly if time resolution is possible. The expanding critical surface(s) from a microballoon target used for spherical implosion studies are particularly useful in this

respect since sideways observation of a plane which is used for symmetrical irradiation can simultaneously monitor the critical surface expansion due to each beam, as performed by Jackel et al[22], and Leonard and Cover[23], for four beam and twin beam illumination respectively. Agreement between experiment and numerical simulation was found to be excellent in both cases. The very limited data on the polarisation of generated $2\omega_o$ light with respect to the incident light is confused and differs widely. Reports range from almost a 100% maintainance of polarisation of the incident beam upon conversion to $2\omega_o$[24], to almost complete depolarisation.[13] Of particular note, Eidmann and Sigel[24] have shown evidence for the generation of $2\omega_o$ light upon reflection when the incident beam is p-polarised and its square law dependence upon the incident intensity.

Fig. 3.7.1 $2\omega_o$ spectra observed in laser-produced plasma experiments.

EXPERIMENT & REF no.	INCIDENT LASER PULSE					target	$\frac{I_{2\omega}}{I_o}$	$2\omega_o$ SPECTRAL DETAILS		
	λ_o (μm)	$\Delta\lambda$ Å	E_j (J)	Δt	I_o W.cm^{-2}			$\Delta\lambda$ Å FWHM	$\delta\lambda$ Å	
CARUSO et al [12]	1.06		1-5	2 ×2 ps	~10^{15}	D_2	10^{-5} — 10^{-6}			little detail reported since v. low spectral resolution.
BOBIN et al [13]	1.06	30	15	15 ns	4. 10^{13}	H_2		30	0	asymm. red broadening
DECROISETTE et al [14]	1.06	0.5			4 10^{13}			30	0	similar expt to ref except for narrow band laser.
YAMANAKA et al [15]	1.06	1.–6 Å 2.–60	40	2 ns	< 2 . 10^{14}	H_2 D_2		30 - 60	~+2	isotopic dependence of spectral sidebands (red side)
P. LEE et al [16]	1.06	3	~ 5	25 ps	10^{16}	$(CH_2)_n$	5. 10^{-4} (b/s)	20	+3	conversion efficiencies given for sidescatter also.
BURNETT et al [17]	10.6	20	25	1.9 ns	7.5 10^{13}	Al	4 . 10^{-5}	80	+20	
GREK et al [18]	10.6		4 — 5	~ 1.7 ns	< 10^{13}	$(CH_2)_n$ Al.	4. 10^{-7}	23 ± 6	−64 ± 18	spectrum built-up in shot by shot.
McLEAN et al [19]	1.06		6 — 10	75 ps	~ 10^{16}	$(CH_2)_n$	4. 10^{-3}	29	~ +2	other integral harmonics up to n = 5 recorded.
GARBAN et al [20]	10.6		40	40 ns	< 10^{12}	$(CH_2)_n$	5 . 10^{-6}	23 ± 2	~ +2 ①	2 components — one ① ~ $2\omega_o$ other ~ 15 Å to red
BYCHENKOV et al. [21]	1.06	10	110	2 ns	10^{14}	μ-balloon		13	0	asym. red broadening

Chapter 3 - References.

1. V L Ginzburg, 'Propagation of e-m waves in plasmas, North Holland, 1970

2. A V Vinogradov & V V Pustuvalov, Sov. Phys. JETP, 36, 3 1973

3. N S Erokhin, S S Moiseev & V V Mukhin, Nucl. Fusion, 14 p333, 1974

4. N G Denisov, Zh. Eksp. Teor. Fiz. 31, p609, 1956

5. F Floux, D Cognard, A Saleres & D Redon, Phys. Letts, 45A, p483 1973

6. V P Silin, Sov. Phys. JETP, 20, 1510, 1965

7. K Nishikawa, J. Phys. Soc. Japan, 24, p926 & 1152, 1968

8. F W Perkins & J Flick, Phys. Fluids, 14, 9, 1971

9. T J M Boyd & J J Sanderson, 'Plasma Dynamics', Nelson 1969

10. V P Silin, 'Parametric action of high power radiation on a plasma' (In Russian) Nauka 1973

11. O N Krokhin, V V Pustuvalov, A A Rupasov, V P Silin, G V Sklizkov, A N Starodub, V P Tikhonchuk & A S Shikanov, JETP Letts, 22, 1, 1975

12. A Caruso, A DeAngelis, G Gatti, T Gratton & S Martelucci, Phys. Lett, 33A, 29, 1970

13. J L Bobin, M Decroisette, B Meyer & Y Vitel, Phys. Rev. Letts, 30, 13, 1973

14. M Decroisette, B Meyer & Y Vitel, Phys. Lett, 45A, 6, 1973

15. C Yamanaka, T Yamanaka, T Sasaki, J Mizui & H B Kang, Phys. Rev. Letts, 32, 19, 1974

16. Ping Lee, D V Giovanelli, R P Godwin & G H McCall, Appl. Phys. Letts, 24, 9, 1974

17. N H Burnett, H A Baldis, M C Richardson & G D Enright, Appl. Phys. Letts, 31, 3, 1977

18. B Grek, H Pepin, T W Johnston, J N LeBoeuf & H A Baldis, Nucl. Fusion, 17, 6, 1977

19. E A McLean, J A Stamper, B H Ripin, H R Griem, J M McMahon & S E Bodner, Appl. Phys. Letts, 31, 12, 1977

20. C Garban, E Fabre, C Stenz, C Popovics, J Virmont & F Amiranoff, J. de Physique, Letts, 39, 11, 1978

21. V Yu Bychenkov, Yu A Zakharenkov, O N Krokhin, A A Rupasov V H V P Silin, G V Sklizkov, A N Starodub, V T Tikhonchuk & A S Shikanov, JETP Lett, 26, 6, 1977

22. S Jackel, B Perry & M Lubin, Phys. Rev. Letts, 37, 2, 1976

23. T Leonard & R Cover, KMS Fusion Inc. Annual Report 1977, Section 2.5

24. K Eidmann & R Sigel, Phys. Rev. Letts, 34, 13, 1975

-Chapter 4-

Experimental investigation into the nature of $2\omega_0$ emission.

4.1 Introduction.

Having shown the relevance of second harmonic emission in the general scheme of laser-plasma interaction, an experimental programme to observe and record the nature of such emission was now performed. To obtain the high laser intensities needed to drive parametric instabilities, the experiments were performed at the Central Laser Facility of the Science Research Council, which is described in Appendix B. Hence the laser wavelength, being that of neodymium doped glass, was 1.06μm, and energy pulses up to 35J were available, in a 100ps FWHM Gaussian profile.

General experimental method.

As far as possible all measurements of scattered radiation were recorded in the backwards direction, thereby leaving a large solid angle around the target for other diagnostics. This restriction also increased the reproducibility of results and permitted the development of diagnostic techniques from harmonic generation. Thus the same f/1 lens was used for focussing the incident laser light onto the target and also the collection of backscattered harmonic light. This meant that if the target was in focus for the incident laser light, then backscattered harmonic light was convergent. Also, the ablated plasma travelled towards the laser, resulting in a Doppler shift of the backscattered light, which needed to be deducted from any spectral displacement in the spectrum. The general experimental

layout in Fig. 4.1.1 shows a 'dog leg' in each beam, consisting of two dichroic mirrors, a_1, a_2, each having a reflectance greater than 98% @ 1.064μm and a transmission greater than 90% for visible wavelengths. Thus backscattered emission could be analysed after transmission back through the final turning mirror, a_1, and in the majority of experiments, the equipment was arranged on the East beam side. The initial experimental arrangement used to obtain spectra of backscattered harmonics is shown in Fig.4.1.1 Two half-metre f/4 Czerny-Turner spectrographs, A and B, were used to record the harmonic emission from the target: either the second and three-halves harmonics simultaneously, if mirror M_1 was a suitable dichroic, or alternatively, they both observed the same harmonic, if M_1 was a beamsplitter.

The backscattered radiation was relayed to the spectrographs by means of lenses L_1 and L_2. Consequently the resolution of the system was controlled by the lens f/number, which restricted the illuminated area of the grating. The spectrograph 'B' grating had 1200 lines per mm.(l.p.mm) and this permitted a maximum dispersion of 8Å/mm for second harmonic light in the first order. The spectrograph 'A' , otherwise a similar instrument to 'B', had a 600 l.p.mm. grating. Spectrograph 'C' was also a grating instrument of Czerny-Turner design and was used to monitor the incident laser pulse, which had a FWHM width close to the transform limit of 0.4Å. The pulse duration was nominally 100ps Gaussian (FWHM) in all experiments, and a photodiode detected

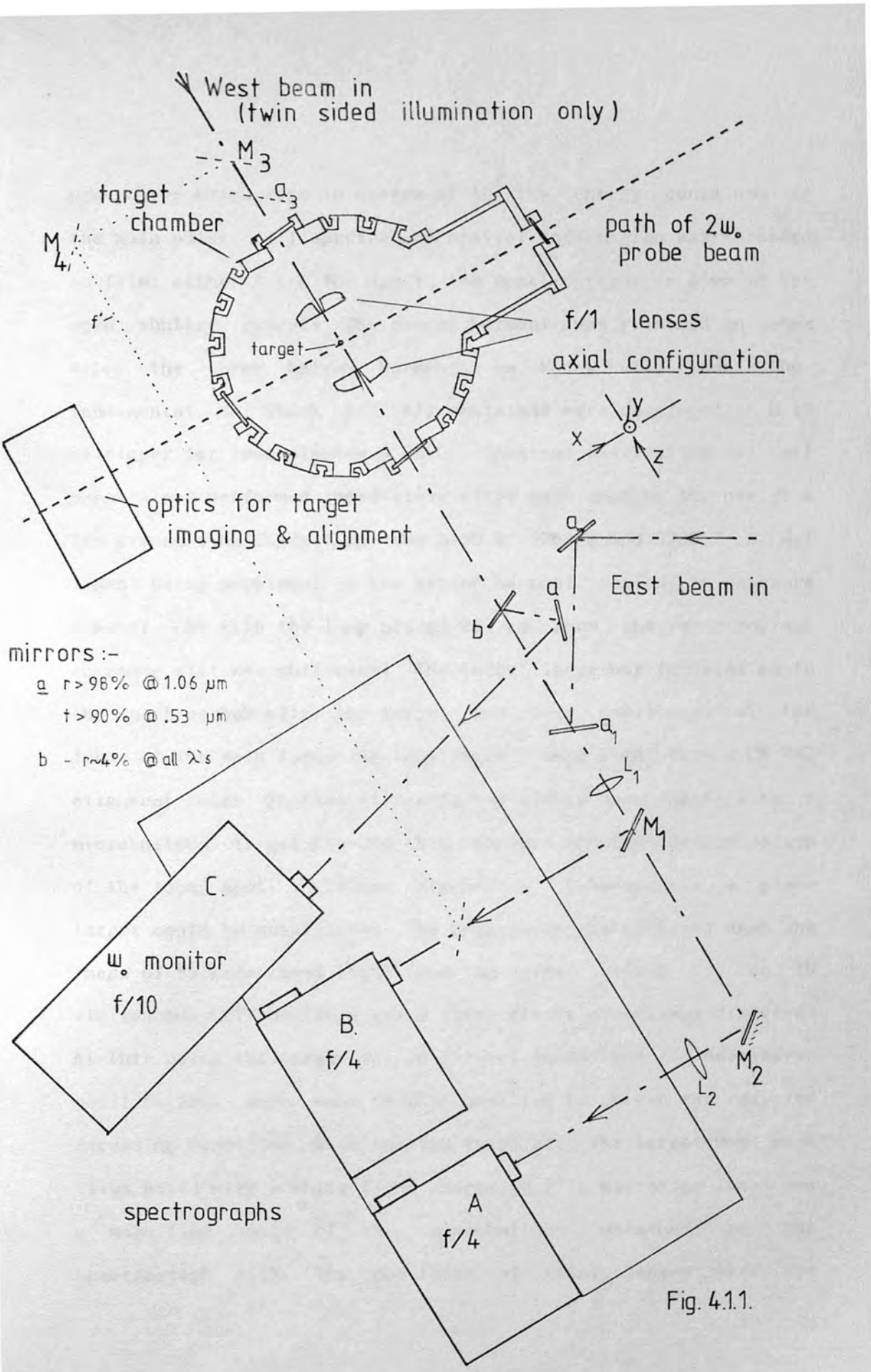

Fig. 4.1.1.

initial experimental arrangement

pre-pulses which were in excess of 10^{-5} the energy contained in the main pulse. All spectra and spatial information was recorded on film; either 4" x 5" for use in the spectrographs or 35mm in the open shutter cameras. The second harmonic was recorded on Kodak 4164, the three halves harmonic on Kodak 4143, and the fundamental on Kodak 1-Z. All emulsions were developed in D-19 developer for four minutes @ 20°C. Spectral calibration of all spectra was performed immediately after each shot by the use of a low pressure Hg/Cd/Zn lamp, the 5460.9, 5769.6 and 5789.7 Å HgI lines being prominent in the second harmonic region. An exposure time of ~5s with the lamp placed 20 cm from the spectrograph entrance slit was sufficient. The target image was focussed on to the spectrograph after the target had been positioned at the focus of the main focussing lens, with 1.06μm light from a CW YAG alignment laser. Initial alignment was always coincident with a microballoon target because this provided accurate determination of the focal spot in three dimensions. Subsequently a plane target could be substituted. The best focus was obtained when the image of backscattered light from the target viewed via an IR vidicon and CCTV monitors was a clear circle of minimum diameter. At this point the target was in correct focus, and if necessary, modifications were made to this position to obtain any required focussing condition. With the YAG laser off, the target was back illuminated with a white light source (e.g. a microsope lamp) and a magnified image of the microballoon obtained on the spectrograph slit. The positions of relay lenses were now

adjusted to give a good focus and alignment on the slit. The image of the wall of the back illuminated microballoon in the film plane of the spectrograph corresponded to a 'black line' across a spectral continuum, as observed on a tracing paper diffusing screen. This line was made sharp and then a narrow band filter was placed across the slit to enable just the portion of the spectrum relevant to the harmonic to be studied. The spectrograph was then found to be well aligned. With care, refocussing was found unnecessary for each shot on planar targets, but was preferable for spherical ones. Time resolution of the spectrum was a major feature of this work, and the only practical instrument to achieve a temporal resolution of 10ps was an electro-optic streak camera. This consists of a vacuum 'streak tube' and an image intensifier coupled to either film or electronic recording. The two instruments used in experiments are described in Section 4.5, both having photocathodes with S-20 sensitivities.

4.2 Time-integrated spectral $2\omega_o$ studies.

Spectra of the second harmonic light were obtained after irradiating a variety of planar and spherical targets were obtained with laser pulses of up to 15J energy. They were taken on spectrograph B (Fig.4.1.1.) when mirror M_1 was a 100% reflector. A spectrum obtained from a Chromium target at an irradiance of $\sim 10^{15}$ W.cm^{-2} is shown in Fig.4.2.1. The spectrum of bandwidth of 30A (FWHM), is asymmetrically broadened to the red

typical $2\omega_0$ spectrum

Fig. 4.2.1.

~ 80 μm

5461 .Å Hg I line

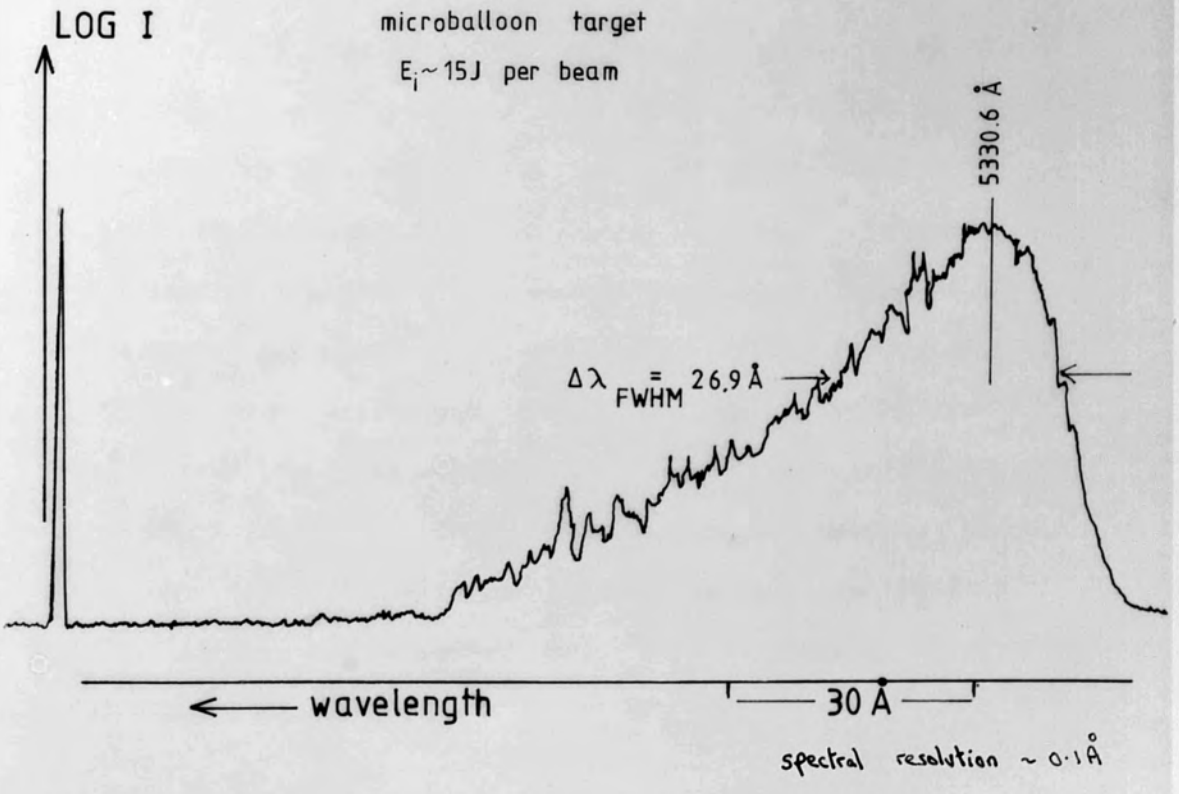

with a peak red-shifted by 20Å. Regular modulation of the red wing is also apparent, with a periodicity ~3Å. The energy conversion efficiency of the $2\omega_o$ emission from the incident energy was estimated to be 2.10^{-5} after correcting for the characteristics. of the film.

Although Fig.4.2.1 displays a typical $2\omega_o$ spectrum, in several cases characteristic differences were noted. In particular, this minority of spectra showed the form of Fig.4.2.2 where the asymmetric broadening to the red was replaced by a sideband which was far less intense than the main peak. The main peak was narrower and nearly symmetrical, but its peak was red shifted by up to 9Å. The spectra displaying this pattern were solely obtained from planar targets, of elements with a high Z number, or alternatively from thin foils up to 1.0μm thick. With these, the plasma formed from the foil became underdense during the laser pulse, so that some of the incident laser energy passed through the plasma without being absorbed, reflected or re-radiated. The plasma became underdense during the laser pulse, before being underdense to harmonic light. In the period when the maximum electron density was greater than n_{cr}, but less than $4 \times n_{cr}$, then $2\omega_o$ emission could be observed, both in the forward and backward directions. This is in contrast to massive targets where any forward scattered light would be reflected from its critical surface and observed only in the backscattered, or sidescattered directions.

atypical $2\omega_0$ spectrum

Fig. 4.2.2

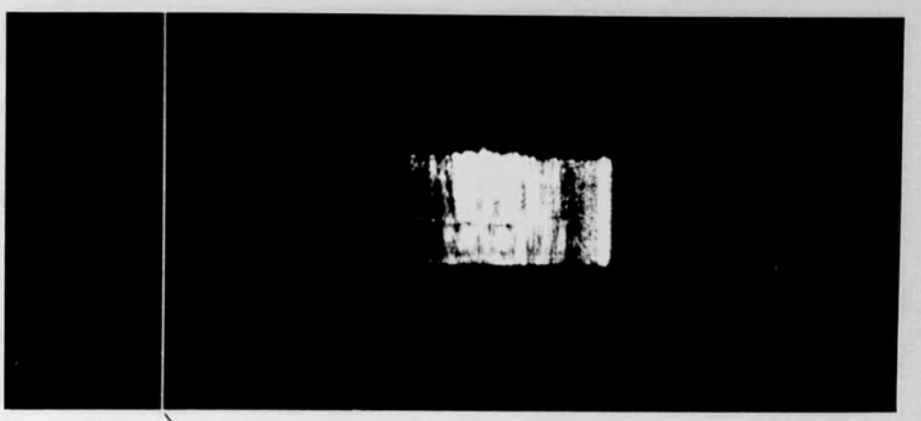

5461 Å HgI line

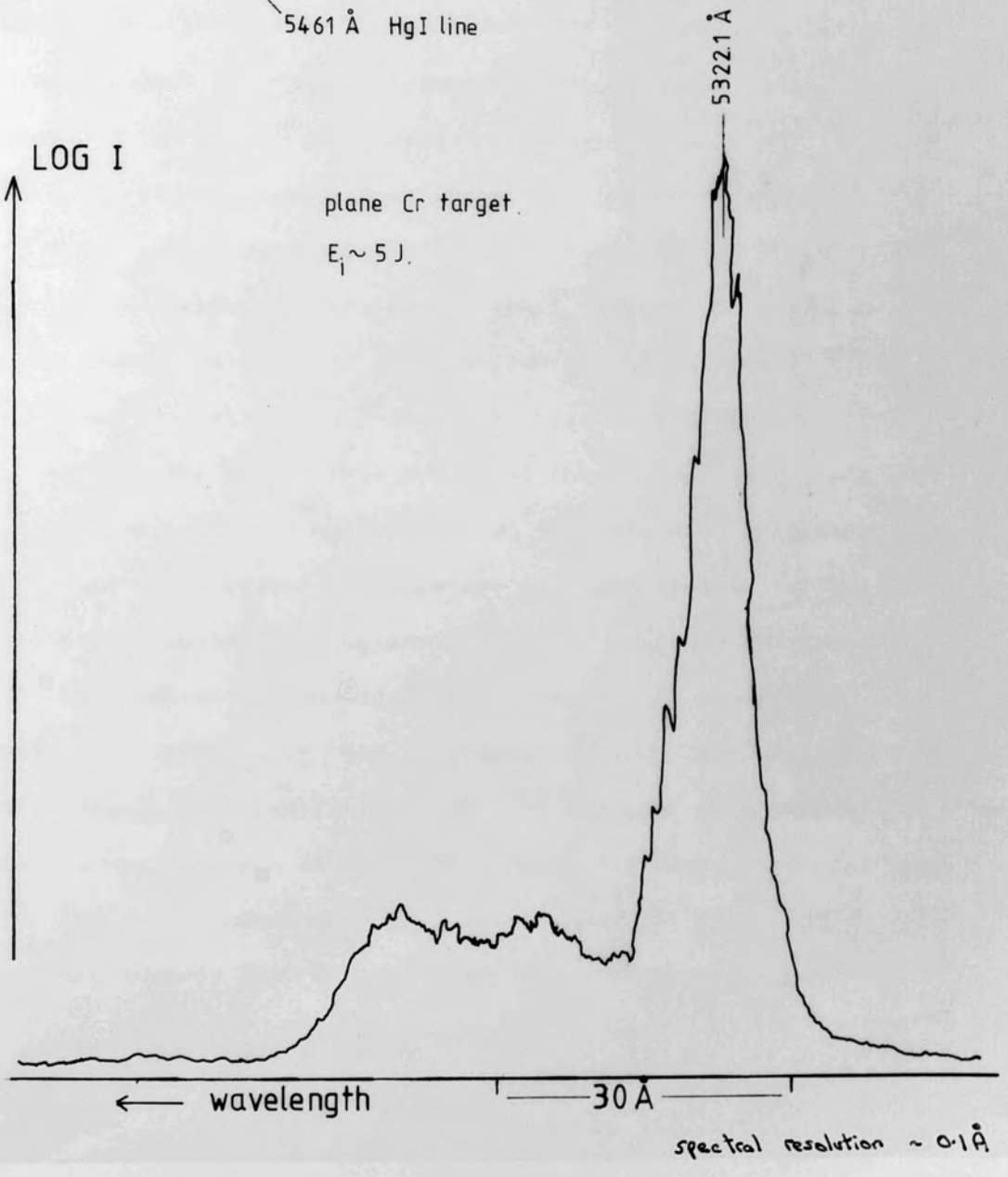

4.3 Angular and polarisation properties of $2\omega_o$ spectra.

To observe spectral differences of $2\omega_o$ emission in different directions, the forward and backward directions of a thin foil target were simultaneously imaged on a spectrograph, (B), one above another. The forward light path is indicated in Fig.4.1.1 by the dotted line (f') as only East beam illumination was used. To avoid damage to the mirrors M_3 and M_4 another dichroic mirror (a_3) was positioned outside the target chamber in the forward scattered path to reflect the transmitted ('burnthrough') energy of the incident laser, but transmit the harmonic light. This protected the optics from damage. An example of a result showing the $2\omega_o$ spectra obtained from forward and backward emission from a 0.08μm polystyrene foil is shown in Fig.4.3.1, with the backscattered spectrum uppermost. Apart from a difference in target magnification, the spectra show almost identical features of a broad peak with a sideband of decreasing intensity towards to the red. The hole in the middle of the backscattered spectrum is where 'burnthrough' has occured on the foil and the plasma is underdense. An unexpected feature of these spectra is that the peak of the transmitted $2\omega_o$ spectrum is blue shifted in comparison with the peak of the backscattered spectrum. As the spectra have similar structure, it was assumed that the $2\omega_o$ spectral distribution was independent of the angle of observation, and emission was observed in both the forward and backward directions from the same localised plasma region. If this region was expanding towards the incident beam, then the result would be a

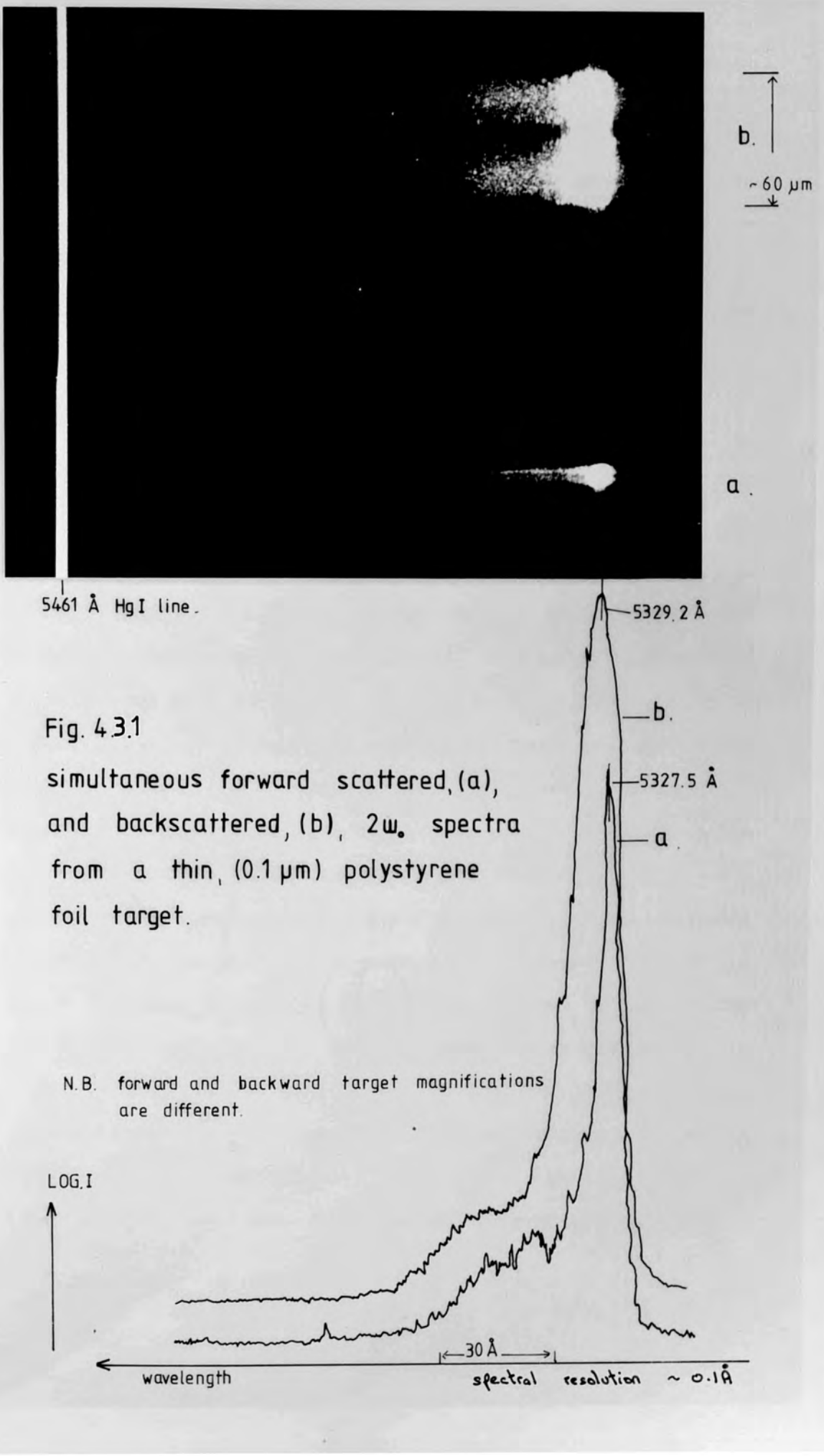

Fig. 4.3.1

simultaneous forward scattered, (a), and backscattered, (b), $2\omega_0$ spectra from a thin, (0.1 μm) polystyrene foil target.

$2\omega_o$ transmitted spectrum red-shifted in comparison with the backscattered spectrum; in contrast with the observed result. This anomaly will be discussed later in context with other experimental data. In association with this observation of two different emission directions, two further experiments were performed to look for preferential planes of $2\omega_o$ emission. In the first instance it was shown in Chapter 3 that $2\omega_o$ generation by linear transformation was achieved with p-polarised light incident upon a density gradient, such that only backscattered $2\omega_o$ should be observable along a similar path to that of the reflected incident beam. This would enable a preferential plane of $2\omega_o$ emission to be that of the incident beam and the ~~first~~ first experiment simply imaged the main focussing lens in $2\omega_o$ light emitted from the target, and was achieved by replacing M_1 in Fig.4.1.1 with a suitable lens and then an open shutter camera, with suitable filters. A photograph of this near-field intensity distribution appears in Fig.4.3.2 and shows no preferential plane of emission, although the incident beam was horizontally polarised. The target here was plane polythene and the incident energy ~1.5 Joules. As the emission did not appear predominant in any one plane or angle of observation, it was possible that spectral differences may be apparent depending on whether the $2\omega_o$ light was emitted in the plane of the incident light, or perpendicular to it. To experimentally determine any difference between these two planes, two spectrographs recorded backscattered light, but with polarisations perpendicular to each

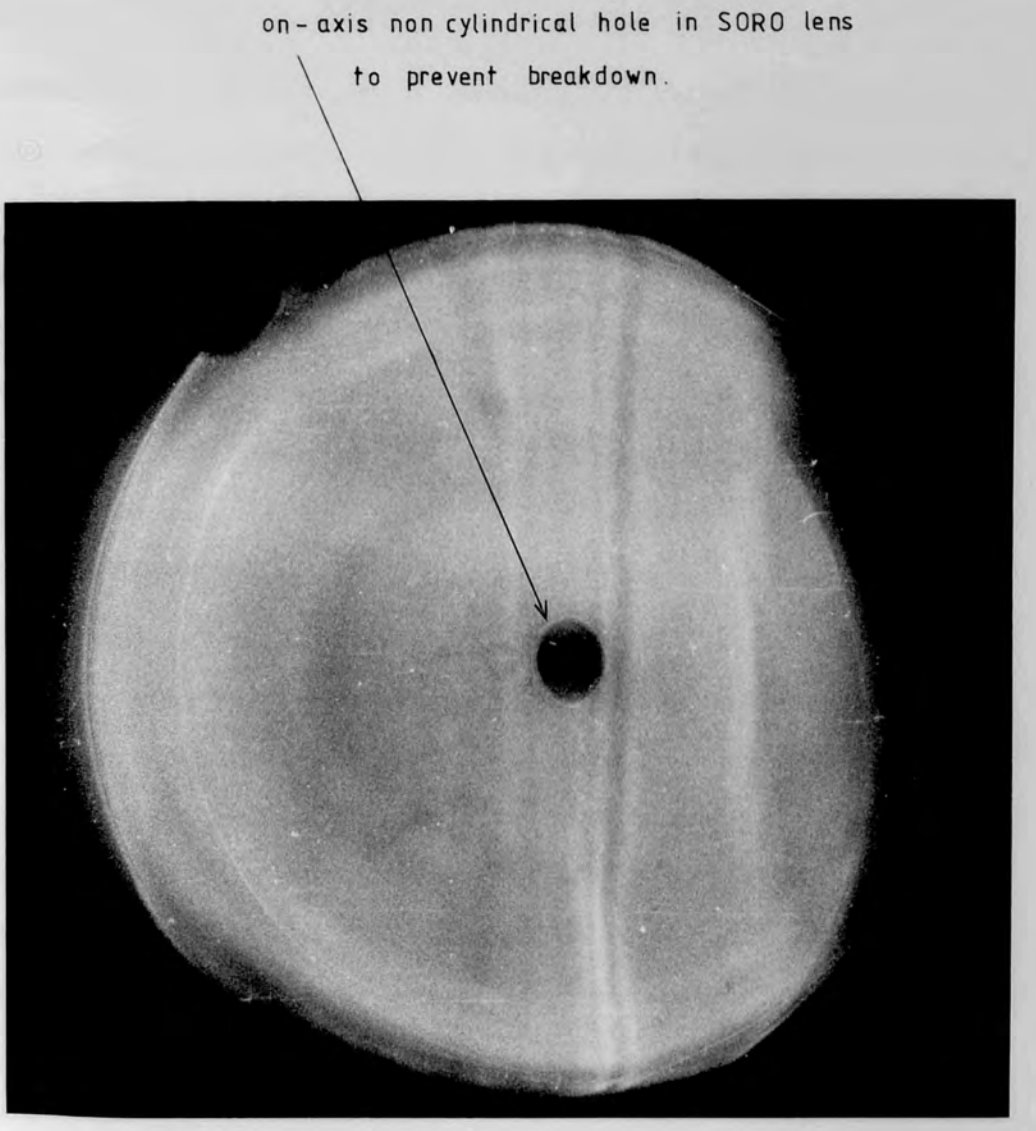

near-field picture of backscattered $2\omega_0$ light - plane of main focussing lens imaged after final turning mirror.

plane polythene target

Fig. 4.3.2

other. Mirror M_1 was a 50:50 beamsplitter set at an angle close to the optimum for reflecting s-polarised emission and transmitting p-polarised . Further polarisation analysers of Polaroid filters were placed in front of each spectrograph. So unless the $2\omega_o$ spectrum was the same in both polarisations some difference in the two was to be expected. However, the resultant spectra from a plane CH_2 target showed no evidence for any spectral differences, and although both spectral peaks were red-shifted, both corresponded to similar values to within 0.8Å. A typical pair of spectra from a CH_2 plane target appear in Fig.4.3.3, taken with an incident energy ~1.0 Joule. A total $2\omega_o$ energy dependence upon incident energy was also found. This was determined by the use of a p-i-n photodiode placed in the backscattered path to receive focussed harmonic light, with narrow band $2\omega_o$ filters. The results for $2\omega_o$ light from a plane target are displayed in Fig.4.3.4. and represent a good fit to a square law over the region for which the photodiode was found to be linear.

4.4 Spatially resolved $2\omega_o$ emission.

Having spectrally resolved $2\omega_o$ light under several different circumstances, it was of importance to observe the region(s) of the irradiated plasma which were responsible for this emission, and to observe their spatial extent, and hence motion. Since, as shown previously, the hydrodynamic plasma expansion towards the incident beam was estimated to be of such a velocity that the Doppler effect on backscattered spectra was not negligible, being $\sim 10^5$ m/s. Experimental determination of these regions involved

Fig. 4.3.3

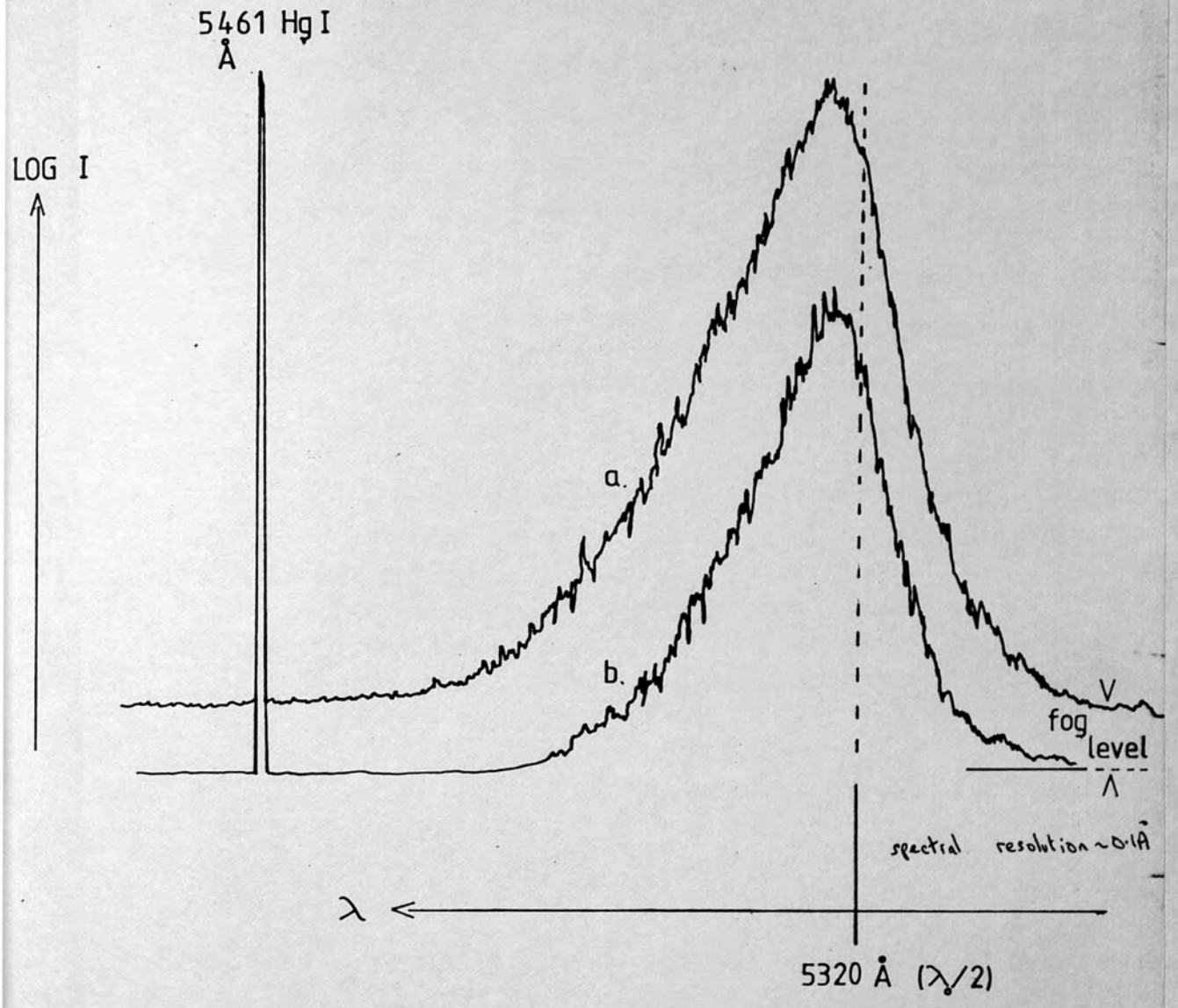

simultaneous backscattered $2\omega_0$ spectra to observe any spectral dependence upon polarisation.

a - $2\omega_0$ component in same plane as polarised incident laser.

b - " " $\perp$ to " of " " "

polythene target. $E_i \sim 1.5$ J

tracing the motion of the critical surface by means of the $2\omega_o$ light emitted therefrom. As shown before, the region of $2\omega_o$ generation is within 10% of the density at the critical surface rather than on it, but the distances between these regions and the critical surface itself are certainly small enough to be less than the resolution limit of any optical system used. For ease of imaging and for comparison of two expanding surfaces, microballoon targets were used and imaged perpendicular to the E-W axis of irradiation, using short focal length microscope objective lenses.

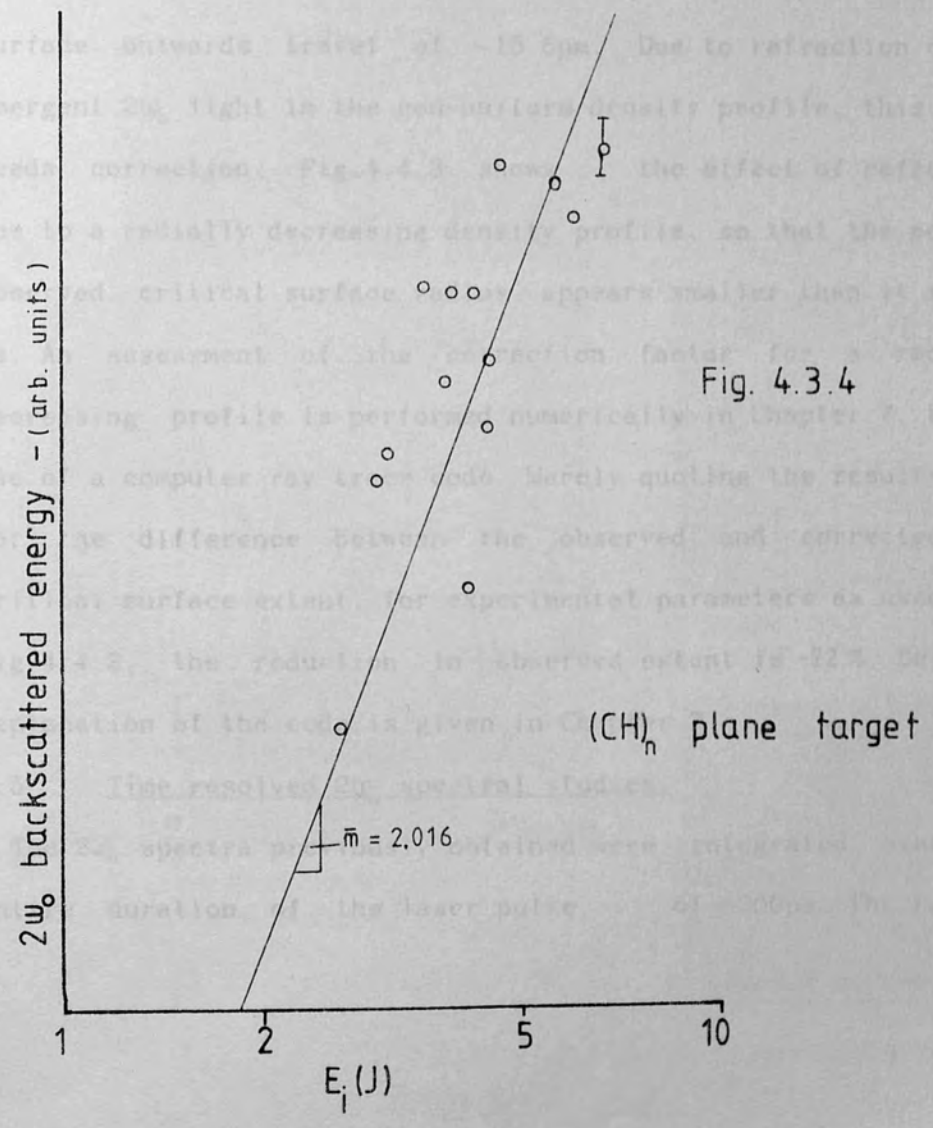

Fig. 4.3.4

These were placed in close proximity proximity to the target and provided an image in the film plane of an open shutter camera placed outside the target chamber, as shown in Fig.4.4.1. Other directions of observation were also used to provide a degree of three dimensional information, when simultaneous photographs were taken off the same shot. Typical time-integrated photographs of a microballoon target imaged in its own $2\omega_o$ light are shown in Fig.4.4.2; double sided illumination of ~8 Joules per beam being used. The central circle indicates the scale size of the microballoon before irradiation, such that the two lobes of emission from each side are distinct, and show a peak critical surface outwards travel of ~15.5μm. Due to refraction of the emergent $2\omega_o$ light in the non-uniform density profile, this value needs correction. Fig.4.4.3 shows the effect of refraction due to a radially decreasing density profile, so that the maximum observed critical surface radius appears smaller than it really is. An assessment of the correction factor for a radially decreasing profile is performed numerically in Chapter 7, by the use of a computer ray trace code. Merely quoting the result here for the difference between the observed and corrected peak critical surface extent, for experimental parameters as used for Fig.4.4.2, the reduction in observed extent is ~22%. Detailed explanation of the code is given in Chapter 7.

4.5 Time resolved $2\omega_o$ spectral studies.

The $2\omega_o$ spectra previously obtained were integrated over the entire duration of the laser pulse, of ~200ps. The rate of

spatially resolved $2\omega_0$ emission.

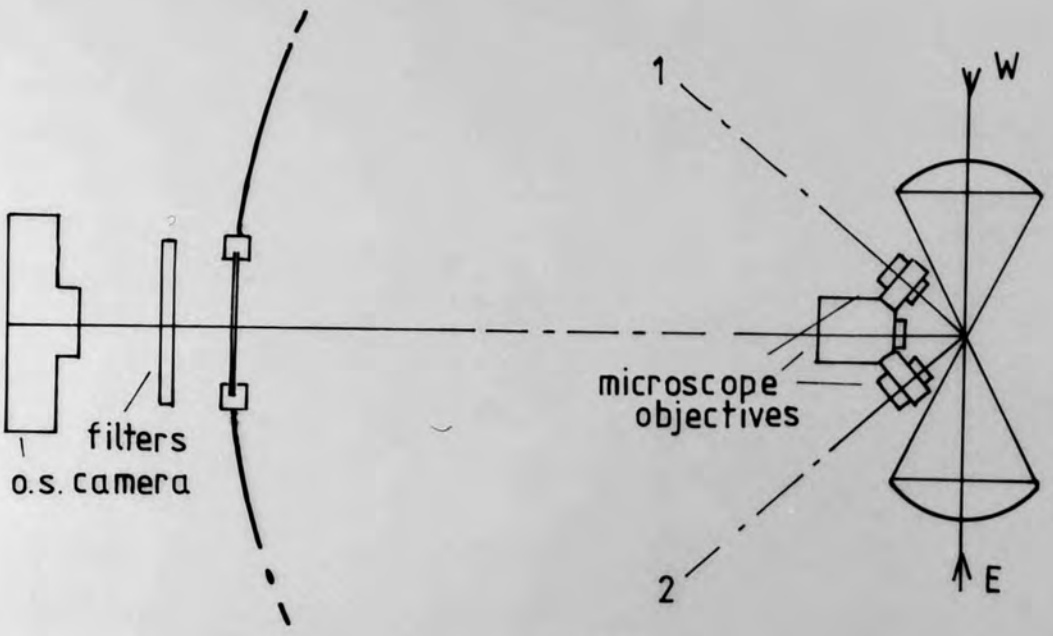

Fig. 4.4.1

SHOT A - $E_i \sim 8.5$ J per beam

SHOT B - E_i as A

side-on $2\omega_0$ light. hor. polarised.

$2\omega_0$ - hor. pol.

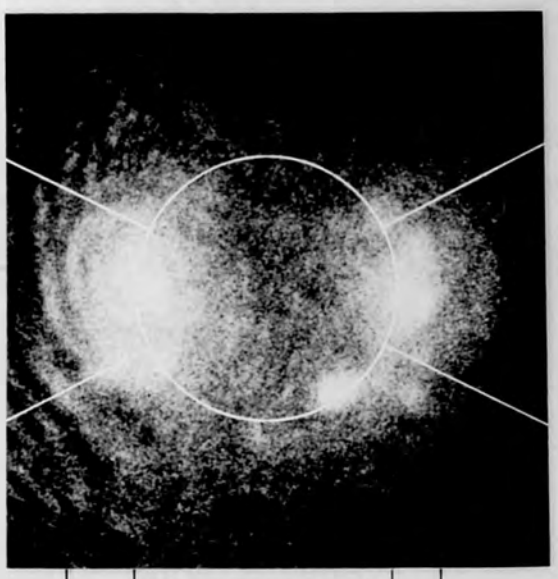

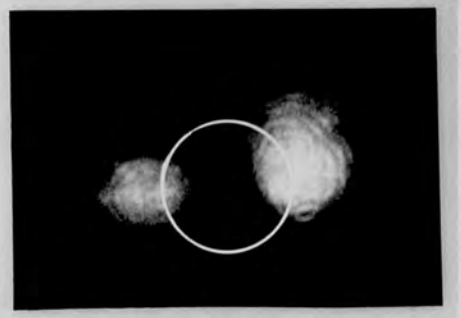

direction 1 - 45° to z-axis
x-z plane

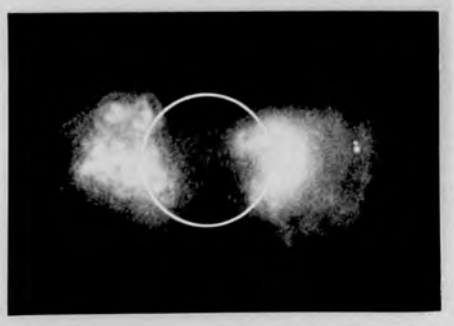

direction 2 - as above.

Fig. 4.4.2

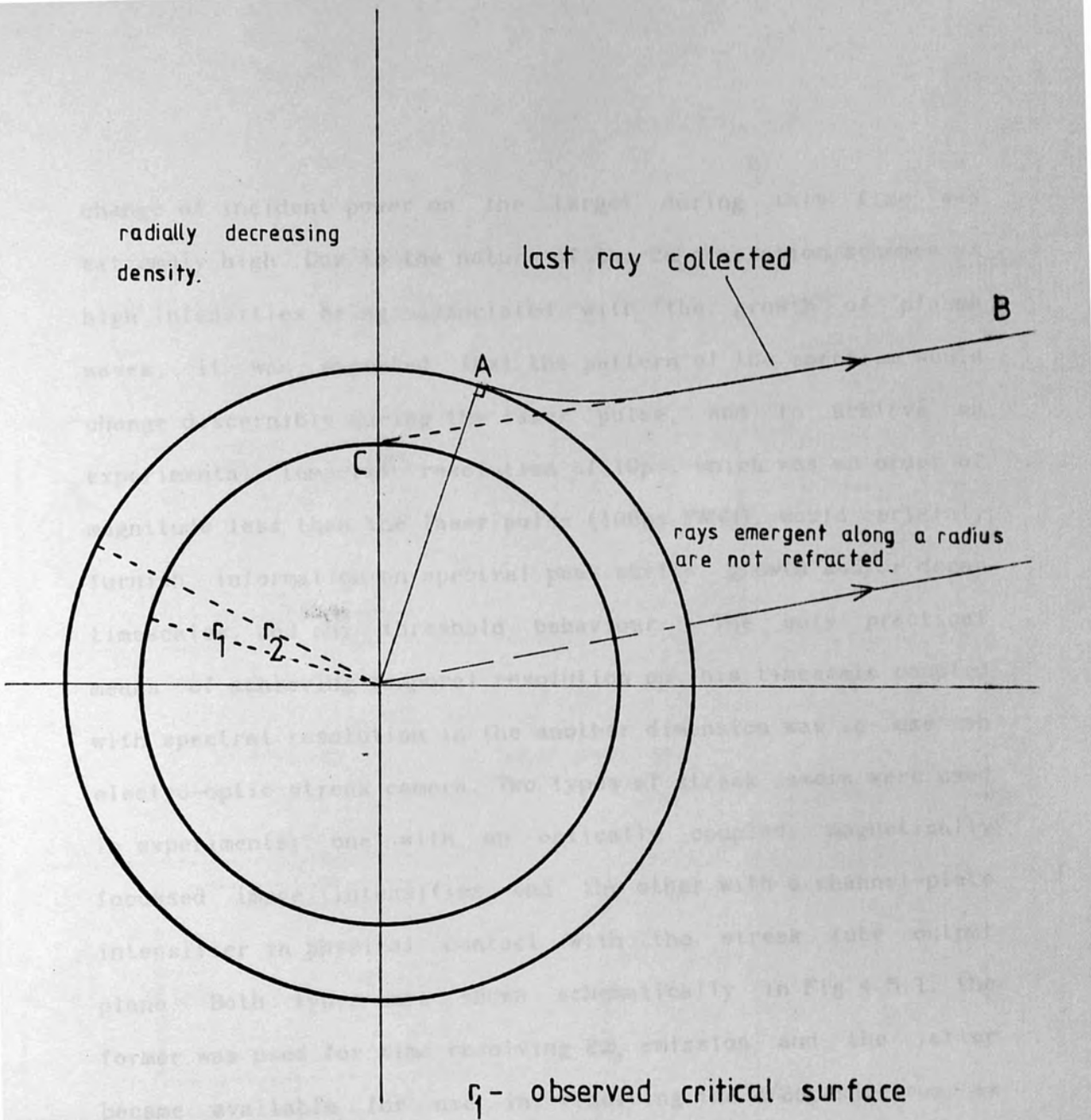

r_1 - observed critical surface

r_2 - actual " "

schematic representation of refraction of $2\omega_o$ light emitted from the critical surface.

Fig. 4.4.3.

change of incident power on the target during this time was extremely high. Due to the nature of the $2\omega_o$ generation schemes at high intensities being associated with the growth of plasma waves, it was expected that the pattern of the spectrum would change discernibly during the laser pulse, and to achieve an experimental temporal resolution of 10ps, which was an order of magnitude less than the laser pulse (100ps FWHM), would certainly furnish information on spectral peak shifts, growth and/or decay timescales, and any threshold behaviour. The only practical means of achieving temporal resolution on this timescale coupled with spectral resolution in the another dimension was to use an electro-optic streak camera. Two types of streak camera were used in experiments; one with an optically coupled, magnetically focussed image intensifier and the other with a channel-plate intensifier in physical contact with the streak tube output plane. Both types are shown schematically in Fig.4.5.1; the former was used for time resolving $2\omega_o$ emission and the latter became available for use in resolving the $3/2\omega_o$ spectrum, as explained in Chapter 6. Each of these instruments was capable of time resolution down to ~5ps, but when used to time resolve spectra, using a grating spectrograph, this figure was degraded due to optical path differences in the spectrograph. Whilst the spectral resolution obtainable with the grating is directly proportional to the number of illuminated lines of the grating, (assuming it is not slit width limited), the potential temporal resolution of the resultant spectrum is inversely proportional to

Fig. 4.5.1.

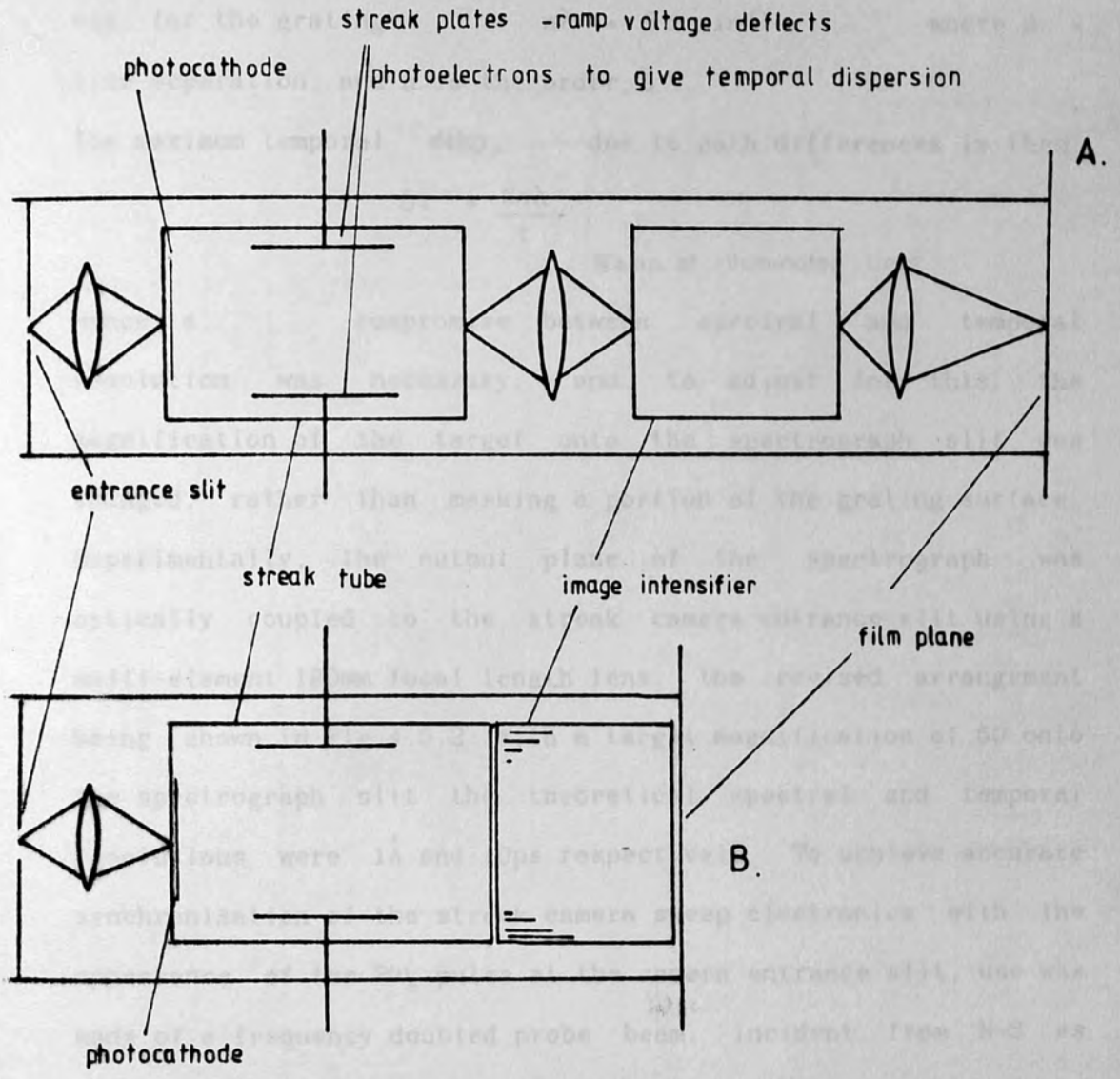

schematics of the two electro-optic streak cameras used in time resolved experiments.

A. E.P.L. camera - optically coupled magnetically focussed intensifier

B Imacon 675 - physically contacted channel plate intensifier

this number.

viz. for the grating: $n\lambda = 2d \sin\Theta$ where d = line separation, and n is the order, & ∴

The maximum temporal delay, due to path differences is then:

$$\delta t = \frac{Nn\lambda}{c},$$

N = no. of illuminated lines

Hence a compromise between spectral and temporal resolution was necessary, and to adjust for this, the magnification of the target onto the spectrograph slit was changed, rather than masking a portion of the grating surface. Experimentally, the output plane of the spectrograph was optically coupled to the streak camera entrance slit using a multi-element 120mm focal length lens, the revised arrangement being shown in Fig.4.5.2. With a target magnification of 50 onto the spectrograph slit the theoretical spectral and temporal resolutions were 1Å and 10ps respectively. To achieve accurate synchronisation of the streak camera sweep electronics with the appearance of the $2\omega_o$ pulse at the camera entrance slit, use was made of a frequency doubled probe beam, incident from N-S as shown in Fig.4.1.1. This beam, generated from a portion of the incident laser light by passage through an ADP crystal was arranged to arrive at the target within 10ps of the main pulse, and was then reflected by a 45° mirror in the target position along the East beam path to simulate a backscattered $2\omega_o$ pulse. This pulse gave an accurate time marker to allow time delays between the photodiode trigger pulse and the sweep commence to be

Fig. 4.5 2.

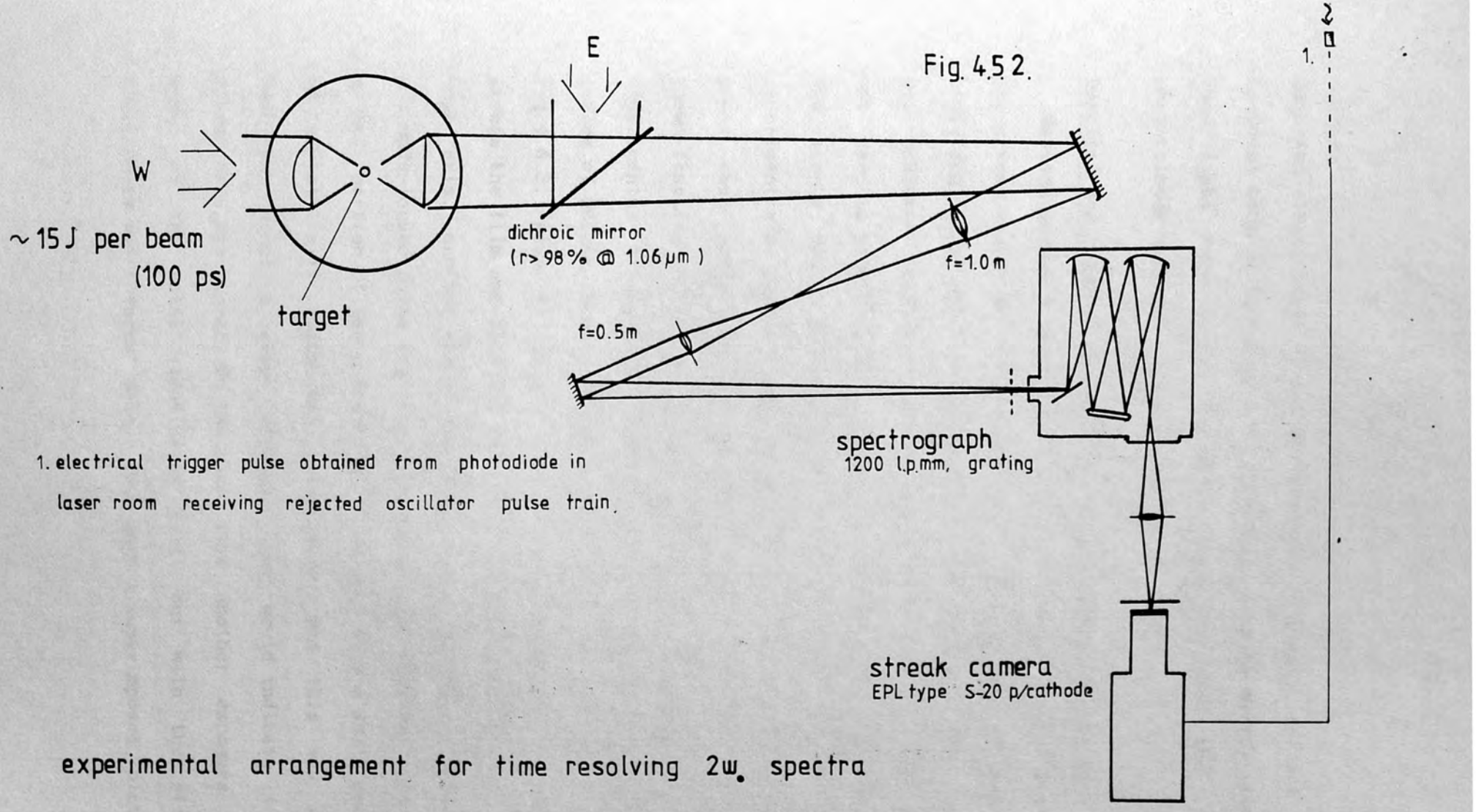

1. electrical trigger pulse obtained from photodiode in laser room receiving rejected oscillator pulse train.

experimental arrangement for time resolving $2\omega_0$ spectra

adjusted effectively. It was not possible to simply reflect the incident beam at low power since the final turning mirror removed this light back along the laser path and also the S-20 photocathode sensitivity was of no use at 1.06μm

Spectral and temporal calibration for time resolved studies.

Besides adequate synchronisation, some means of calibrating the streak camera was necessary, and also a means for calibrating individual shots for both wavelength and dispersion. The former was achieved in a separate experiment where an EPL 33 dye laser was used to provide a mode-locked train which was observed by the streak camera after passage through an air-gap etalon. This experiment also gave the dynamic range of the camera and film, since each pulse of the mode-locked train was attenuated by a known fraction and a definite round trip time existed. The experimental arrangement together with a typical time resolved series of pulses from a single mode-locked pulse appears in Fig.4.5.3. Also to ensure that the camera had a linear sweep across the film and that the entrance slit was perpendicular to this axis, another simple experiment was performed. For this, a non mode-locked pulse from the dye laser was incident upon a masked portion of the entrance slit, so that only a small amount of the total slit width was illuminated, and this was time resolved. Hence a swept straight line would indicate if the streak axis was linear. On the same film another exposure was made of the total illuminated slit, but with the streak electronics off ('focus' mode). This gave a superimposed picture

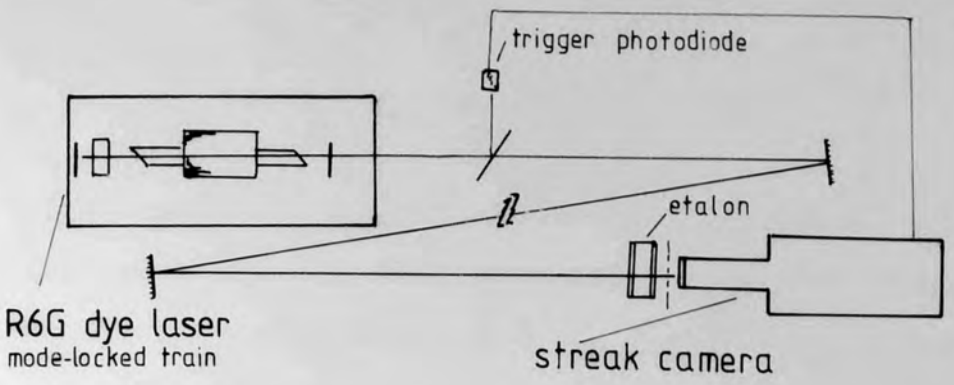

Fig. 4.5.3

a. temporal calibration.

exp. arrangement as above.

pulses separated by 15 ps

results shown for Imacon 675 streak camera.

time ⟶

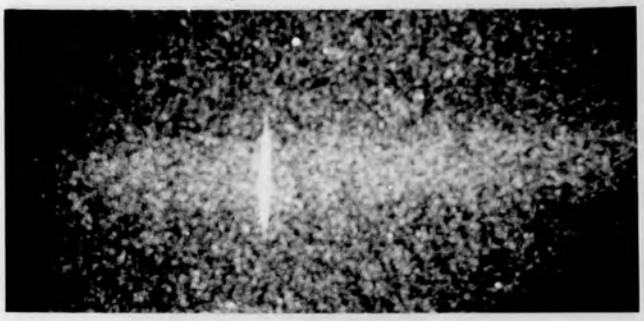

b. camera entrance slit viewed in 'focus' & 'streaked modes.

laser not mode-locked, no etalon.

streak camera calibration — Fig. 4.5.4.

of the entrance slit which clearly should be perpendicular to the time axis. This was found to be so, a result also being shown in Fig.4.5.4 Shot to shot spectral calibration was performed using a Hg/Cd/Zn lamp, as before, just after each shot. With the camera in focus mode, an exposure was made with the spectrograph wavelength setting on 5461 Å. Hence the 5461 Å HgI line provided a 'dot' on the film correspondng to the optical axis, since for each shot the spectrograph setting was 5320Å. With another exposure with the setting on 5441Å, this corresponded to 5320 + (5461 - 5441) = 5340Å, again using the 5461 Å HgI line. Another exposure with the setting on 5471 gave a corresponding wavelength of 5320 + (5461 - 5471) = 5310Å. Hence three dots on the film provided detail on the dispersion (distance between the two extreme dots was 30Å), and the wavelength, since the centre dot corresponded to the true second harmonic position.

Results.

Several shots were recorded of the time resolved second harmonic spectrum at $\sim 10^{16}$ W.cm^{-2}, with calibration after each shot. The results were taken on Kodak 2485 70mm film of 10,000 ASA rating, developed in D-19 for 5 minutes at 30°C. Three spectra from similar shots onto microballoon targets are shown in Fig.4.5.5, and display several interesting and unusual features. Firstly, the emission is pulsed, and occurs on timescales which are limited by the resolution of the camera (<10ps), and each pulse is spectrally resolution limited as well, so that the spectrum is formed of several quasi-monochromatic pulses, each of

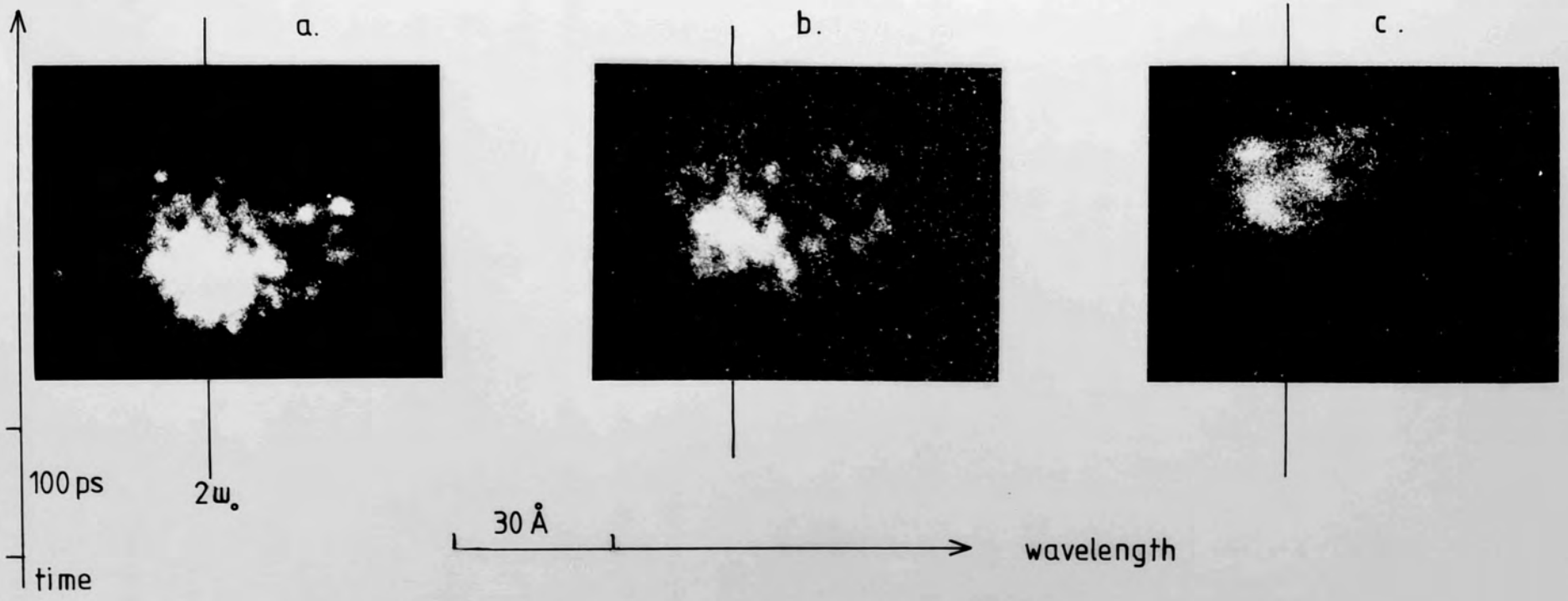

three typical time resolved backscattered $2\omega_0$ spectra.

$E_i \sim 15$ J per beam

temporal resolution ~ 10 ps
spectral " ~ 1.5 Å

Fig. 45.5

duration far less than the incident laser pulse. The occurence of these pulses appears to be completely random and shows no pattern, although a tentative observation may suggest that there is a tendency for the spectrum to move to the red with advancing time. The total duration of the $2\omega_o$ emission is similar to that of the laser pulse. These time resolved spectra are discussed in context with the other data in the next section.

4.6 Discussion.

At the laser intensities used, it was expected that $2\omega_o$ generation due to parametric instability would be by far the dominant process, and the general time integrated spectrum of Fig.4.2.1 displays a red shifted peak and an asymmetric red wing due to the excited ion-acoustic spectrum. The spectral peak red shift may be increased by 4Å since the Doppler shift due to the expanding plasma is of this order; both estimated from simulations and from experiment. This Doppler shift is calculated on the assumption that $2\omega_o$ light is generated 'inside' the expanding plasma, and not within the reflected incident beam, since the electron plasma waves generated are parallel to the density gradient. This spectral peak shift occurs occurs in a position in good agreement with the theory of Silin, since from eqn 3.5.6:

$$\delta\lambda = \left(\frac{Z}{A}\right)^{1/2}\left(20T_e + 7.10^{-15}\phi\left(\frac{L_n}{\lambda_o}\right)^{2/3}\right)^{1/2}$$

which after inserting values pertinent to experiments gives

$\delta\lambda = 19\mathring{A}$

Since this $2\omega_o$ spectral shift from the true harmonic position is a function of the peak laser irradiance, the total spectral width was expected to increase accordingly, as the range of laser irradiances at the critical surface after linear absorption and scattering would be greater the higher the peak intensity of the pulse. This idea is represented for several shots of similar microballoon target configuration and focussing conditions in Fig.4.6.1, and the relationship between the peak red shift and the FWHM spectral width ($\Delta\lambda$). These experimental results agree with an increase in $\delta\lambda$ corresponding to an increase in $\Delta\lambda$, but to a limited extent. For all these spectra, regular modulation of the red sideband is apparent, with a periodicity ~$3\mathring{A}$, and is, as yet, unexplained. The atypical spectrum, shown in Fig.4.2.2 occurs when the target is either of a high Z material, or more often, when it was a thin foil. The former meant that the absorption of the laser beam prior to the critical surface is higher than for lower Z targets, and also the energy loss from the plasma due to bremsstrahlung is greater. This meant that the intensity available at the critical surface is very much reduced, and this is also true for the foil targets, since if 'burnthrough' occurs at a time prior to the peak of the laser pulse, the peak irradiance calculated from the laser pulse and the focal spot size may not be reached, and hence a lower peak intensity will result at the critical surface just prior to burnthrough. These considerations point to the fact that $2\omega_o$

Fig 4.7.1.

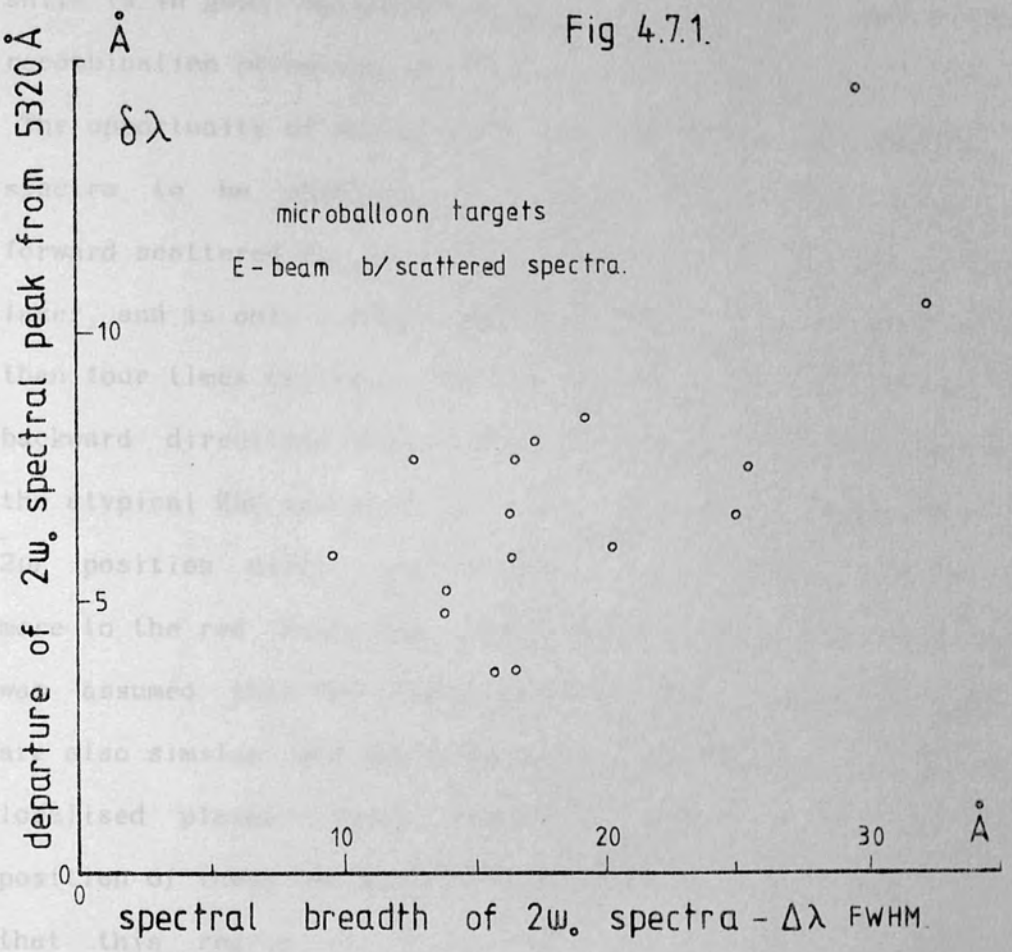

generation due to linear transformation may be the dominant mechanism under these two conditions, where actual intensities are around the threshold for parametric instability. The resultant spectrum is therefore one of narrower width, with a peak which is less red shifted than before, but with a further red shifted sideband, which is probably due to the onset of parametric $2\omega_0$ generation. The narrow peak of this spectrum corresponds to a red shift of ~7Å, which allowing for ~3Å Doppler

shift is in good agreement with the value of plasmon/photon recombination mechanism of ~5Å

The opportunity of using thin foil targets also enabled $2\omega_0$ spectra to be obtained in opposing directions, so that the forward scattered $2\omega_0$ is in the same direction as the incident laser, and is only visible when the peak electron density is less than four times critical. The two spectra from the forward and backward directions show similar features as discussed above for the atypical $2\omega_0$ spectrum, but their peak shifts from the true $2\omega_0$ position differ very slightly, the backscattered one being more to the red. Since the spectra have very similar features, it was assumed that the mechanism(s) responsible for each spectrum are also similar, and hence the emission occurs from the same localised plasma region. Hence the small difference in peak position of these two spectra suggests from the Doppler effect that this region of the plasma is moving inwards, albeit at a velocity $< 10^3$ m/s. This is not an unacceptable solution since as $2\omega_0$ emission can only be generated before the plasma becomes underdense, which is prior to the laser pulse peak, the critical surface is in close proximity to the rear of the target and the motion at this density will be approximately zero. This is supported by simulations of the density profile obtained at different times using the computer code MEDUSA, as in Chapter 7, to obtain general trends of critical surface movement. Three profiles at different times for a 0.4μm foil target are shown in Fig.4.6.2 Immediately apparent from these is the profile

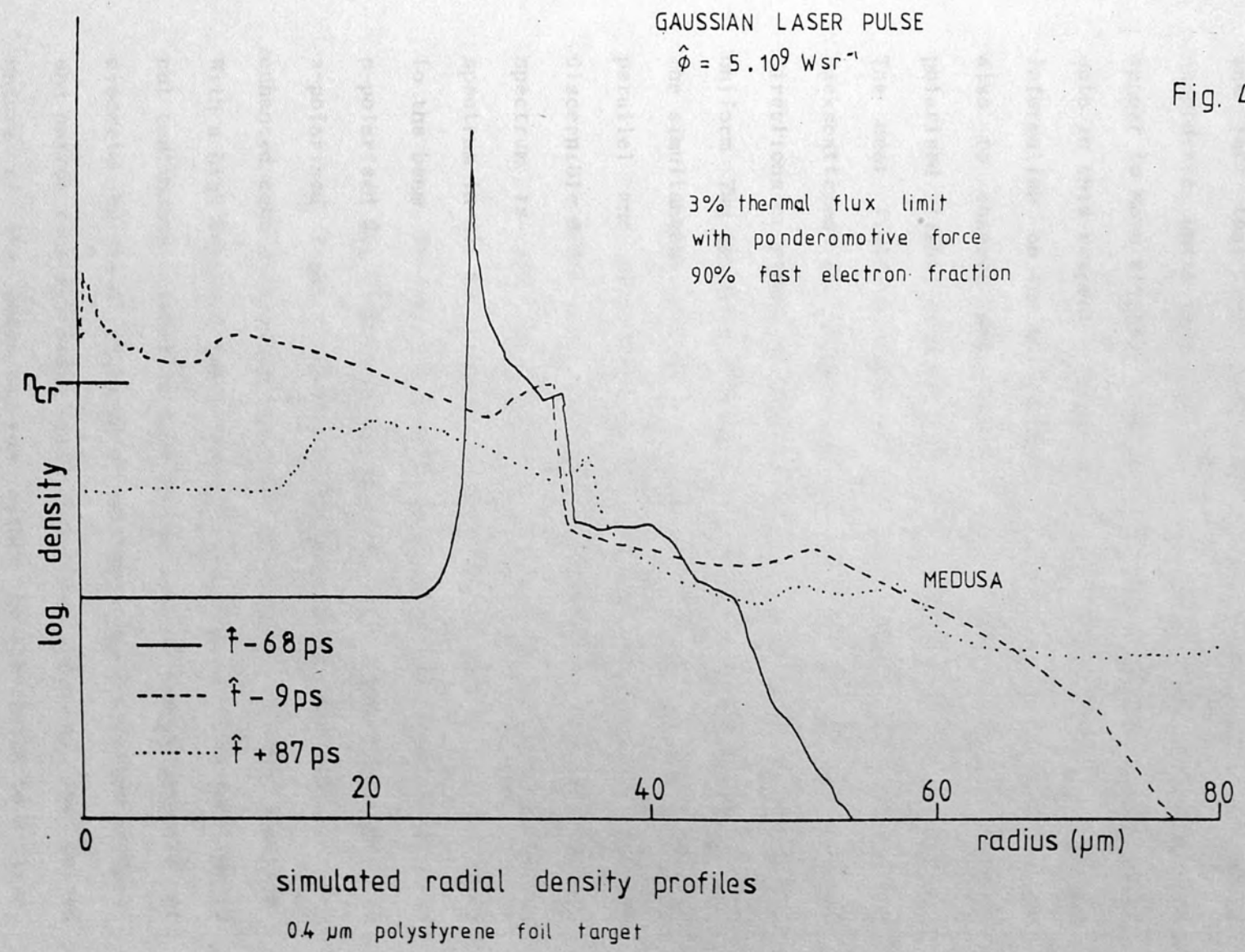

Fig. 4.6.2

simulated radial density profiles

0.4 μm polystyrene foil target

steepening due to the ponderomotive force close to critical, and the fact that this modification persists until the plasma is underdense. Until this occurs too, the critical surface does appear to move slightly inwards, and agrees with the experimental data in this respect. Subsequent experiments sought to obtain information on the polarisation of backscattered $2\omega_0$ emission and also to observe any spectral differences between s and p polarised light with respect to the incident beam polarisation. The near field picture of the focussing lens imaged in backscattered $2\omega_0$ light shows little detail of any preferential directions or planes of emission since the light seems fairly uniform. The incident beam was polarised in the horizontal plane. The simultaneous spectra of light resolved for $2\omega_0$ emission parallel and perpendicular to the incident beam also show few discernible differences. However, the peak of the p-polarised spectrum is red shifted by ~1Å compared with the s-polarised spectrum in all cases when the target was inclined at 45° to the beam. This suggests that the turning point density for the p-polarised $2\omega_0$ light is fractionally lower than that for the s-polarised light. The time integrated $2\omega_0$ spectral data were enhanced considerably by the time resolution of the spectrum. With a high temporal resolution, it was seen that the spectrum is not continuous, either in time or wavelength, and is composed of discrete bursts of emission of extremely short duration (< 10ps), and narrow spectral width (< 1Å) This observation of the pulsed nature of the emission can either be attributed to a 'true'

plasma effect, whereupon the emission rapidly grows in intensity, saturates and decays, all within the temporal resolution of 10ps, or alternatively is due to the rapid motion of an emitting region across the volume subtended by the spectrograph entrance slit on the target: i.e. the region of plasma as seen by the viewing optics. From considerations of the magnification used, the latter explanation neccesitated the localised region of the plasma to move across the field of view with a velocity component in excess of 10^6 m/s, perpendicular to the axis of irradiation and the spectrograph entrance slit. This large value leads to a tentative conclusion that the latter explanation, of a localised plasma region moving with this velocity is improbable, although not impossible, and that the former explanation is worthy of further investigation. Certainly at the laser intensities used in the time resolved work, ($\sim 10^{16}$ W.cm^{-2}), parametric instability was the dominant mechanism. Hence for parametric instability, the fastest growing mode is the one with the largest value of the propagation vector (k) which is not severely Landau damped, and this may be taken as those where

$k\lambda_D \leq 0.25$, where λ_D is the Debye shielding distance.

Hence the plasma waves excited by the parametric decay instability and satisfying this criterion can grow until detuning effect effects limit further growth. These plasma waves will then Landau damp, but in doing so will generate fast electrons since the electrons will be accelerated up to the phase velocity of the electron plasma wave. The production of these fast electrons

means that further Landau damping will occur at larger phase velocities than before, since;

$$k\lambda_D = v_{th} / v_{phase} \quad .$$

The effect of this is to effectively increase the threshold for the decay instability so that a period of time elapses on the leading edge of the laser pulse before this new threshold is exceeded, and hence the $2\omega_o$ emission resulting from recombination involving these plasma waves, is pulsed. The Landau damping decrement for plasma parameters of interest here is shown in Fig.4.6.3 as a function of k of the plasma wave. The growth rate predicted in Chapter 3 for the electron plasma wave amplitude to increase by the exponential e is $2.8\ 10^{14}\ s^{-1}$, so that within the temporal resolution of the streak camera, the wave can grow by over twenty orders of magnitude, so that it is perfectly plausible for the wave to grow, detune, and damp within the time resolution inherent in the experiment.

Fig. 4.6.3.

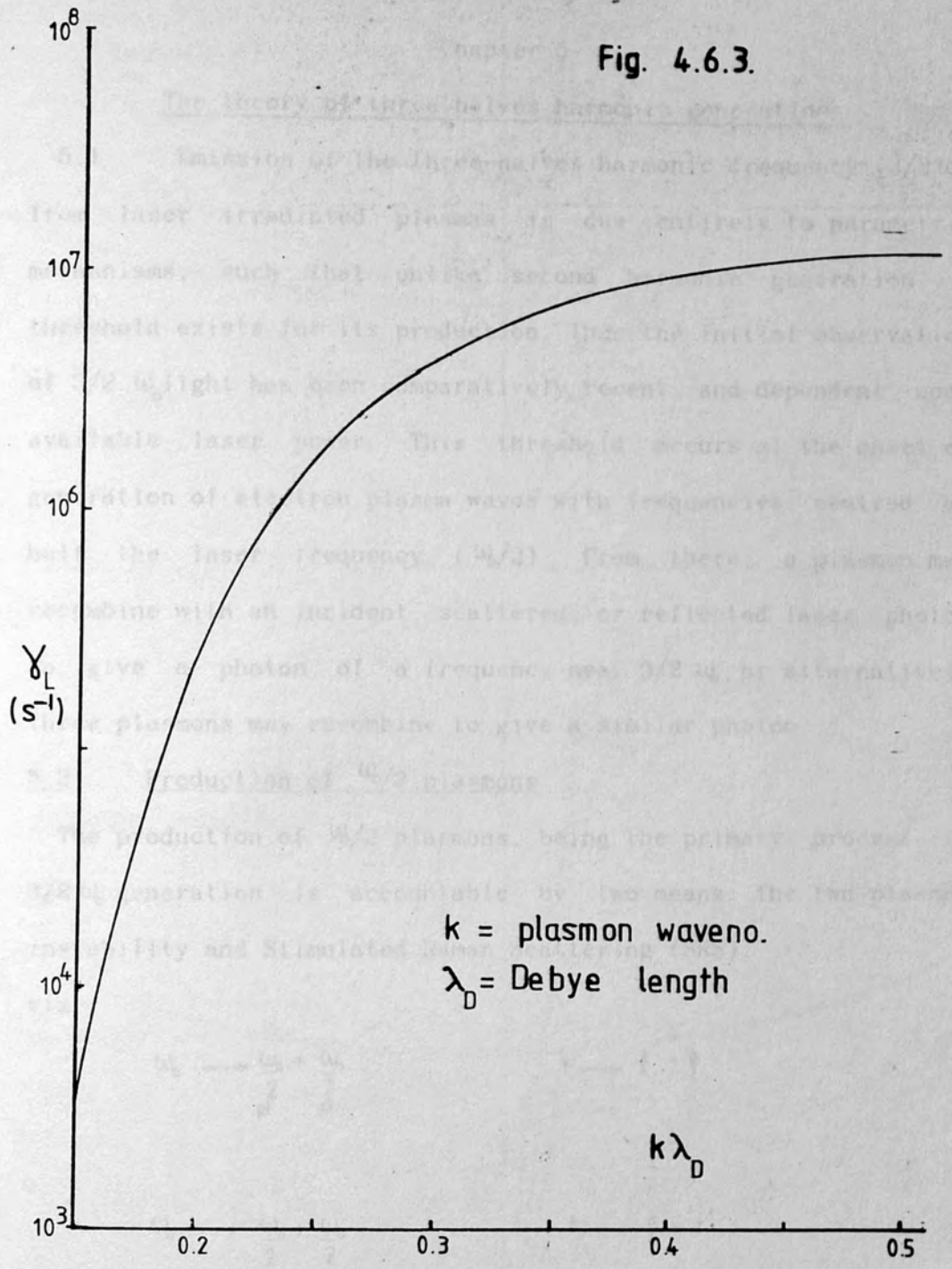

Landau damping decrement (γ_L) - Nd laser.

at critical surface.

typical λ_D for T = 800 eV is 6.7 10^{-9} m. since

$$\lambda_D = \sqrt{\frac{\epsilon_0 k_B T_e}{n_e e^2}}$$

-Chapter 5-

The theory of three-halves harmonic generation.

5.1 Emission of the three-halves harmonic frequency ($3/2\,\omega_0$) from laser irradiated plasmas is due entirely to parametric mechanisms, such that unlike second harmonic generation, a threshold exists for its production. Thus the initial observation of $3/2\,\omega_0$ light has been comparatively recent, and dependent upon available laser power. This threshold occurs at the onset of generation of electron plasma waves with frequencies centred on half the laser frequency ($\omega_0/2$). From there, a plasmon may recombine with an incident, scattered, or reflected laser photon to give a photon of a frequency near $3/2\,\omega_0$, or alternatively three plasmons may recombine to give a similar photon.

5.2 Production of $\omega_0/2$ plasmons

The production of $\omega_0/2$ plasmons, being the primary process in $3/2\,\omega_0$ generation is accountable by two means: the two-plasmon instability and Stimulated Raman Scattering (SRS).

viz.

$$\omega_0 \longrightarrow \underset{pl}{\frac{\omega_0}{2}} + \underset{pl}{\frac{\omega_0}{2}} \qquad t \longrightarrow \ell + \ell$$

$$\omega_0 \longrightarrow \underset{pl}{\frac{\omega_0}{2}} + \underset{ph}{\frac{\omega_0}{2}} \qquad t \longrightarrow \ell + t'$$

For SRS satisfying the frequency and wavenumber matching criteria may be seen graphically in Fig. 5.2.1, where the appropiate dispersion relations are represented for forward and backward

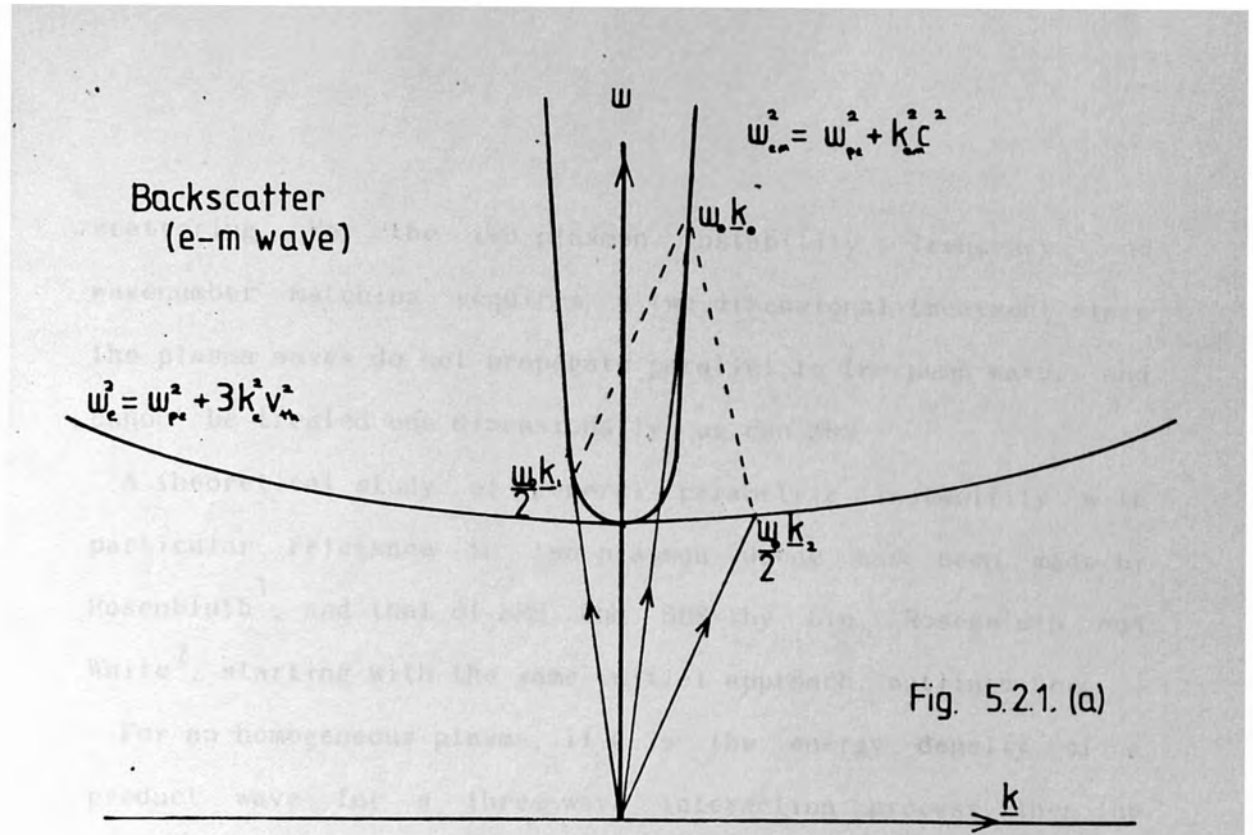

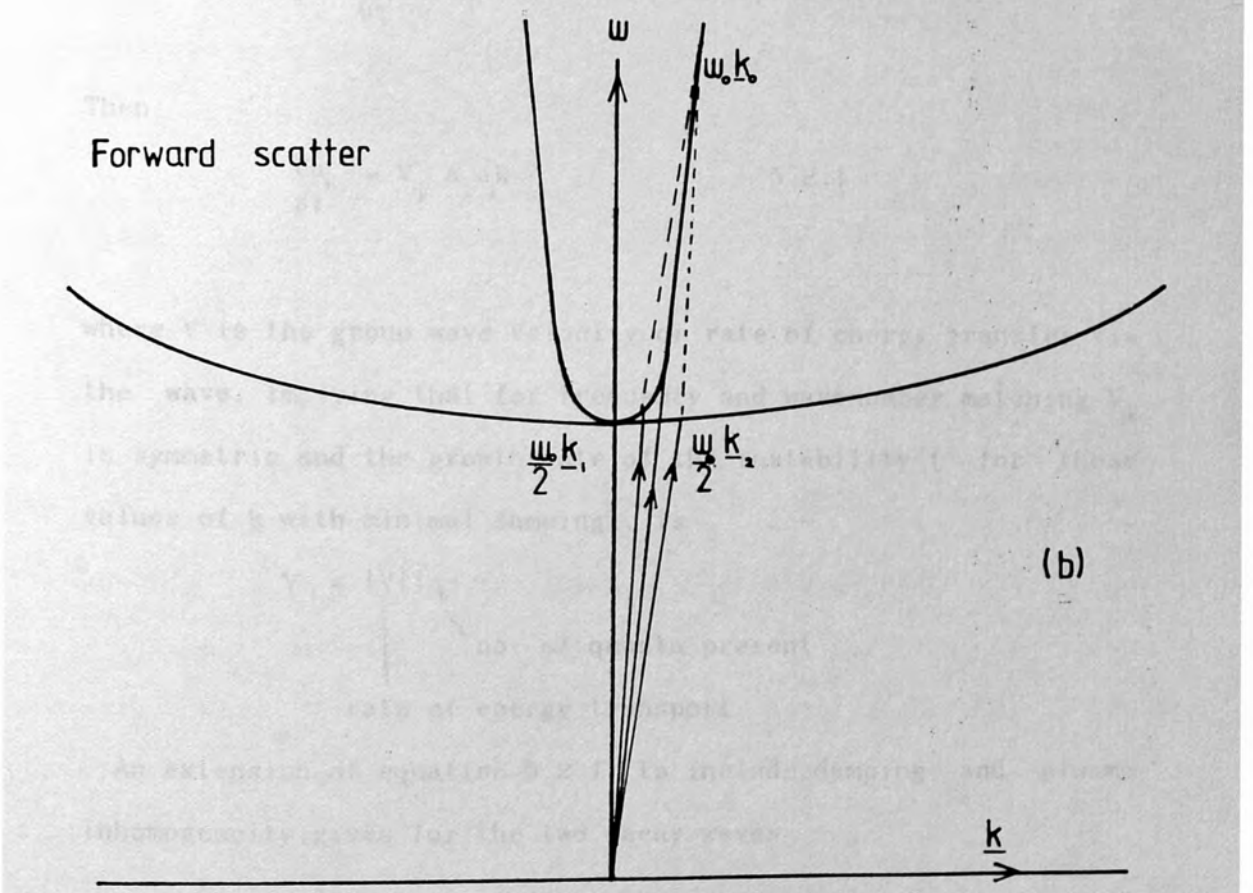

Frequency & Waveno. matching for Stimulated Raman Scattering

$\omega_0 = \omega_1 + \omega_2$, $\quad \underline{k}_0 = \underline{k}_1 + \underline{k}_2$, $(\omega_1 \sim \omega_2 \sim \frac{\omega_0}{2})$

scattering. For the two-plasmon instability, frequency and wavenumber matching requires a two dimensional treatment since the plasma waves do not propagate parallel to the pump wave, and cannot be treated one dimensionally, as can SRS.

A theoretical study of general parametric instability with particular relevance to two-plasmon decay has been made by Rosenbluth[1], and that of SRS and SBS by Liu, Rosenbluth and White[2], starting with the same initial approach, outlined here.

For an homogeneous plasma, if ϵ_i is the energy density of a product wave for a three-wave interaction process, then the action amplitude of that wave,

$$a_i = \frac{\epsilon_i}{\omega_i} \quad = \text{number of quanta present.}$$

Then

$$\frac{da_i}{dt} = V_{ij}\, a_j\, a_k \qquad - 5.2.1.$$

where V is the group wave velocity or rate of energy transfer via the wave, implying that for frequency and wavenumber matching V_{jk} is symmetric and the growth rate of the instability (for those values of $\underline{k}$ with minimal damping), is

$$\gamma = |V||a_o|$$

$|V|$: rate of energy transport; $|a_o|$: no. of quanta present

An extension of equation 5.2.1. to include damping and plasma inhomogeneity gives for the two decay waves :

$$\frac{da_1}{dt} + \nu_1 a_1 + V_1 \frac{da_1}{dz} = \gamma_0 a_2 \exp\left[i\int_0^z K\, dz\right]$$

$$\frac{da_2}{dt} + \nu_2 a_2 - V_2 \frac{da_2}{dz} = \gamma_0 a_1 \exp\left[-i\int_0^z K\, dz\right] + \delta(z)$$

where V_1 and V_2 = group velocities of product waves, assumed oppositely propagating.

and ν_1 ν_2 = respective damping rates

$\delta(z)$ = source due to thermal excitation

K = phase (wavenumber) mismatch = $k_0 - k_1 - k_2$

Laplace transforming these equations in time and using

$$a(p) = \int_0^\infty \exp(-pt)\, a(t)\, dt$$

and inserting initial values and substituting

$$a = \hat{a} \exp\left(\frac{p+\nu_1}{V_1} - \frac{p+\nu_2}{V_2}\right)\frac{x}{2}$$

gives

$$\frac{d^2a}{dx^2} + \frac{1}{4}\left(K - i\left(\frac{p+\nu_1}{V_1} + \frac{p+\nu_2}{V_2}\right)\right)^2 a + \left(\frac{\gamma_0^2}{V_1 V_2} + \frac{1}{2}\frac{dK}{dz}\right) a = \frac{\gamma_0 b\, \delta(z)}{V_1 V_2} \quad - 5.2.2$$

Without the source term on the RHS, this is an eigenvalue equation for a with p its eigenvalue. Analysis of this equation with approximations for K (phase mismatch) variance can give stipulations for the growth and nature of the instabilities.

If $K = K'(z)$, then equation 5.2.2 reduces to the standard form of the parabolic cylinder equation[4], after change of variable.

For this, only spatial amplification is possible, such that the waves must grow substantially during the time it takes to propagate to the point of large phase mismatch. Using a WKB approximation for the solution of the equation shows that wave amplification is given by

$$I = I_o \exp\left(2\pi\gamma_o^2 / V_1 V_2 K'\right)$$

Hence for positive growth, $\frac{2\pi\gamma_o^2}{V_1 V_2 K'} \gg 1$ 5.2.3

For the two-plasmon instability, the growth rate as given by Jackson[3] is:

$$\gamma_o^2 = 1.414\ 10^{14}\left[\frac{e^2}{m^2 c^3}\right] \varnothing_o \text{ with } \varnothing_o \text{ in } W.cm^{-2}$$

and upon inserting this into equation 5.2.3, and substituting for the group velocities determined from the relative dispersion relations, a threshold arises of:

$$\varnothing_o > 1.63\ 10^3 \frac{T_e}{L_n \lambda_o} \quad W.cm^{-2} \qquad 5.2.4$$

where T_e is in keV and L_n, the scalelength is in metres, as is the incident wavelength, λ_o.

For SRS, a higher threshold than that for the two-plasmon instability is envisaged, since convection of energy out of out of the unstable region will be faster via the product electromagnetic wave than via an electrostatic wave. Also at the lower density and higher temperatures suitable for SRS, Landau damping becomes important, unless $k\lambda_D \geq 1/3$, implying that $v_{phase} >$

5. v_{th}.

A simple expression for the growth rate of SRS is shown by Rosenbluth and Sagdeev[5] to be

$$\gamma_o \sim \frac{v_o}{c}\sqrt{\omega_o\,\omega_{pe}} \qquad 5.2.5.$$

indicating the gain to increase with electron density. For both the two-plasmon instability and SRS the region of the plasma unstable to both these processes is where plasma waves of frequency $\sim\frac{\omega_o}{2}$ can be supported, and this corresponds to an electron density near a quarter critical, since $\omega_{pe} \propto n_e^{1/2}$. Hence these two mechanisms are important as a possible means of diagnosing instability in the quarter critical region, where incident laser energy may be reflected or re-radiated before it reaches the critical surface and can be efficiently absorbed. The plasma frequency in expression 5.2.3 is $\frac{\omega_o}{2}$ and inserting this growth rate into equation 5.2.3 gives an intensity threshold for SRS as:

$$\phi > 2.\ 10^{16}\ W.cm^{-2}$$

which is superior to thresholds for other parametric processes.

For the experiments using Nd laser light ($\lambda_o = 1.06\mu m$) and a nominal 20μm density scalelength, the thresholds may be summarised as:

$$\phi_{2.pl} > 6.\ 10^{13}\ W.cm^{-2}$$

$$\phi_{srs} > 2.\ 10^{16}\ W.cm^{-2}$$

so that the two-plasmon decay is far more likely to be the primary mechanism for $3/2\,\omega_o$ generation, and as such, the dispersion relation of the plasmons produced by the two-plasmon

decay is of interest in deducing the characteristics of the $3/2\,\omega_0$ light formed by various recombination schemes. Denoting the two plasmons with subscripts 1 & 2, the wave matching requires

$$\omega_0 \longrightarrow \omega_1 + \omega_2 \quad , \text{ and } \quad k_0 \rightarrow k_1 + k_2$$

For an electron plasma wave, the Bohm-Gross equation for the dispersion relation is:

$$\omega_{bg}^2 = \omega_{pe}^2 + 3\, k_i^2 v_e^2 \quad , \qquad i = 1,2.$$

hence

$$\omega_1^2 - \omega_2^2 = (\omega_1 + \omega_2)(\omega_1 - \omega_2) = (\omega_1 - \omega_2)\omega_0 = 3\, v_e^2 (\, k_1^2 - k_2^2\,)$$

$$\omega_1 - \omega_2 = 3\, v_e^2 \frac{(\, k_1 - k_2\,)(\, k_1 + k_2\,)}{\omega_0} = 3\, \frac{v_e\, k_0\, (\, k_1 - k_2\,)}{\omega_0}$$

If each of the decay waves is resolved along the path of k_0, then each plasmon may differ from $k_0/2$ by a factor K, such that

$$k_{1z} = \frac{k_0}{2} + K \qquad k_{2z} = \frac{k_0}{2} - K \quad .$$

Then

$$k_0 .(\, k_1 - k_2\,) = k_0 \left(\left(\frac{k_0}{2} + K \right) - \left(\frac{k_0}{2} - K \right) \right) = 2\, \underline{k}_0 . \underline{K}$$

As $\omega_0 = \omega_1 + \omega_2 = 2\omega_1 + (\,\omega_2 - \omega_1\,)$, then

$$\omega_1 = \frac{\omega_0}{2} + \frac{(\omega_1 - \omega_2)}{2} = \frac{\omega_0}{2} + 3\, \frac{v_e^2\, K\, k_0}{\omega_0} \qquad 5.2.6$$

As well as the dispersion relation, the plasmons which are preferentially excited will give peaks to the $3/2\,\omega_0$ spectrum which is produced, and these correspond to those plasmons with maximum growth rate. From the work of Liu and Rosenbluth[6], an extension of that by Rosenbluth[1], described earlier, an expression arises for the plasmon growth rate of the two plasmon decay as a function of the plasmon wave number. Taking plasma

inhomogeneity, Landau damping, and collisional damping into account, this expression is:

$$\gamma = \underbrace{\frac{k_o |v_o|}{2}}_{1} - \underbrace{\frac{(2n+1)\omega_{pe}}{2k_y L_n}}_{2} - \underbrace{\frac{\omega_{pe}\sqrt{\pi}}{k^3\lambda_D^3}\exp\left(-\frac{1}{2k^2\lambda_D^2} - \frac{3}{2}\right)}_{3} - \underbrace{\nu_{ei}}_{4}$$

where

1 = growth rate of absolute instability.

2 = reduction term for plasma inhomogeneity.

3 = Landau damping decrement.

4 = collisional damping decrement.

To determine the k value of the plasmon with maximum growth rate, the first derivative of this expression is put equal to zero (w.r.t. k), to determine this position, and this gives:

$$K^2 = \frac{k_o^2}{4} + k_y^2 \quad .$$

This condition is used later to determine the position of peaks in the postulated spectral distributions.

5.3 <u>3/2 ω_o generation from $\omega/2$ plasmons.</u>

Subsequent 3/2 ω_o generation can occur either by the recombination of an excited plasmon with a photon, or alternatively three plasmons may coalesce.

viz

$$\omega_{o_{ph}} + \frac{\omega_o}{2}_{pl} \longrightarrow \frac{3}{2}\omega_{o_{ph}} \quad , \qquad t + \ell \longrightarrow t'$$

or

$$\frac{\omega_o}{2}_{pl} + \frac{\omega_o}{2}_{pl} + \frac{\omega_o}{2}_{pl} \quad \frac{3}{2}\omega_o \quad . \qquad \ell + \ell + \ell \longrightarrow t$$

The recombining photon may be either incident, scattered, or reflected, and if scattered, then the process of Stimulated Brillouin Scattering (SBS) will mean that the photon will be downshifted in frequency. Avrov et al[7] discuss the three plasmon and incident photon/ plasmon recombination processes, and develop expressions for the spectral composition of $3/2\ \omega_o$ light and the dependence of this spectrum upon angle of observation. Their starting point is the tensor equation for the non-linear interaction between plasma waves and electromagnetic waves in plasmas, as as deduced by Pustuvalov and Silin[8] in their review article. This uses the assumption that the region of parametric instability is much less than the mean free path of the laser light with respect to electron-ion collisions.

i.e.

$$\frac{c}{\nu_{ei}} \gg \delta z$$

This criterion is satisfied for plasmas of moderate temperature (< 15 keV), but another assumption of their analysis is that it is only valid for short wavelength plasmons ($k \gg k_o$), which is not true for the case of interest here, well above threshold.

However, a more general approach as developed by Barr[10] is outlined here, which considers all four possible recombination schemes, and uses the dispersion relation of plasmons produced by two-plasmon decay as a starting point to determine $3/2\ \omega_o$

spectral characteristics.

From the dispersion relations of an incident electromagnetic wave at ω_o and a scattered e-m wave of frequency $3/2\,\omega_o$,

$$\omega_o^2 = \omega_{pe}^2(z) + k_o^2 c^2 \quad , \quad \omega_{3/2}^2 = \omega_{pe}^2(z) + k_{3/2}^2 c^2$$

it can be seen that at quarter critical, ($\omega_{pe} = \omega_o/2$)

$$\frac{3}{4}\omega_o^2 = k_o^2 c^2 \quad \text{and} \quad 2\omega_o^2 = k_{3/2}^2 c^2$$

so that

$$\frac{k_{3/2}}{k_o} = \sqrt{\frac{8}{3}} \qquad 5.3.1$$

Since it is the peaks of experimental spectra which provide the most easily determinable feature, these correspond to the plasmon frequency with the largest growth rate, and as shown previously this corresponds to those plasmons whose k vectors can satisfy

$K^2 = \frac{k_o^2}{4} + k_y^2$, where $k_y = k_{3/2}\sin\Theta = k_s \sin\Theta$.

-the subscript s denoting the scattered photon and Θ is the angle between k_o and k_s.

Recombination mechanisms.

1. Ingoing photon + plasmon.

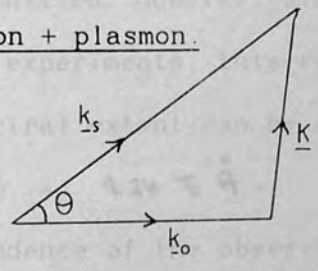

resolving components in the z direction

$$k_s \cos\Theta = k_o + k_z$$

$$k_s \sin\Theta = k_y \quad , \quad k_z = \frac{k_o}{2} + K$$

From the dispersion relation for the plasmon (eqn 5.2.6), a departure of the angular frequency of the $3/2\,\omega_o$ light from its

true position is given by :

$$\frac{\delta\omega}{\omega_o} = \frac{3\,K\,k_o\,v_e^2}{\omega_o} = \frac{9}{4}\frac{v_e^2}{c^2}\left(\sqrt{\frac{8}{3}}\cos\Theta - \frac{3}{2}\right)$$

since $\frac{k_s}{k_o} = \sqrt{\frac{8}{3}}$

Hence $\delta\lambda = -33.8\,(\cos\Theta - 0.92)\,T_e$ Å 5.3.3

where T_e is in keV. This is the anticipated spectral shift, assuming all the possible plasmons are excited. Hence this $3/2\omega_o$ spectrum is a function of the angle of emission. If equation 5.2.7 is taken to determine the peaks in this spectrum, then

$$\left(k_s\cos\Theta - \frac{3k_o}{2}\right)^2 = \frac{k_o^2}{4} - k_s^2\sin^2\Theta \quad , \text{ since } k_y = k_s\sin\Theta$$

and hence $\cos\Theta = -0.136$ and $\Theta = 97^\circ$.

Substituting this into equation 5.3.3 gives a red-shifted peak of

$$\delta\lambda = 35.2\,T_e \text{ Å} \qquad 5.3.4$$

Hence the recombination of an ingoing photon and an excited plasmon is expected to yield components on both the red and blue shifted sides of the true harmonic frequency, with a peak occuring at an angle of 97° to the incident wave vector, this peak being red shifted. However, since f/1 lenses were the lowest f/no used in experiments, this red peak would not be seen, and the maximum spectral extent can be estimated to be $2.\delta\lambda(\Theta)$ where Θ = 2 x arctan 0.5, = $9.24\,T_e$ Å.

With the dependence of the observed $3/2\,\omega_o$ spectrum on the angle between the direction of emission and the incident wave vector, account must be taken of the modification of this idealised picture due to the plasma inhomogeneity. In a plasma formed from a solid target, there must exist, even if only for a very short

time, an electron density which corresponds to the critical density for $3/2\,\omega_o$ light, which is 9/4 times as dense as the critical density for the fundamental light, i.e. n_{cr}. Hence any $3/2\,\omega_o$ light travelling towards this density will be classically reflected and so complicate the spectrum for any given observation direction. For the direction of backscatter ($\theta = 180^{\circ}$), any forward scattered light will be reflected as shown in Fig 5.3.1.a, so that it will emerge at the same acute angle as if directly backscattered. However, in travelling to this $9/4\ n_{cr}$ surface and returning, the $3/2\,\omega_o$ light will encounter absorption, and will be less intense than a similar backscattered wave. This fact may be used to estimate density scalelengths due to the difference in intensity between blue and red shifted wings, and the general idea of directional dependence should enable the determination of the appropiate recombination mechanism(s).

2. Specularly reflected photon + excited plasmon recombination.

With a similar analysis to the previous case:

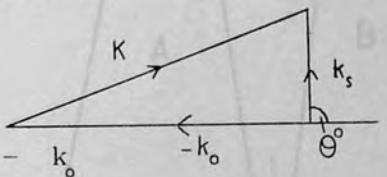

$$k_s \cos\theta = k_z - k_o$$

$$k_s \sin\theta = k_y$$

$$\frac{\delta\omega}{\omega_o} = \frac{9}{4}\left(\frac{v_o}{c}\right)^2\left(\frac{k_s}{k_o}\cos\theta + \frac{1}{2}\right)$$

$$\delta\lambda = -33.8\,(\cos\theta + 0.31)\,T_e\ \text{Å} \qquad -5.3.5$$

The criterion for the plasmons with maximum growth rate is again:

geometry for forward & backscattered $\frac{3}{2}\omega_0$ light in a linear density profile.

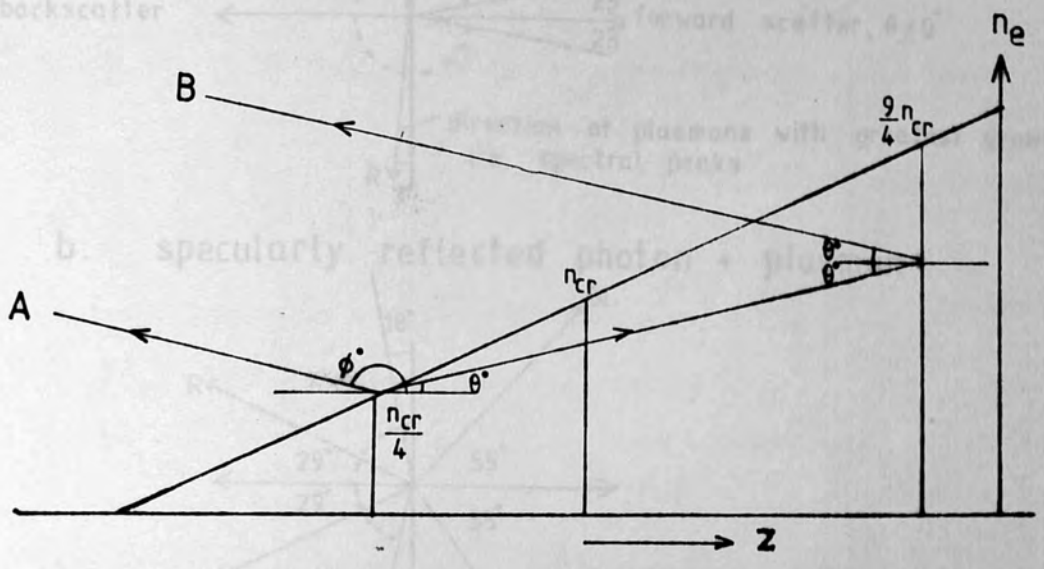

Fig. 5.3.1 a.

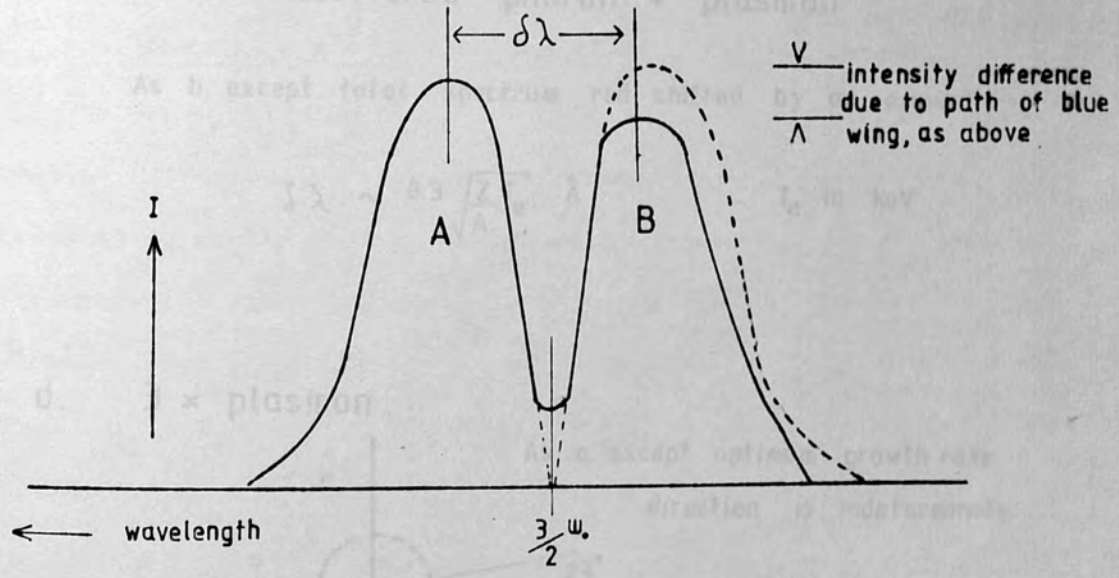

predicted $\frac{3}{2}\omega_0$ spectrum due to plasmon & reflected or scattered photon recombination - (after Barr[10], geometry as above).

Fig. 5.31.b.

a. Ingoing photon + $\frac{\omega_0}{2}$ plasmon recombination

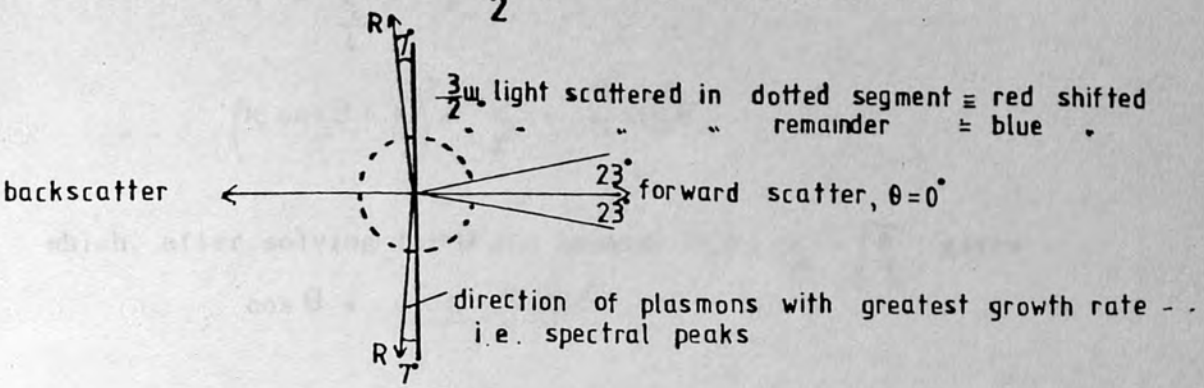

b. specularly reflected photon + plasmon

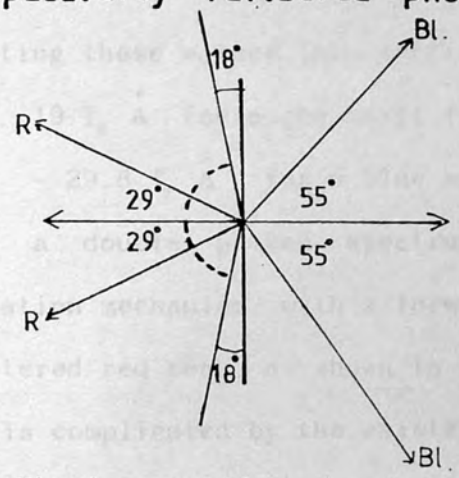

c. Brillouin scattered photon + plasmon

As b. except total spectrum red shifted by an amount

$$\delta\lambda \sim 8.3\sqrt{\frac{Z}{A}T_e}\ \text{Å} \qquad \text{-- } T_e \text{ in keV}$$

d. 3 × plasmon

As a. except optimum growth rate direction is indeterminate.

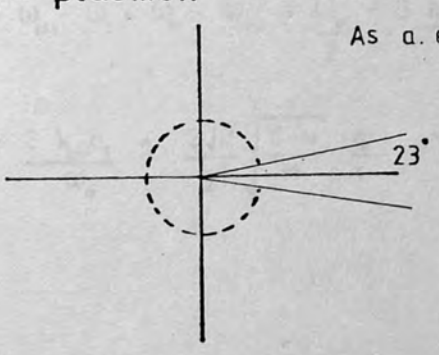

Predicted $\frac{3}{2}\omega_0$ spectral compositions for possible recombination mechanisms. (after Barr[10])

$$K^2 = \frac{k_o^2}{4} + k_y^2 ,$$

$$\therefore \quad \left(k_s \cos\theta + \frac{k_o}{2}\right)^2 = \frac{k_o^2}{4} + k_s^2 \sin^2\theta$$

which, after solving for θ and knowing that $\frac{k_s}{k_o} = \sqrt{\frac{8}{3}}$, gives:

$$\cos\theta = \frac{0.31 \pm \sqrt{2.094}}{2}$$

$$\theta = 151^\circ \text{ or } 55^\circ .$$

On inserting these values into expression 5.3.4 gives:

$\delta\lambda = 19\ T_e$ Å for a red shift from $3/2\ \omega_o$

$\delta\lambda = -29.8\ T_e$ Å for a blue shift from $3/2\ \omega_o$

so that a double peaked spectrum is predicted for this recombination mechanism, with a forward scattered blue peak and a backscattered red peak, as shown in Fig 5.3.1 b although this picture is complicated by the existence of the 9/4 n_{cr} surface, as mentioned previously.

3. Excited plasmon + photon generated by SBS recombination.

The $3/2\ \omega_o$ emission generated by this scheme has a similar angular distribution to the previous case, except that the recombining photon has a downshifted frequency equal to the frequency of the incident laser minus that of the excited ion acoustic wave.

$$\omega_{3/2} = \omega_{sbs} - \omega_s = \omega_o - \omega_{ia} + \frac{\omega_o}{2} + 3\frac{k_o K v_e^2}{\omega_o}$$

$$\frac{\omega_{ia}}{\omega_o} = \frac{2\ k_o\ c_s}{\omega_o} = \frac{2\sqrt{2}}{2}\sqrt{\frac{Z\ m}{M}}\ \frac{v_e}{c} = 1.77\ 10^{-3}\sqrt{\frac{Z}{A}\ T_e}$$

$\therefore \quad \delta\lambda = + 8.3 \sqrt{\frac{Z}{A} T_e}$ Å toward the red in addition to the spectrum of case '2'.

4. Three-plasmon recombination.

Again, using an identical analysis to '1'.

$$\omega = \sum_{i=1}^{3} \omega_i = \frac{3\omega_o}{2} + \left(\sum_{i=1}^{3} K_i \right) 3 \frac{k_o v_e^2}{\omega_o}$$

$$k_s \cos\Theta = \Sigma k_{iz} = 3 \frac{k_o}{2} + \Sigma K_i \quad , \qquad \Sigma K_i = k_s \cos\Theta - \frac{3}{2} k_o$$

$$k_s \sin\Theta = \Sigma k_{iy}$$

which gives:

$$\delta\lambda = - 33.8 \, (\cos\Theta - 0.92) \, T_e \quad \text{Å}$$

This is exactly the same angular dependence as that for the ingoing photon and plasmon recombination, but determination of any spectral peaks cannot be done since there only exists 5 equations in 6 unknowns. However, these recombining waves offer a greater flexibility in phase matching, even if only the optimally growing modes are included, and this scheme is more probable even if it is of higher order. A summary of the characteristics of the four schemes is shown in Fig 5.3.1(b)

5.4 Experimental work to date.

Probably the first observation of $3/2\ \omega_o$ emission from a laser produced plasma was by Bobin et al[11], who used a 2ns Nd laser pulse incident upon a plane polythene target. A single peak $3/2\ \omega_o$ spectrum was observed but similar spectra have not been reported by other authors. SRS as a mechanism for $3/2\ \omega_o$ generation also produces photons of frequency $\sim \frac{\omega_o}{2}$, the observation of these photons may be taken as a signature of SRS. However, Bobin et al

report the only observation of such emission (@ 2.12μm for an Nd laser), and Ping Lee et al[12] deduce from their own experiments that as $3/2\,\omega_o$ emission is more than an order of magnitude greater than the threshold of detectability for any $\frac{\omega_o}{2}$ emission, then SRS can be neglected as a possible mechanism for subsequent $3/2\,\omega_o$ generation in favour of the two-plasmon decay.

Experimental observations of $3/2\,\omega_o$ light are not copious and of the six reports of such emission to date[11-16], widely varying values of the conversion efficiency from fundamental to $3/2\,\omega_o$ harmonic are reported, albeit under various target parameters and laser pulse lengths. Of these six reports, two with a CO_2 laser[16,19], five observe a double peaked spectrum with the blue shifted wing narrower and less intense than the red shifted wing. Two other observations of $3/2\,\omega_o$ emission have been spatially resolved[17,18], so that the expanding quarter critical surface(s) may be 'traced', in a similar manner to the critical surface using $2\omega_o$ light. From equations 5.3.1 & 5.3.4, it can be seen that the peak to peak spectral width is a function of the electron temperature, so that $3/2\,\omega_o$ spectra showing this double peaked structure can be used to obtain a value for the electron temperature. Bychenkov et al[20] show reasonable agreement between this temperature and that obtained from X-ray measurements, but Garban et al[16] notice poor agreement in their work.

A particularly interesting experiment by Offenberger et al[19] is the only one to use a preformed plasma, and this is heated by a CO_2 laser. Due to the nature of this plasma in having a peak electron

density less than $9/4\ n_{cr}$, only the red wing of the $3/2\,\omega_o$ spectrum is visible in the backward direction, in line with the previous theory, although no details of any forward scattered $3/2\,\omega_o$ emission are given.

A fairly comprehensive table of the experimental observation of $3/2\,\omega_o$ emission to date is shown in Table 5.4.1, all experimental details being recorded where available.

$\frac{3}{2}\omega_o$ emission observed in laser-plasma experiments

EXPT & REF no.	INCIDENT LASER PULSE.					target (μb = microballoon)	$\frac{I_{\frac{3}{2}}}{I_o}$	$\frac{3}{2}\omega_o$ SPECTRAL DETAILS.	
	λ_o (μm)	FWHM $\Delta\lambda$ Å	E (J)	Δt	I_o W.cm^{-2}			Double peak? if so, $\delta\lambda$(p-p)	
BOBIN et al[11]	1.06	30	15	15 ns	$\sim 4.10^{13}$	H_2	—	NO	single peak. asym. red broadening. $\Delta\lambda \sim 80$ Å
Ping Lee et al[12]	1.06	3	~ 5	25 ps	$\sim 10^{16}$	$(CH_2)_n$	$2-7 \times 10^{-3}$	—	no spectral detail reported — only b/s intensities for several angles.
AVROV et al[13]	1.06	10	110	2.5 ns	$\sim 10^{16}$	μb.	10^{-7}	yes 22-45 Å	blue peak less intense. $\Delta\lambda_{red}$ — 15-32Å $\Delta\lambda_{blue}$ 7-13Å
JACKEL et al[17]	1.06	—	4×50	200-600 ps	$>10^{15}$	μb	10^{-4}	——	—— only spatial detail —— similar conversion efficiencies for $2\omega_o$ & $\frac{3}{2}\omega_o$
PANT et al[14]	1.06	30	0.1-20	5 ns	$<4.10^{14}$	D_2, C, Cu.	10^{-5}	yes	steep gain curve above threshold of $2\omega_{pe}$ decay. increase in $\delta\lambda_{red}$ with target Z noticed.
GARBAN et al[16]	10.6	—	40	40 ns	10^{12}	$(CH_2)_n$	$\sim 10^{-8}$	yes ~120 Å	red peak broader & more intense than blue peak $\hat{\delta\lambda}_r \sim 80$ Å $\hat{\delta\lambda}_b \sim 35$ Å also steep gain above threshold.
OFFENBERGER et al[19]	10.6	—	50	40 ns	$5\ 10^{11}$	underdense gas	$3\ 10^{-7}$	NO	red peak only — as expected for underdense plasma.
ALEKSANDROV et al[15]	1.06	—	—	3.5 ns	2.10^{13} - 2.10^{14}	$(CH_2)_n$ Al	—	yes 30-50 Å	shift of peaks dependent on target material. blue peak less intense.
BYCHENKOV et al[20]	1.06	10	100-120	~ 1 ns	10^{14}	μb	—	yes	time resolved $\Delta t \sim 100$ ps. no detail apparent otherwise same expt as Avrov et al.

Fig. 5.4.1

Chapter 5 - References.

1. M N Rosenbluth, Phys. Rev. Letts, 29, 565, 1972

2. C S Liu, M N Rosenbluth, & R B White, Phys. Fluids, 17, 6, 1974

3. E A Jackson, Phys. Rev. A, 153, 235, 1967

4. J C P Miller, Tables of Weber Parabolic Cylinder Functions; HMSO 1955

5. M N Rosenbluth & R Z Sagdeev, Comm. on Plasma Phys. & Contr. Fusion, 1, 129, 1972

6. C S Liu & M N Rosenbluth, Phys. Fluids, 19, 7, 1976

7. A I Avrov, V Yu Bychenkov, O N Krokhin, V V Pustuvalov, A A Rupasov, V P Silin, G V Sklizkov, V T Tikhonchuk & A S Shikanov, Sov. Phys. JETP, 45, 3 1977

8. V V Pustuvalov & V P Silin, Proc.(TRUDY) P N Lebedev Inst. 61, 42 1972

9. V V Pustuvalov, V P Silin & V T Tikhonchuk, Sov. Phys. JETP 38, 938, 1974

10. H C Barr, Rutherford Laboratory Report RL-79-036, Section 8.3.8 p8.12, 1979

11. J L Bobin, M Decroisette, B Meyer & Y Vitel, Phys. Rev. Letts. 30, 13, 1973

12. Ping Lee, D V Giovanelli, R P Godwin & G H McCall, Appl. Phys. Letts, 24, 9, 1974

13. A I Avrov et al (authors as in ref. 6) JETP Letts, 24, 5, 1976

14. H C Pant, K Eidmann, R sigel & P Sachsenmaier, Opt. Comm,

16, 3, 1976

15. V V Aleksandrov, V D Vikharev, V P Zotov, N G Koval'skii & M I Pergament, JETP Letts, 24, 10, 1978

16. C Garban, E Fabre, C Stenz, C Popovics, J Virmont & F Amiranoff, J. de Physique-Letts, 39, p16, 1978

17. S Jackel, B Perry & M Lubin, Phys. Rev. Letts, 37, 2, 1976

S Jackel, J Albritton & E Goldman, Phys. Rev. Letts, 35, 8, 1975

18. T Leonard & R Cover, KMS Fusion Inc.,Annual Report 1977 Sect. 2.5

19. A A Offenberger, A Ng, L Pitt & M R Cervenan, Phys. Rev. A, 18, 2, 1978

20. V Yu Bychenkov, Yu A Zakhorenkov, O N Krokhin, A A Rupasov, V P Silin, G V Sklizkov, A N Starodub, V T Tikhonchuk & A S Shikanov, JETP Letts, 26, 6, 1977

-Chapter 6-

Experimental investigation of three-halves harmonic emission.

6.1 Observation of the three halves harmonic was possible with available laser power capable of exceeding the threshold intensity for the two-plasmon instability and approximately equalling it for SRS. As for the second harmonic studies, both time integrated and time resolved studies were performed, the latter with time resolution ~15 ps, necessary again at the high power intensities used on target if any structure was to be seen within the laser pulse duration of nominally 100 ps FWHM Gaussian.

6.2 Time Integrated spectral and spatial studies of $3/2\omega_0$ emission.

6.2.1 Initial experiments to determine $3/2\omega_0$ spectral distribution.

Several time integrated $3/2\omega_0$ spectra were recorded using the experimental arrangement of Fig. 4.1.1. with a Soro main focussing lens and multi-element relay lenses after the final turning mirror, (a_1). These were taken from planar and microballoon targets with irradiances exceeding 10^{15} W.cm^{-2}. Two examples of spectra, obtained at similar power levels and focussing conditions with microballoon targets appear in Figs.6.2.1 (a) and (b), obtained with a spectral resolution ~5Å.

All the spectra observed exhibited a double peaked structure, with a peak red-shifted from the true $3/2\omega_0$ harmonic and the other peak blue-shifted. The SORO lens was corrected for 1.06μm

typical $\frac{3}{2}\omega_0$ spectrum

Fig. 6.2.1. a

microballoon target, $E_l \sim 8.0$ J per beam

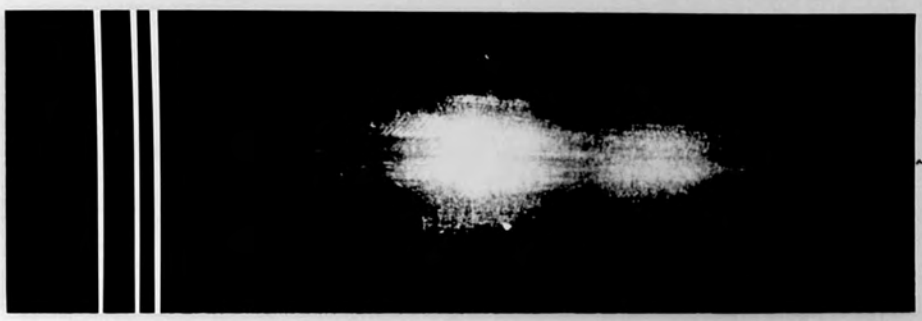

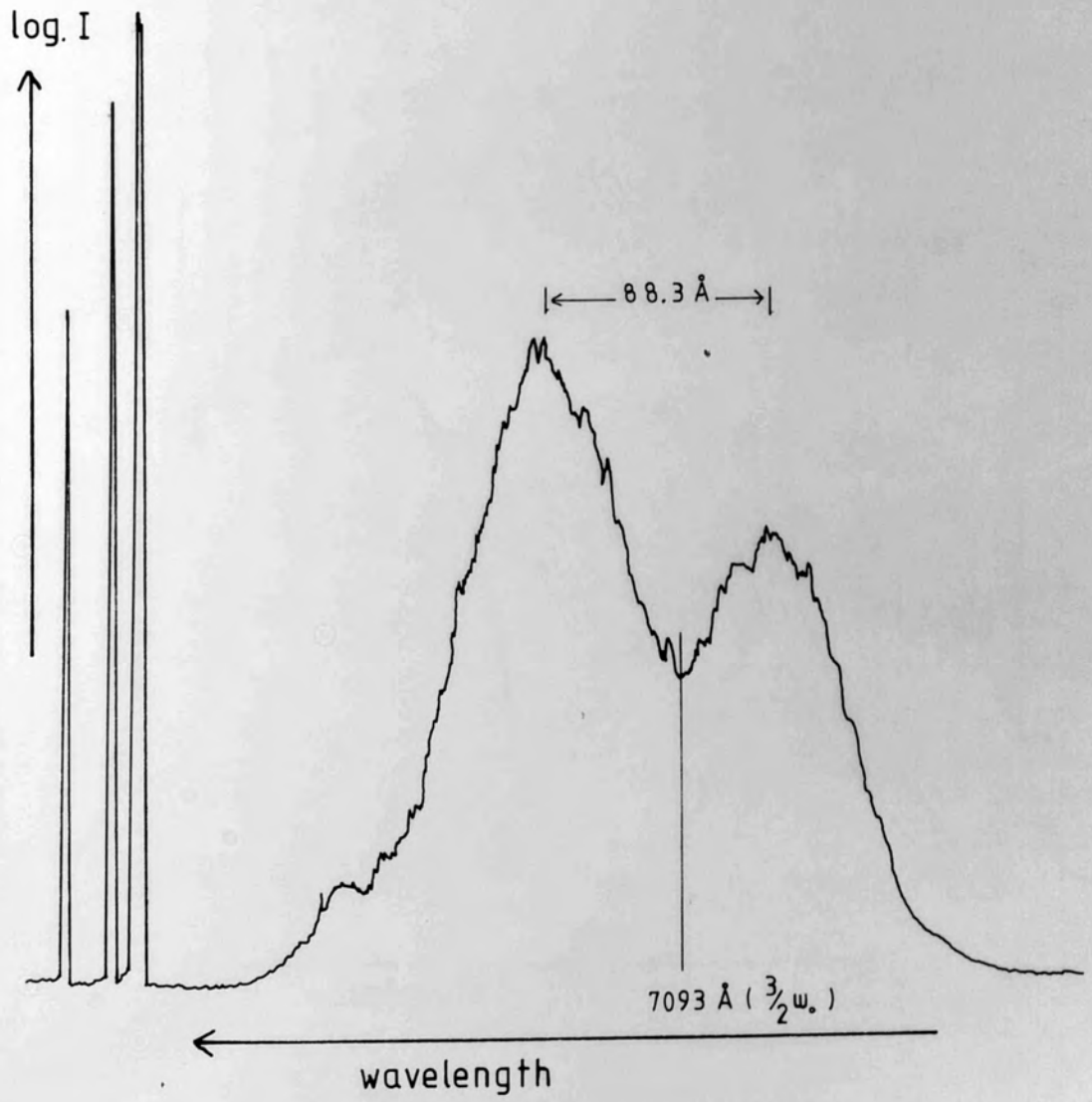

typical $\frac{3}{2}\omega_0$ spectrum

Fig. 6.2.1. b

microballoon target $E_i \sim 8.0$ J per beam

this spectrum has the maximum peak-peak width observed.

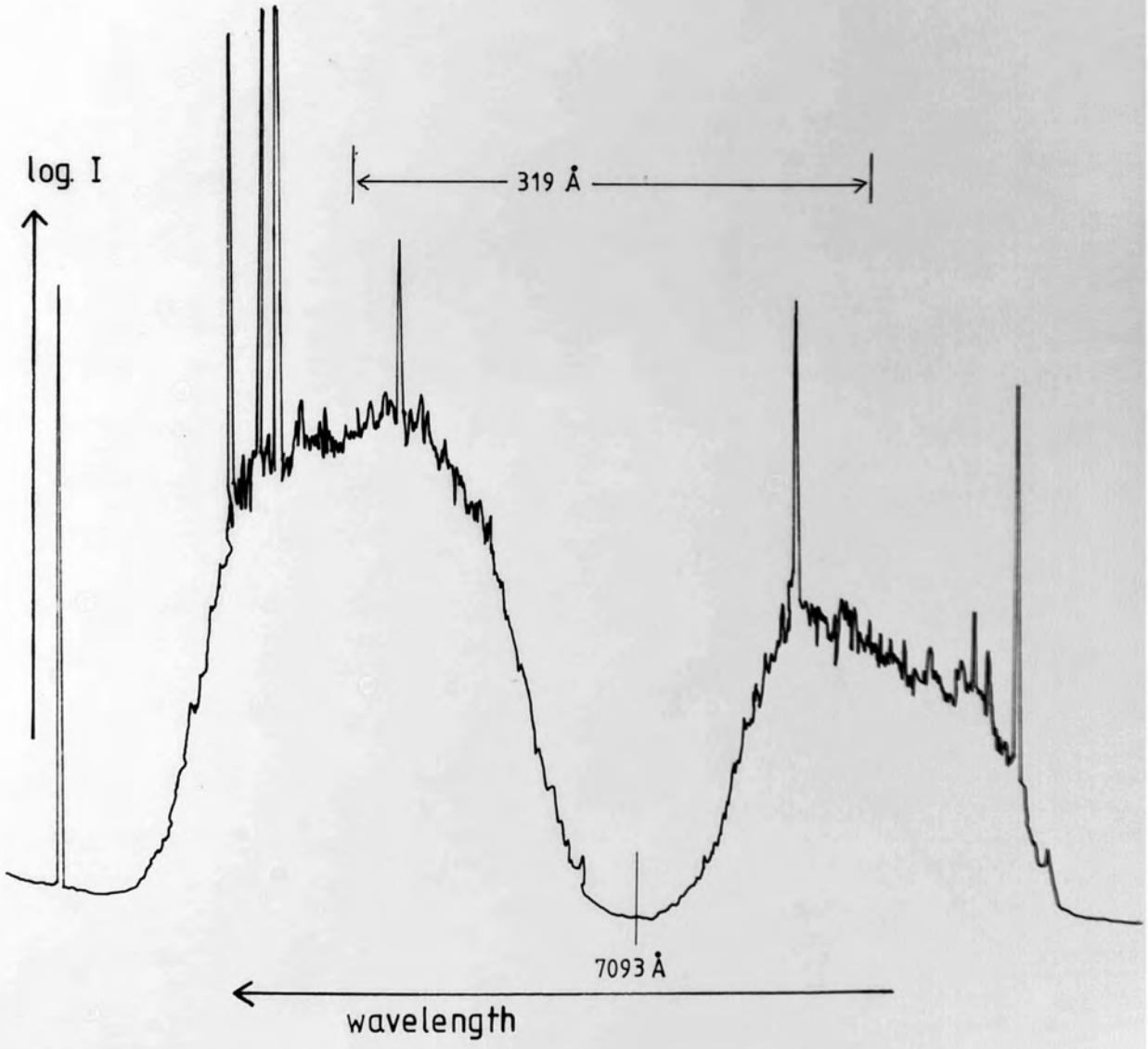

and suffered severe chromatic aberration @ 7093 Å. The red shifted peak was found to be more intense than the blue peak, and suffered greater displacement from $3/2\omega_0$. From records obtained with similar irradiances, focussing conditions and targets, the spectral displacement may be represented as shown in Fig.6.2.2(b) and a mean ratio of red peak shift to blue peak shift of~1·4 may be obtained from the gradient. However, as the quarter critical surface is expanding towards the spectrograph, a correction must be made for the expected Doppler blue shift. It is found that the +4 A blue shift on the y-axis in Fig.6.2.2(b) corresponds to an expansion velocity of the quarter critical density of $\sim 1.6\ 10^{5}$ m/s, and it will be seen that this value is in close agreement with that obtained by using MEDUSA in section 7.3. Hence this agreement suggests that the line drawn across the experimental points in Fig.6.2.2.(b) showing a linear relationship between red peak shift and blue peak shift is a realistic hypothesis. The spectral width between the red shifted peak and the blue shifted peak was found to have no correlation with either the main laser pulse or pre-pulse energies. The latter was only just detectable however if its energy exceeded 10^{-5} that of the main pulse. A remaining feature of all spectra was the apparent structure in the spatial dimension; the spectrum being composed of several 'lines' of emission, with similar, but not identical spectral breadths, and differing intensities. To examine this phenomenon a little more closely, two further experiments were performed. Firstly, a microballoon target was

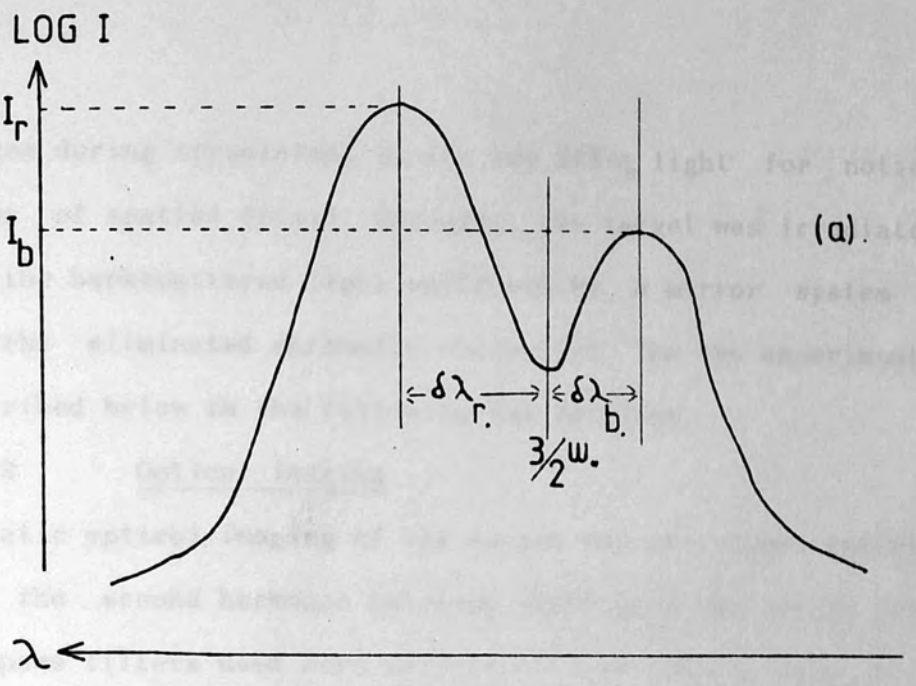

general form of observed $3/2\omega_o$ spectra.
microballoon targets - backscatter

Fig. 6.2.2

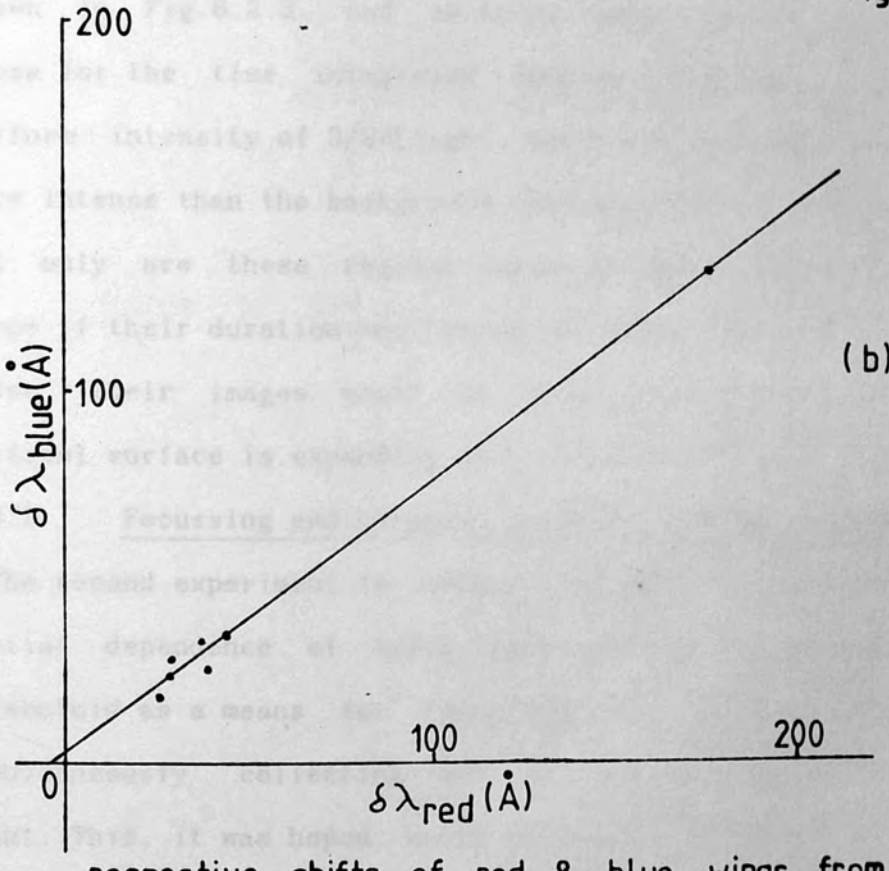

respective shifts of red & blue wings from
$3/2\,\omega_o$ spectra from similar shots

imaged during irradiation in its own $3/2\omega_o$ light for noticeable signs of spatial detail. Secondly, the target was irradiated by, and the backscattered light collected by, a mirror system which thereby eliminated chromatic aberration. The two experiments are described below in the following two sections.

6.2.2 Optical imaging.

Static optical imaging of the target was performed exactly as for the second harmonic emission (Section 4.3); except that the bandpass filters used here were centred on 7093 Å with a 100 Å bandwidth. The experimental arrangement is shown in Fig.4.4.1, and an example of a photograph obtained of the $3/2\omega_o$ emission is shown in Fig.6.2.3, and obtained under similar conditions to those for the time integrated spectra. Instead of a fairly uniform intensity of $3/2\omega_o$ light, there are regions which are far more intense than the background intensity. It is apparent that not only are these regions small in space, but also in time, since if their duration was comparable with that of the laser pulse, their images would be 'smeared out', since the quarter critical surface is expanding at a velocity $>10^5$ m/s.

6.2.3 Focussing and harmonic collection using a paraboloid.

The second experiment to obtain further information on the spatial dependence of $3/2\omega_o$ light involved the use of an f/3.5 paraboloid as a means for focussing the incident light, and simultaneously collecting and collimating the backscattered light. This, it was hoped, would eliminate chromatic aberration providing that achromatic relay lenses, or spherical mirrors were

Fig. 6.2.3.

East beam

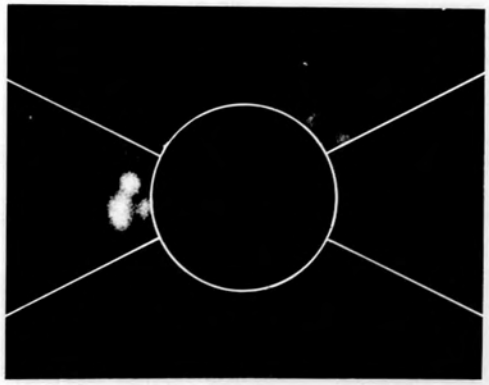

West

example of side-on observation of $\frac{3}{2}\omega_o$ light.

100 Å filter bandwidth
hor. polarised emission
$E_l \sim 8$ J per beam

used to subsequently image the target onto the spectrograph. However, the reflection coefficient of the paraboloid was only 70% in the visible region of the spectrum, and this fact coupled with the much larger focal spot size obtained (~100μm) and the lower collection efficiency (f/3.5 as opposed to f/1), reduced the available irradiance and required that the incident intensity was as high as possible to enable a useful $3/2\omega_o$ exposure to be obtained. The experimental arrangement and a typical $3/2\omega_o$ spectrum are shown in fig.6.2.4. Superimposed on the $3/2\omega_o$ spectrum is another defocussed spectrum of far lesser width (30Å). Since the spectrograph was used in second order this was assumed to be a fourth order spectrum of the third harmonic, and it was removed with a Wratten 61 filter which had a high optical density for wavelengths below ~6000Å. This harmonic has been seen by some other authors and was not studied further. The $3/2\omega_o$ spectrum observed was continuous with a bandwidth of ~60Å. The red and blue wings observed by using the f/1 lenses were far less apparent when using the paraboloid, although the spectrum was very approximately symmetrical about the true $3/2\omega_o$ harmonic position. However, the spectrum does appear to be composed of horizontal 'lines': i.e. discrete spatial regions which radiate a complete spectrum, as the bandwidth of each is very similar, although the intensity of each 'line' was the same.

6.3 Directional dependence of the $3/2\omega_o$ spectrum.

From the spectral results, the $3/2\omega_o$ spectrum as predicted in Chapter 5 for the four recombination mechanisms was observed,

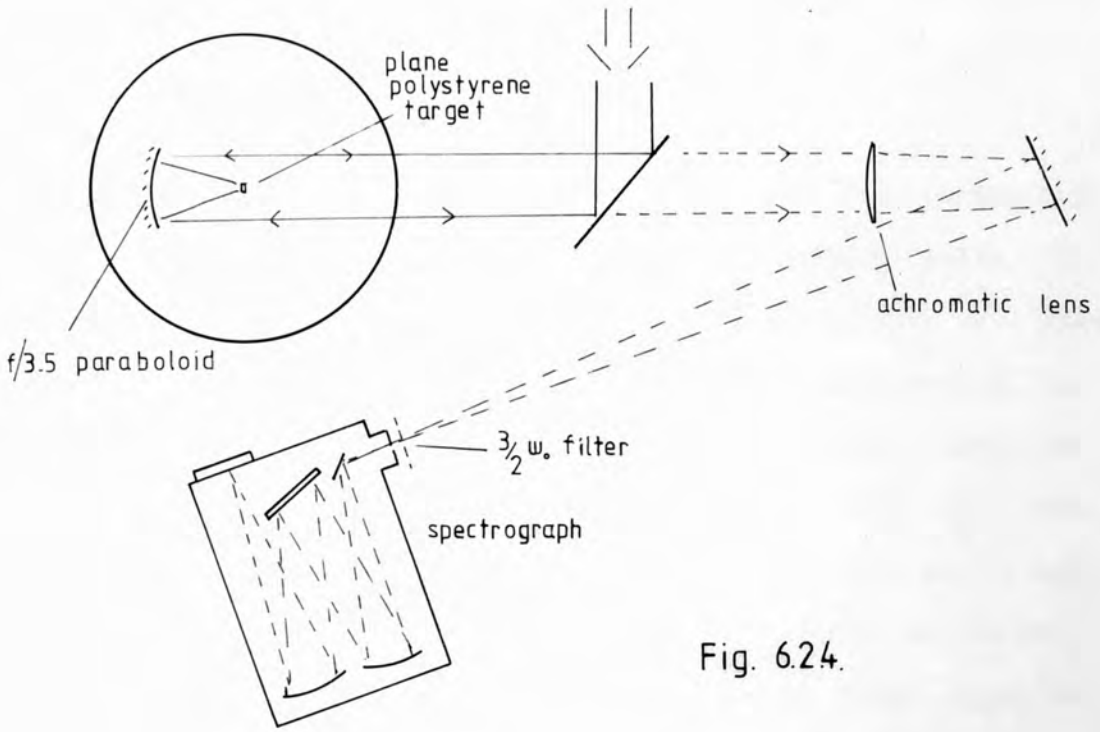

Fig. 6.24.

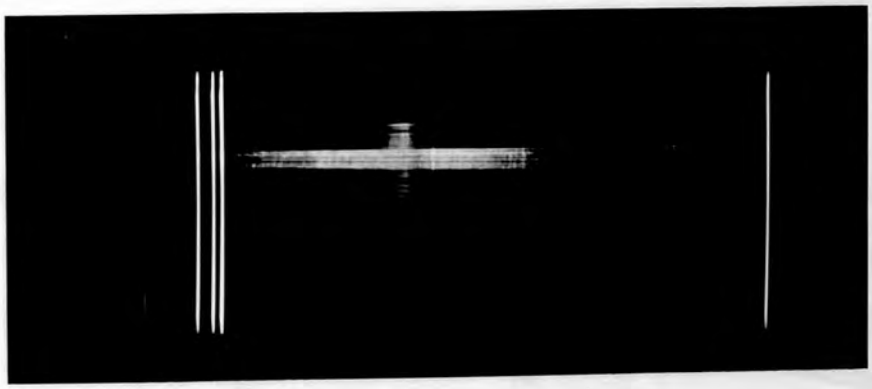

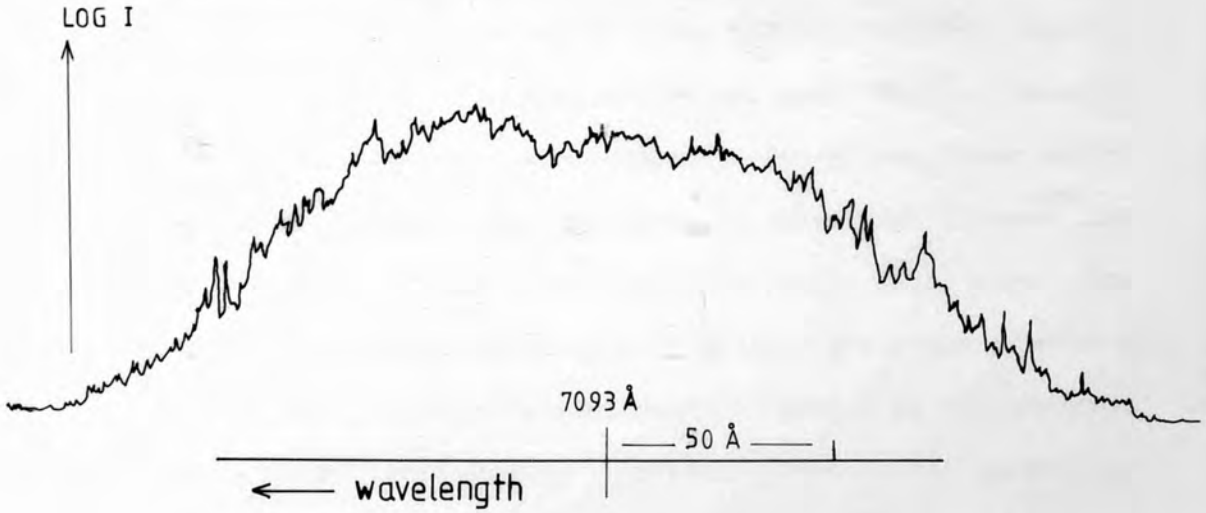

$\frac{3}{2}\omega_0$ spectrum obtained by use of a paraboloid for incident & backscattered light.

although the smaller receiving solid angle of the paraboloid meant the lack of observation of two distinct peaks. An experiment was needed to clarify the generation schemes of $3/2\omega_o$ emission, for which the theory was presented in Section 5.3. One way to do this was to simultaneously observe more than one emission direction, since the spectral shifts from $3/2\omega_o$ are dependent upon the angle (Θ) between the incident wave vector and the scattered $3/2\,\omega_o$ wave, for different mechanisms. It was most advantageous to observe the $3/2\omega_o$ light from two opposing directions, but for massive targets, the forward scattered direction , $0^\circ<\Theta<90^\circ$, is inaccessible since the plasma is grossly overdense for the majority of the laser pulse. However, it will be seen that the use of a thin foil would overcome this, since the plasma would become underdense during the laser pulse, transmitting forward scattered $3/2\,\omega_o$ light. This is because the peak electron density needed to be below $9/4\ n_{cr}$ with respect to the incident laser light, and above $1/4\ n_{cr}$ for generation in the first place. Computer simulation using MEDUSA (Section 7.3), for a 0.4μm polystyrene foil target showed the peak electron density to be within these limits for the majority of the laser pulse, and hence an experiment was planned to use the forward and backward scattered light simultaneously from a foil target. Due to the lower generation efficiency of $3/2\omega_o$ light compared with $2\omega_o$ light, and the loss of a substantial fraction of the incident laser energy upon 'burnthrough', incident power levels needed to be as high as possible, and to optimise collection of the forward

scattered light, an ICOS double element f/1 lens was used for this direction. The experimental arrangement adopted for this experiment, involving East beam irradiation, appears in Fig. 6.3.1. A dichroic mirror behind the target chamber reflected the 'burnthrough' energy to a Joulemeter and avoided any optical damage to subsequent optical components. A second dichroic mirror selectively reflected the $3/2\omega_o$ light, and transmitted remaining unwanted second harmonic and residual fundamental light. With laser energies approaching 30 Joules, several spectra of $3/2\omega_o$ emission in both forward and backward directions were recorded. The thickness of the polystyrene foil target was varied between 0.08 and 2.0μm, no emission being detectable in the forward direction for thicknesses greater than 0.9μm. The spectrograph slit width gave a limit to the spectral resolution of ~2Å, the spectrograph itself again being used in second order to obtain a useful dispersion. A typical result showing both forward and backward directions is shown in Fig. 6.3.2, the backward one uppermost. The incident intensity was $\sim 10^{16}$ W.cm^{-2}, and the particular foil was 0.4μm thick. Chromatic aberration was again apparent in the backward direction, but the superior doublet lens was available for use in the forward direction. Shot to shot differences were noticeable but the general feature of the ratio of intensities were very similar. Unlike the $3/2\,\omega_o$ spectra from microballoon targets, backscattered spectra from thin foils had a far more intense red -shifted wings than blue-shifted wings, and in the example shown, the red wing is barely visible. In

Fig 6.3.1

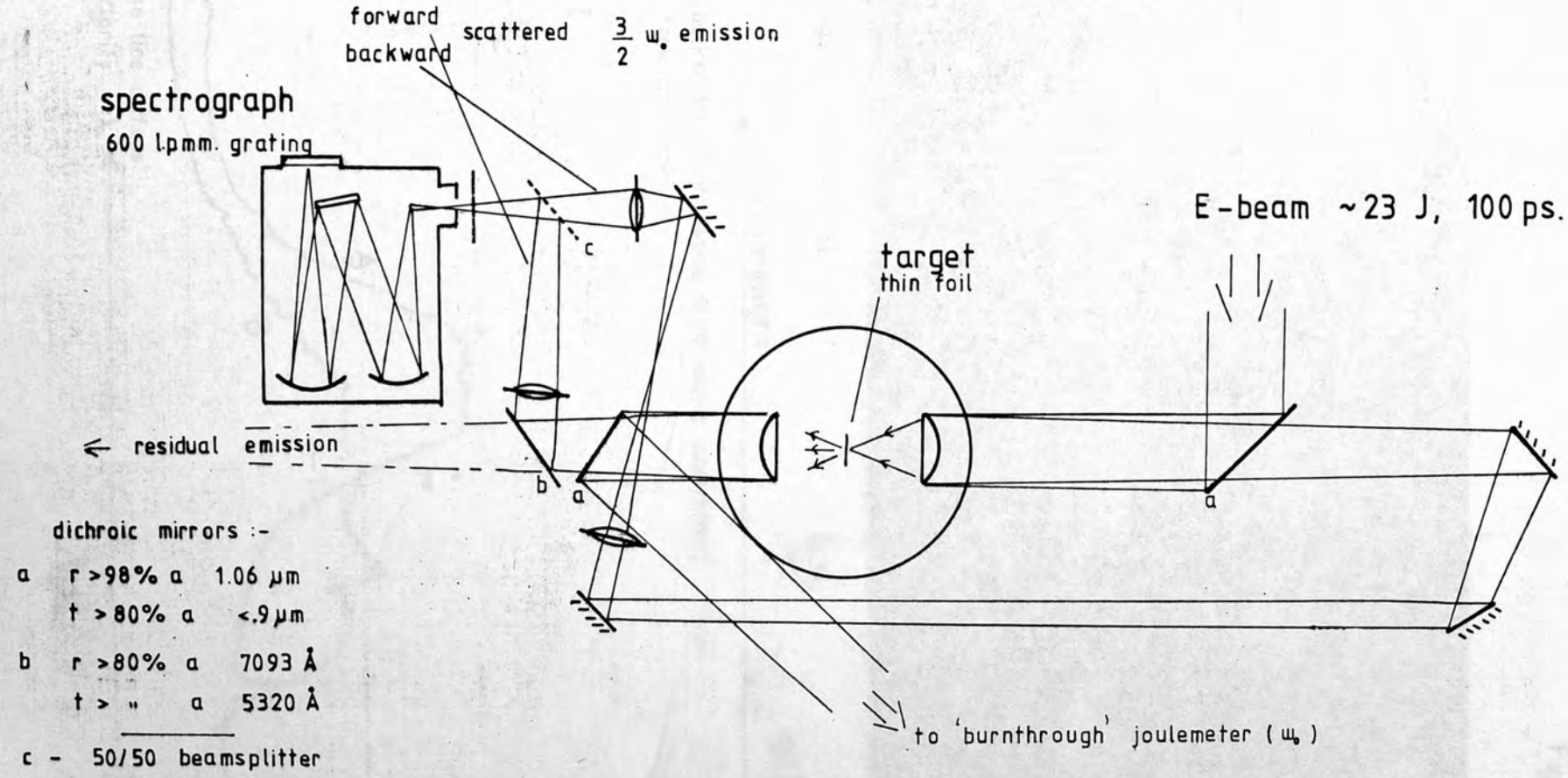

experimental arrangement to observe directional dependence of $\frac{3}{2}\omega_0$ emission.

typical forward & backscattered $3/2\,\omega_0$ spectra from a thin foil target. $E_i \sim 23J$

Fig. 6.32

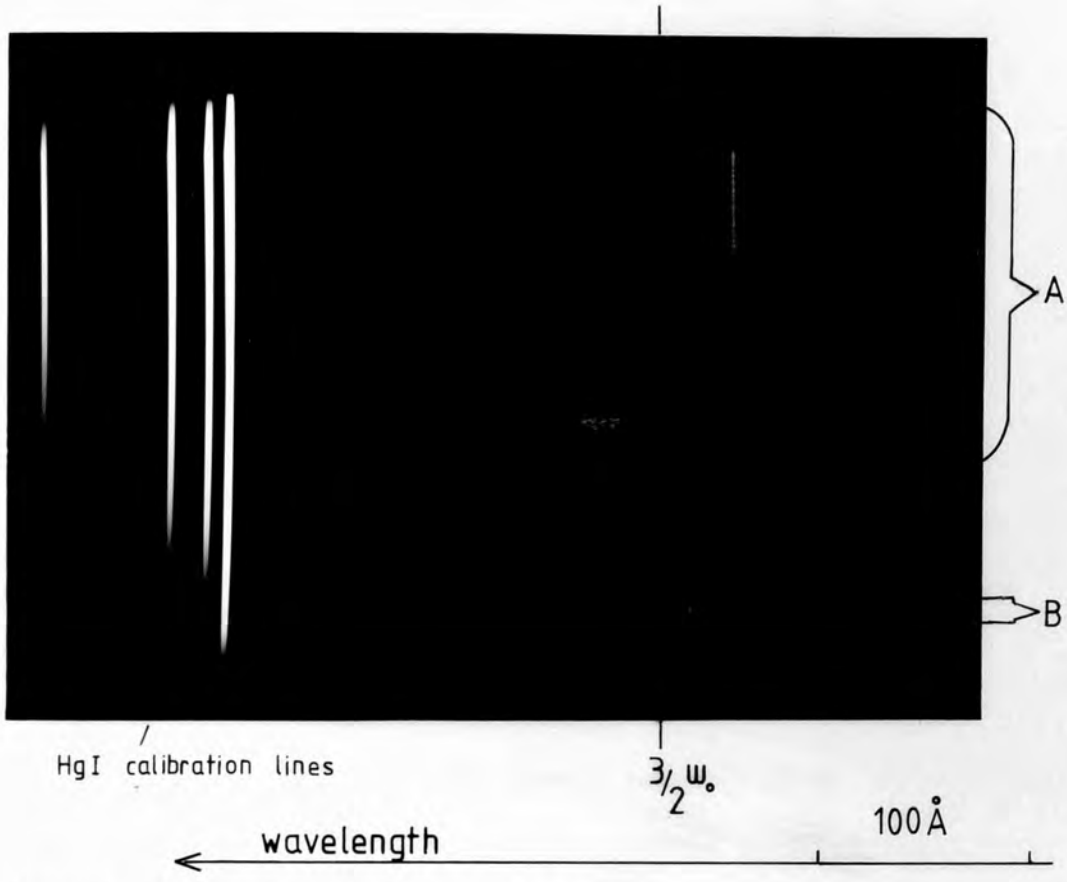

A - backscatter (high degree of chromatic aberration)
B - forward scatter

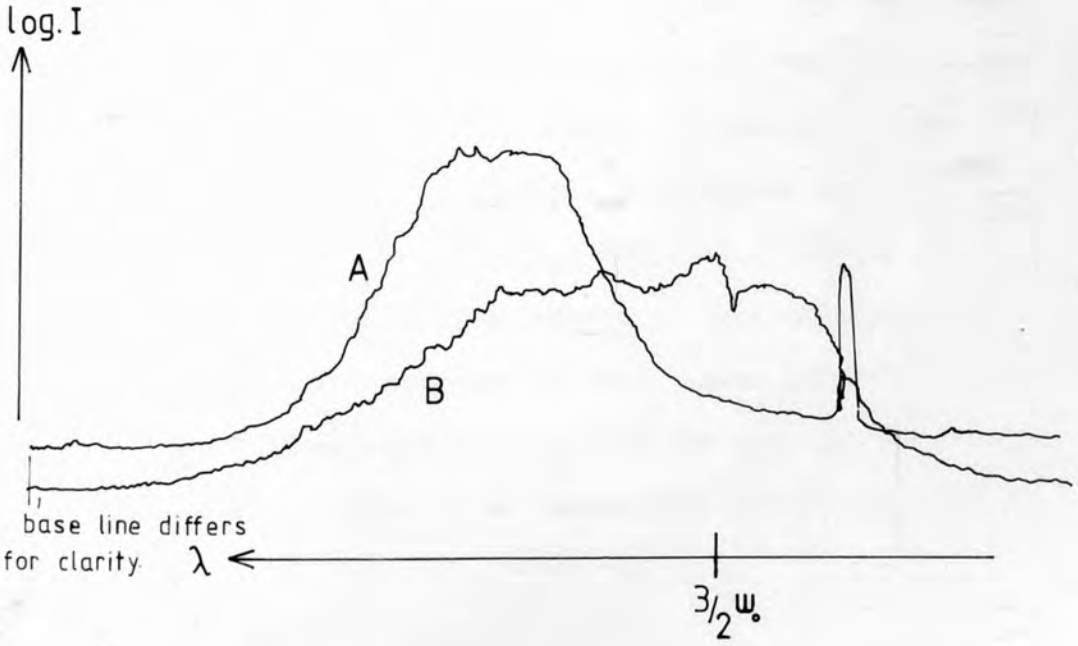

contrast, in the forward direction, an almost continuous spectrum is apparent, the microdensitometer trace indicating a marginally more intense blue-shifted wing. This pattern was maintained for all values of foil thickness, although as the thickness was increased up to 1.0μm, the overall forward scattered intensity diminished, to below the fog level of the film. The backscattered spectrum is certainly different to that obtained from massive targets, and the forward direction is different again. As the blue wing here is more intense than the red wing, a definite spectral dependence upon direction of emission is observed, consistent with results derived from linear theory. This data is discussed with other information in Section 6.5.

6.4 Time resolved $3/2\,\omega_o$ spectral studies

To further characterise the generation of this harmonic, experimental evidence was sought on the time dependence of the $3/2\,\omega_o$ spectrum, as previously achieved with the second harmonic spectrum. The prime interest was in the relative development in time of the red and blue satellites; whether these satellites were synchronous; and whether the total bandwidth (peak - peak) was any function of time, and hence laser intensity. Since the conversion efficiency from fundamental to $3/2\omega_o$ was $\sim 10^{-6}$, far less light was available than for $2\omega_o$ and the streak camera photocathode sensitivity is also reduced at this wavelength.

A similar experimental approach to that taken previously for the time resolved work was adopted, and the experimental layout appears in Fig.6.4.1. However, an Imacon 675 streak camera was

Fig. 6.4.1

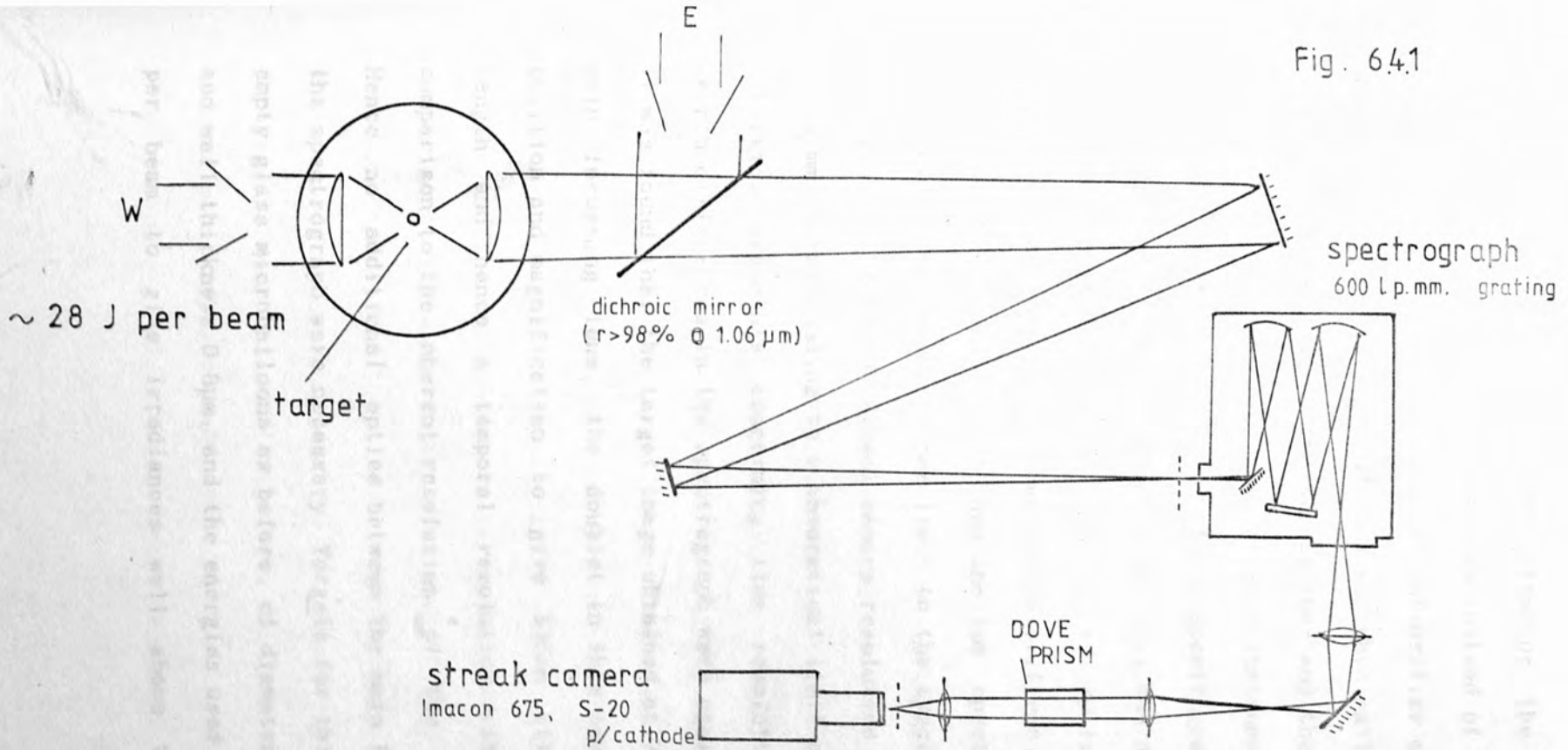

experimental arrangement for time resolving $\frac{3}{2}\omega_0$ spectra.

now available, and offered lower jitter by the use of trigger circuitry employing ceramic valves instead of the KN-22 krytron units of the EPL camera. The image intensifier of the Imacon was of channel-plate design and this was physically in contact with both the phosphor end of the streak tube and the recording film. The horizontal time dispersion of this instrument meant that the horizontal spectral dispersion of the spectrograph needed to be rotated through 90°, and as shown, this was done by means of a Dove prism inclined at 45° in the relay optics. The spectral range as seen on the streak camera slit was made just greater than 300Å, centred on 7093Å, and the 1mm spectrograph entrance slit width meant an upper limit to the spectral resolution of 20Å, compared with the streak camera resolution limit of 28 line pairs/mm, corresponding to a theoretical limit of 1.5Å.

Previous arguments concerning time resolution due to path length differences in the spectrograph were again considered, and it was found that the target image obtained at 7000Å due to the main focussing lens, the doublet in this case, was ideal for position and magnification to give 5.37mm illuminated grating length and hence a temporal resolution ~15ps. This is in comparison to the inherent resolution of the camera of ~7ps. Hence no additional optics between the main focussing lens and the spectrograph were necessary. Targets for this experiment were empty glass microballoons as before, of diameters nominally 80μm, and wall thickness 0.8μm, and the energies used were >23 Joules per beam to give irradiances well above threshold of the

two-plasmon decay. The spectral calibration 'spots' were also put on as before, except that the relative wavelengths were 7043, 7093, and 7193Å. To achieve the calibration it was necessary to trigger the channel plate intensifier from an external source, and this was done using a +20V pulse from a Farnell pulse generator.

6.5 Experimental results of time resolved work.

Several time-resolved spectra were recorded from microballoon targets on Kodak 2485 high speed film and developed in D-19 for 5 minutes at 30°C. Typical $3/2\,\omega_0$ time resolved spectra appear in Figs.6.5.1.a,b and b, the latter spectrum being recorded with the spectrograph in first order to increase the time resolution. This was for comparison and also to reduce the edge effects of the streak tube. Four features of all the time resolved spectra became apparent, the most notable of these being the fact that the total spectrum is pulsed in time, on timescales less than the resolution limit of the recording system. Secondly, emission of the blue satellite is entirely synchronous with emission of the red satellite, no one satellite therefore appearing without the other. As with the time integrated spectra, the departure of the peak of the blue satellite from 7093Å appears to be a linear function of the departure of the red satellite from 7093Å, which is true for each burst of emission. The total bandwidth, red peak to blue peak, appears to decrease as time progresses, although this is not completely consistent from shot to shot, but on no

Fig. 6.5.1. a

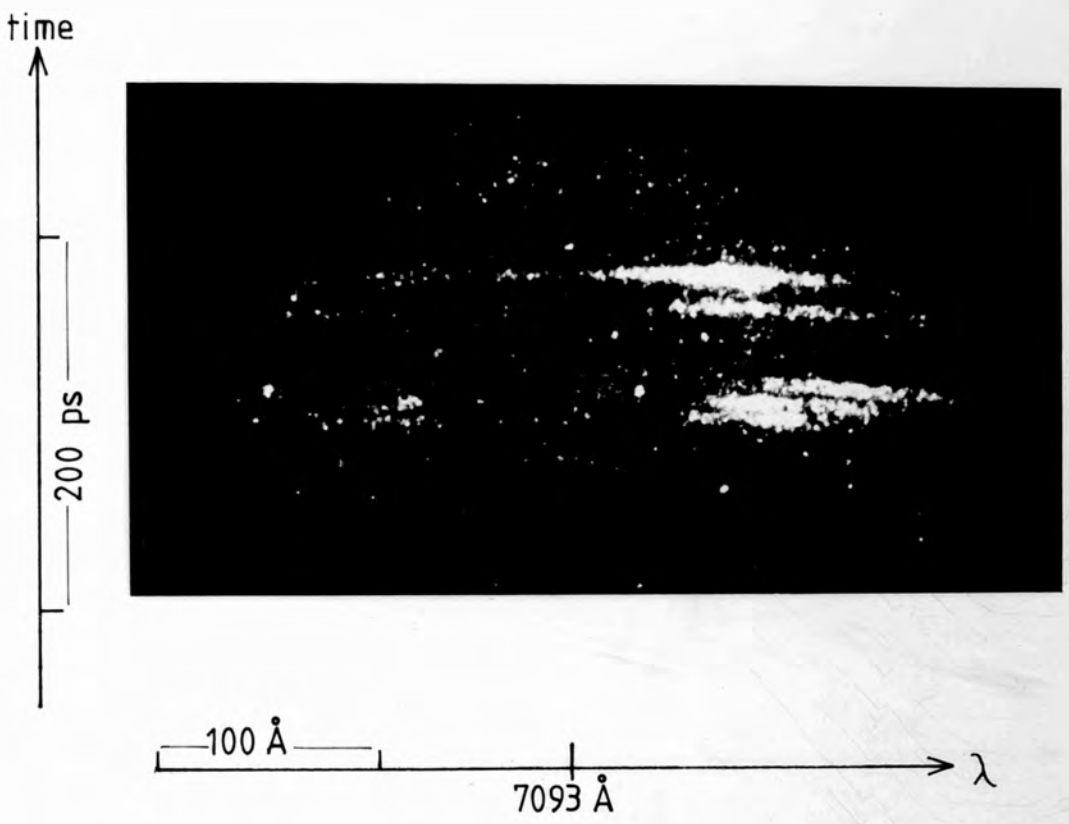

time resolved $\frac{3}{2}\omega_0$ spectrum μballoon target, $E_i \sim 28$ J per beam

Fig. 6.5.1 b

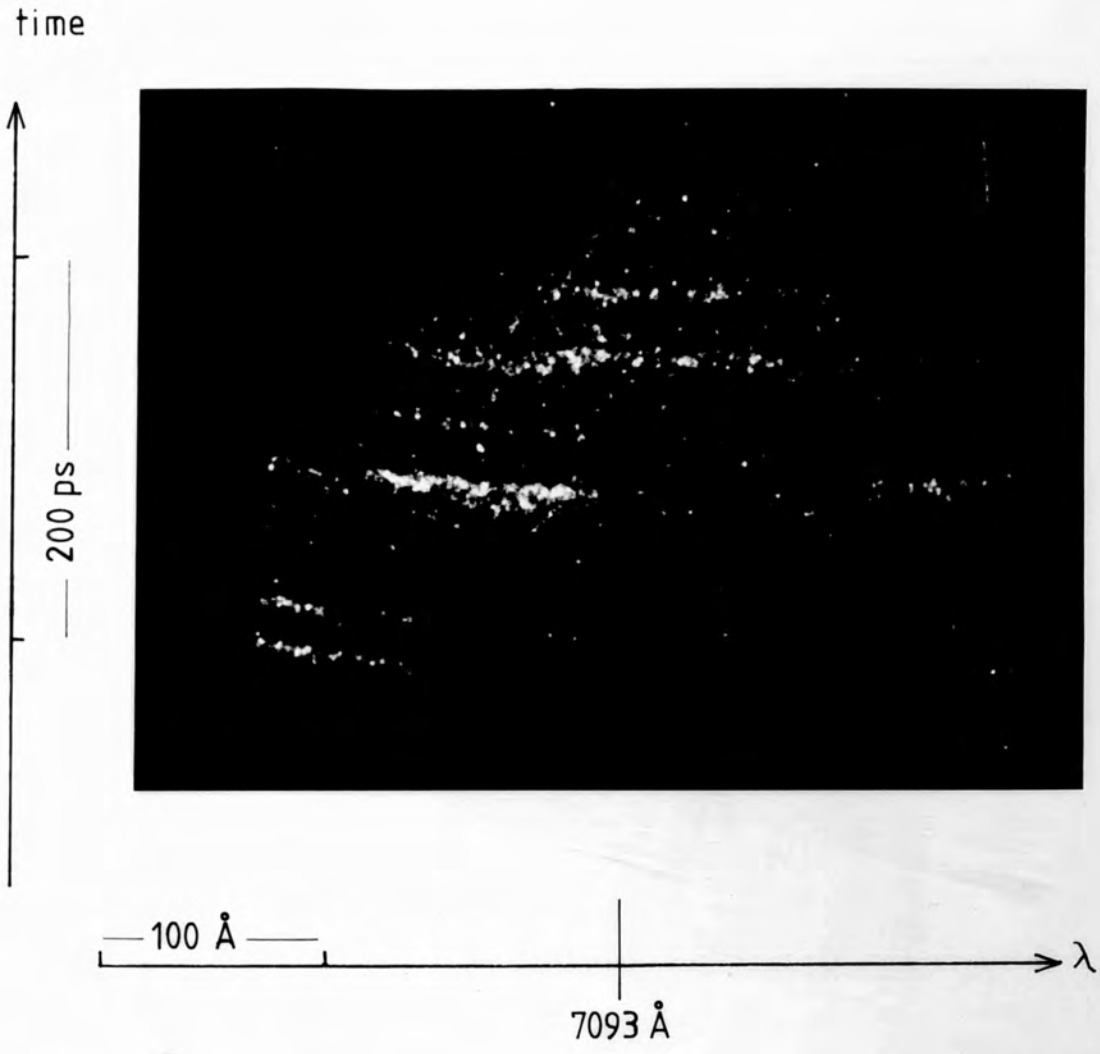

time resolved $\frac{3}{2}\omega_o$ spectrum — μballoon target, E_i~28 J per beam

Fig. 6.5.1. c

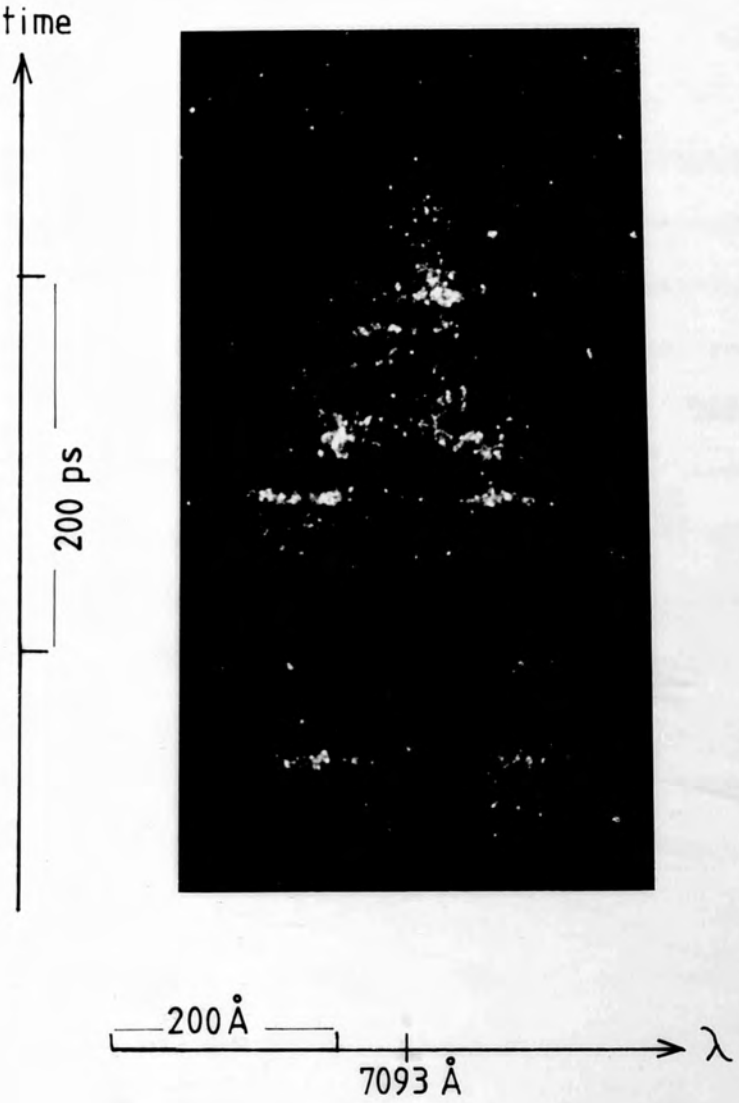

time resolved $\frac{3}{2}\omega_0$ spectrum μ-balloon target $E_i \sim 28$ J.

spectrograph in first order

occasion does the bandwidth increase as time progresses. The shot recorded in first order was to achieve greater temporal resolution at the expense of spectral resolution, and here the $3/2\,\omega_o$ emission 'bursts' are also limited by the instrumental resolution.

6.6 Discussion.

The experiments performed here have given fresh information on the nature of three-halves harmonic emission from laser-produced plasmas. With this harmonic having a high threshold has meant the use of laser powers in excess of 100 GW per beam, and from consideration of the recording film sensitivity at 7093Å, a fundamental/three-halves conversion efficiency of $\sim 10^{-7}$ was noted at these powers. Due to the difference in threshold irradiance, the two plasmon decay was by far the more dominant mechanism in producing plasmons at $\omega_0/2$ in mean frequency, and the preceding analysis in Chapter 5, using these plasmons may be used to interprete experimental data.

From the time integrated $3/2\,\omega_o$ spectra, taken from microballoon targets irradiated with f/1 lenses, two well defined peaks are apparent; one blue shifted from the true harmonic position, and the other red shifted. The blue shift was always less than the red shift , and the two peaks had a linear relationship between their respective differences from 7093Å, within the limits of experimental accuracy. When the solid angle of irradiation and collection was decreased, by the use of a paraboloid instead of a lens, the two peaks became indistinct, although the total

spectral width was similar, and both red and blue shifted components were apparent.

Further information was provided by the thin foil experiment where a spectrum similar to that obtained with the paraboloid was seen in the forward direction, whilst only a red component was simultaneously observed in the backscattered direction. By virtue of the fact that both definite red and blue peaks are seen from massive targets, the spectrum obtained by the recombination of an incident photon and plasmon is unlikely, since this only generates a red shifted peak. For the recombination of a plasmon and either a specularly reflected or Brillouin scattered photon, both red and blue components are generated, but the spectrum predicted from the theory is asymmetric about 7093Å, with a greater shift to the blue. Experimentally however, several factors need to be considered which can affect the observed spectrum. If Brillouin scattering provides the recombining photon, then the whole spectrum will be red shifted by an amount equal to ~8.0Å, for Z~9.6, and T_e~2keV. This must be balanced against the Doppler shift due to the quarter critical expansion of ~4.0Å. A more important factor however, is that the peak of the blue wimg, which travels to the 9/4 n_{cr} surface and returns, is, if specularly reflected, just outside the f/1 lens solid angle, since as shown in Fig.5.3.1.a, the 55° forward scattering angle returns just outside the f/1 lens angle, (2. arctan 0.5). Also the recombining plasmons with the highest values of the $\underline{k}$ vector (blue shifted) will experience greater Landau damping, and

this in turn will reduce the blue peak shift, as in Fig.5.3.1.b. Hence these two schemes offer good agreement with the experimental data, and if an assumption is made that the blue peak occuring at 55° to the incident $\underline{k}$ vector is collected by the lens, then a determination of the minimum absorption encountered by the $3/2\,\omega_o$ wave in travelling to the $9/4\,n_{cr}$ surface and back may be made. From a figure for this absorption, a value for spatially averaged density scalelength may be estimated, since from equation 2.2.14. for a wave travelling from 1/9th critical and back; as for a $\frac{3}{2}\omega_o$ wave, from $\frac{n_{cr}}{4}$ to $\frac{9}{4}n_{cr}$.

$$\frac{I_{blue}}{I_{red}} = 1 - \exp\left(-2.132\,\frac{L_n \nu_{cr}}{c}\right)$$

Experimentally determined values of the ratio of blue wing intensity to red wing intensity are, after film calibration, between 0.32 and 0.60, so that inserting a realistic value of the collision frequency of $5.10^{12}\ s^{-1}$, a range of scalelengths between 10μm and 25μm is predicted, extremely well with those obtained from interferometric experiments and from computer codes, as in Chapter 7, these giving a value ~13.5μm.

With the spectra obtained by use of the paraboloid, two functions were served; the chromatic aberration was eliminated and the solid angle of irradiation/collection reduced. With respect to the latter, this meant that the peaks of both the red and blue components, as previously seen, now fall well outside the solid angle of the collection optics, and accounts for the lack of two definite peaks, as observed with f/1 optics, since

the half angle subtended by the paraboloid was only 8.1° as opposed to 26.6° previously. As the red peak for either the specularly reflected or Brillouin scattered photon and plasmon recombination scheme is emitted well within the solid angle of the lens, an estimate may be made of the electron temperature at quarter critical from the spectral shift (red peak - 7093Å). As the Brillouin and Doppler shifts are small and opposing, they are ignored for this estimate. Typically, $\delta\lambda$ from the red peak to $3/2\omega_o$ is 62Å, and as $\delta\lambda = +\ 19.1\ T_e$ Å, where T_e is in keV, this electron temperature is approximately 3.2 keV. This value is high with respect to data gathered from the thermal electron temperature determined by the X-ray absorber foil method, and also that determined by computer simulation. These other values are ~0.8 keV, but if the temperature determined from the $3/2\omega_o$ spectra may not be unrealistic if the suprathermal electron temperature distribution is included, of typically 10 keV.

Returning to data on the $3/2\omega_o$ spectrum as provided by the thin foil experiment, the lack of a discernible blue wing in the backscattered direction gives evidence for forward scattering of any blue wing, and its appearance in the spectra from massive targets by virtue of reflection at 9/4 n_{cr}. However, the blue component in the forward scattered direction is marginally more intense than the red. So from the experiments on massive targets, evidence points to the mechanism of a specularly reflected photon and plasmon recombination as the dominant scheme, when observed in backscatter. This scheme is in preference to SBS photon and

plasmon recombination since the short laser pulse used (100ps) on every shot was not of sufficient duration to enable long scalelengths to be produced, and as the gain for SBS is proportional to the scalelength, then the experimental conditions were not conducive to SBS. For the thin foil experiments, the foil became underdense rapidly, so that not only does the 9/4 n_{cr} surface cease to exist, but also the n_{cr} surface, and if the latter is non-existent, then specularly reflected or Brillouin scattered photons cannot exist. This fact, coupled with the criterion that two plasmon decay can take place at densities less than a quarter critical, indicates that either incident photon/plasmon or 3 plasmon recombination is responsible for the observed $3/2\omega_o$ light. Since both of these schemes have similar angular dependence of the spectrum, it is difficult to determine which mechanism is dominant. Both can explain the observed $3/2\omega_o$ spectra from the foil targets, since the f/1 lens in the forward direction can collect blue and red components, whilst the backscattered lens can collect only red. From considerations of ease of matching conditions, the 3 plasmon recombination is considered the more probable.

The side-on photographs of the localised nature of $3/2\omega_o$ emission, together with the paraboloid spectra, show the emission to occur in discrete 'bursts', each localised in space but not in wavelength. As shown earlier, since these bursts are not 'smeared-out' in space, they must be occuring on timescales much less than the laser pulse duration, and this deduction was later

confirmed with the time resolved work. Taking this information, together with the spectral nature of the time resolved spectra shows that a complete spectrum of plasmons, approximately centred on $\omega_0/2$ is produced by the two plasmon decay, in small localised bursts within the plasma corona; $3/2\,\omega_0$ light is similar to that of the $2\omega_0$ light, and again the assumption is made that the parametrically excited plasma waves with the maximum growth rate grow until detuning limits any further growth. As recorded earlier, the approximate maximum growth rate for the two plasmon decay is $v_0\omega_{pe}/\sqrt{2}\,c$, so that within the time resolution of the spectrograph/streak camera system, an increase in the plasma wave amplitude of e^{256}, or effectively infinite, is possible. These waves then Landau damp, and in doing so produce fast electrons. These electrons in turn give rise to Landau damping at larger phase velocities (smaller $k\lambda_D$) which will effectively increase the threshold, and account for the delay between pulses. This is the time taken for the laser pulse leading edge to increase in power beyond the new threshold. Spectrally, Lee and Kaw[4] have shown that for two plasmon decay, a limit exists for the maximum detuning, which in terms of the difference in frequency between one plasmon and the laser frequency is

$$\frac{\delta\omega}{\omega_{pe}} = \frac{v_0}{c}\sqrt{\sin 2\theta}$$

where θ is the angle between the incident laser wave vector and the plasma wave vector. This has a maximum when $\theta = 45^\circ$, and

$$\frac{\delta\omega}{\omega} = \frac{v_o}{c}\sqrt{2}$$

so that at 10^{16} W.cm^{-2} , a maximum of 140Å red peak to blue peak is predicted, which agrees with the previous theory of plasmon and specularly reflected or Brillouin scattered photon recombination, and with the time integrated spectra frm massive targets. However, if the angle of propagation of the plasmons should change as a function of time, then the separation of these peaks will decrease also.

The experimental observation that these two peaks do decrease in separation with advancing time gives evidence for a mechanism which forces the plasmons to propagate at angles different to the optimum. This may be explained by the appearance of perturbation in the density profile, so that due to a density depression (caviton) near n_{cr} , the plasmons are forced to propagate nearer to 90° than 45° , due to wave matching criteria. Evidence for caviton formation has been reported experimentally upon identical targets, at similar laser intensities. From the time resolved $3/2\,\omega_o$ spectrum of Fig.6.5.1.a, a decrease of peak to peak spread from 174Å to 112Å in ~31ps indicates a change between the plasmon/incident photon wave vectors of ~33°. The timescale on which this change occurs is in agreement with the density profile measurements (ref. 7) at different times during the laser pulse which indicate caviton formation to be achieved within 50ps.

Chapter 6 - References

1. B Grek, H Pepin, T W Johnston, J N LeBoeuf & H A Baldis, Nucl. Fusion, 17, 6, 1977

2. E A McLean, J A Stamper, B H Ripin, H R Griem, J M McMahon & S E Bodner, Appl. Phys. Letts, 31, 12, 1977

3. N H Burnett, H A Baldis, M C Richardson & G D Enright, Appl. Phys. Letts, 31, 3, 1977

4. Y C Lee & P K Kaw, Phys. Rev. Letts, 32, 4, 1974

5. R Fedosejevs, I V Tomov, N H Burnett, G D Enright & M C Richardson, Phys. Rev. Letts, 39, 15, 1977

6. D T Attwood et al, Phys. Rev. Letts, 40, p184, 1978

7. A Raven & O Willi, Phys. Rev. Letts, 43, 4, 1979

— Chapter 7 —

Numerical studies of the plasma corona.

7.1 The hydrodynamic motion of the plasma has been modelled numerically by use of a published computer code, in order to obtain expansion velocities of the critical and quarter critical surfaces. Density profiles and their variation during the laser pulse have also been studied, using the same code. The paths of optical rays in these regions have then been determined by the development of a ray-trace code, 'TRACE'.

7.1.2 The application of a computer code.

The largest numerical model used in these studies was the one-dimensional, two fluid Lagrangian computer code MEDUSA, described in detail in refs. 1-3. This has been substantially modified since its original form to take account of factors such as fast (suprathermal) electron transport and also ponderomotive force[4]; the latter incorporated in a switchable subroutine. The code was used almost entirely to simulate the evolution of the coronal density profile, and hence various points on the profile, the variable parameters of the code being summarised under three categories: laser input pulse, target configuration, and the constraints on plasma transport phenomena. Being a one-dimensional code, MEDUSA could be used with either planar, cylindrical, or spherical geometric systems. However, it has been shown by Morse[5] that when using a one-dimensional code, the differences in plasma parameters generated using planar and spherical geometry is negligible at distances from the centre of symmetry greater than twice the focal spot radius. Hence

spherical geometry was used in all runs, including those for planar targets. With regard to energy absorption, MEDUSA uses inverse bremsstrahlung absorption up to the critical surface, at which resonant and anomalous absorption effects are simulated by depositing a prescribed fraction of the remaining energy there. Another variable enables a fraction of the absorbed energy to be released in a suprathermal electron distribution with a mean temperature n times that of the thermal distribution. In all cases here the suprathermal temperature was 9 times the thermal temperature. Electron thermal conduction as the energy transport mechanism obeyed Fourier's law until the net flux across an interface equalled a preset fraction of the flux limit on the free-streaming limit. i.e. until

$Q = -K_e \nabla T_e$ (K_e = thermal conductivity, e.g. Spitzer.)

had a limit of $Q_{max} = \frac{a\, n_e\, v_{th}\, k_B\, T_e}{4}$

where a was the flux limiting parameter.

Also in MEDUSA was a means for determining the rate of energy release if fusionable target materials were used. Neutrons generated fron thermonuclear reactions were taken to be a mass and momentum loss from the system, as well as was normal bremsstrahlung. Further details on the original code are contained in references 1-3.

7.2 Critical surface motion.

Motivation for studying the motion of the critical surface was

provided by the need to ascertain the effect of this motion on the second harmonic spectrum. Also the results were relevant to directly reflected and scattered laser light, at ω_o. With regard to critical surface motion, several models have been proposed to evaluate motion of the plasma 'fluid', and to obtain expressions for the electron/ion temperature and density away from the target.[8-13] However, most of these models are steady state, whereas in the experiments, the laser pulse, being Gaussian with a 100ps FWHM, meant that the rate of change of irradiance was extremely high. At the other extreme, a model to simulate picosecond pulse interaction, such that there is no time for any hydrodynamic expansion to occur,[12,13] or steady state to be established, is also inappropiate. Indeed, at high irradiances, generalisations are few, and simulation of absorption due to anomalous mechanisms extremely difficult. Hence the use of a computer code, but for order of magnitude calculations, a simple hydrodynamic model was sufficient, since the expected Doppler shifts due to critical surface motion were small compared with spectral widths. This could enable a simple overall view of the hydrodynamic blow-off to be obtained, and permit trends of the effect of laser irradiance and transport phenomena on this ablation to be made, and this model follows.

In one dimension, under isothermal conditions with equal electron and ion temperatures, the equations of motion and continuity are:[14]

$$m_i\, n\left(\frac{d}{dt} + v\frac{d}{dz}\right)v = -2\, k_B\, T_e \frac{dn}{dz} \qquad 7.2.1$$

$$\frac{dn}{dt} + \frac{d(nv)}{dz} = 0$$

where m_i = ionic mass.

Here, z is the distance from the surface of ablation, which has essentially zero velocity, and clearly has an initial value corresponding to the target radius, but moves fractionally inwards during the laser pulse. The solution of 7.2.1 and 7.2.2 gives:

$$n_e = n_o \exp \frac{z}{c_s t} \qquad 7.2.3$$

$$v(t) = c_s + \frac{z}{t} \qquad 7.2.4$$

where c_s is the isothermal sound speed and $= \sqrt{\frac{2\, k_B\, T_e}{m_i}}$

The mass flow from the ablation surface , $\frac{dm}{dt} = m_i\, c_s\, n_o$, where n_o is the initial solid particle density, and the kinetic pressure at this surface is equal to $2\, n_o\, k_B\, T_e = p_A$.

The initial mass of the target (per unit area) as a function of time is then

$m(t) = m_o - \frac{dm}{dt}.t$, where m_o is the initial mass of the target, and this may be used to obtain the equation of motion of the ablation region.

$$\left(m_o - \frac{dm}{dt} t \right) \frac{d^2 z}{dt^2} = p_A$$

Evaluation of the integral after the initial condition t=0, gives:

$$\frac{dz}{dt} = v(t) = c_s \ln \frac{m_o}{m(t)}$$

$$v(t) = c_s \ln \left(\frac{1}{1 - \frac{\frac{dm}{dt} t}{m_o}} \right) \qquad 7.2.5$$

This expression shows the ablation velocity to increase with time, assuming a relatively constant ablation rate; and also that the expansion velocity will be greater than the ion sound speed if

$$\frac{dm}{dt} t \; > \; 63\% \text{ of } m_o$$

It is also apparent that from this simple analysis the density scalelength will increase with time, as $L_n = c_s t$ where

$$L_n = \left(\frac{1}{n_e} \frac{dn_e}{dz} \right)^{-1}$$

A 100ps laser pulse of constant irradiance produces a density scalelength of ~20μm for a typical ion sound speed of 2.10^5 m/s. This value is in exceptionally good agreement with that experimentally determined on similar targets at similar

irradiances by several authors[16-18].

MEDUSA was now used to simulate the critical surface motion, after the previous empirical model had estimated the order of expected expansion velocities and scalelengths. To do this, a subroutine was incorporated which on each timestep located the mesh point furthest from the core and sequentially moved inwards by a mesh point at a time until one was located corresponding to a density greater than critical. Linear interpolation between this one and the previous one was used to give a position for the actual critical surface radius. A graphics routine then reproduced this position as a function of time. The radii for four different values of the peak laser irradiance are shown in Fig.7.2.1 for a glass microballoon target; the pulse shape of 100ps FWHM Gaussian corresponding to that used in experiments. Although for spherical geometry the fluxes are quoted in $W.sr^{-1}$, an experimentally determined value of 30μm for the focal spot diameter of the Soro lens gives a conversion factor of $1.41\ 10^{5}$ to irradiance into $W./cm^{2}$. The other variable parameters of thermal flux limit and fraction of absorbed energy converted into fast electrons were set at 3% and 90% respectively; these values corresponding most closely with data from published experiments.[15,19] From the simulations, higher irradiances corresponded with higher mean expansion velocities, and the greater the maximum extent of the critical surface before it becomes underdense, and moves inwards. The time t=0 corresponds to the point on the leading edge of the Gaussian laser pulse where the power is e^{-3} of the

Fig. 7.2.1.

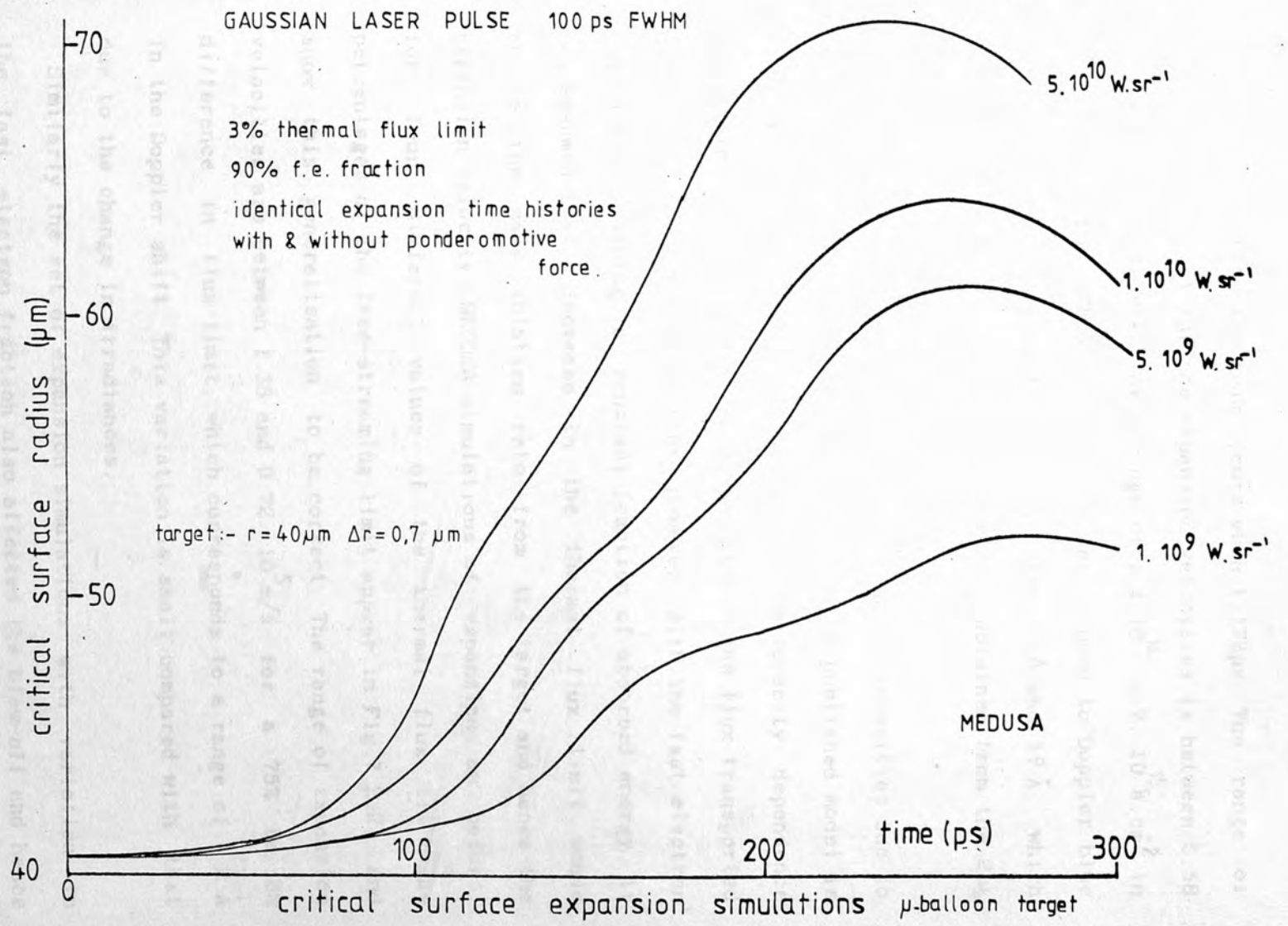
GAUSSIAN LASER PULSE 100 ps FWHM
3% thermal flux limit
90% f.e. fraction
identical expansion time histories
with & without ponderomotive
force.
target :- r = 40 μm Δr = 0,7 μm
5. 10^10 W.sr^-1
1. 10^10 W.sr^-1
5. 10^9 W.sr^-1
1. 10^9 W.sr^-1
MEDUSA
critical surface radius (μm)
70
60
50
40
0
100
200
300
time (ps)
critical surface expansion simulations μ-balloon target

peak power and hence the peak occurs when t=178ps. The range of these mean critical surface expansion velocities is between 5.58 10^4 m/s and 2.23 10^5 m/s, for a range of 1.4 10^{14} to 7. 10^{15} W.cm^{-2} in laser irradiance. These velocities correspond to Doppler blue shifts of the $2\omega_o$ backscattered light between 1.0 and 3.9 Å, which agree well with the expansion velocities obtained from the $2\omega_o$ side -on time integrated photographs.

With regard to the influence on the expansion velocities due to the plasma transport phenomena, again no one published model is sufficient to give a complete picture of the velocity dependence upon thermal flux limit or the proportion of the flux transported by fast (suprathermal) electrons. However, with the fast electron component remaining a constant fraction of absorbed energy, it was assumed that a decrease in the thermal flux limit would reduce the mass ablation rate from the target and hence the expansion velocity. MEDUSA simulations of expansion as before, for four different values of the thermal flux limit as percentages of the free-streaming limit appear in Fig.7.2.2, and show this generalisation to be correct. The range of expansion velocities are between 1.38 and 0.72. 10^5 m/s for a 75% to 3% difference in flux limit, which corresponds to a range of 1.2 Å in the Doppler shift. This variation is small compared with that due to the change in irradiances.

Similarly the set of expansion simulations with variation in the fast electron fraction also affected the blow-off and hence critical surface velocity, but to a limited extent. An increase

Fig. 7.2.2.

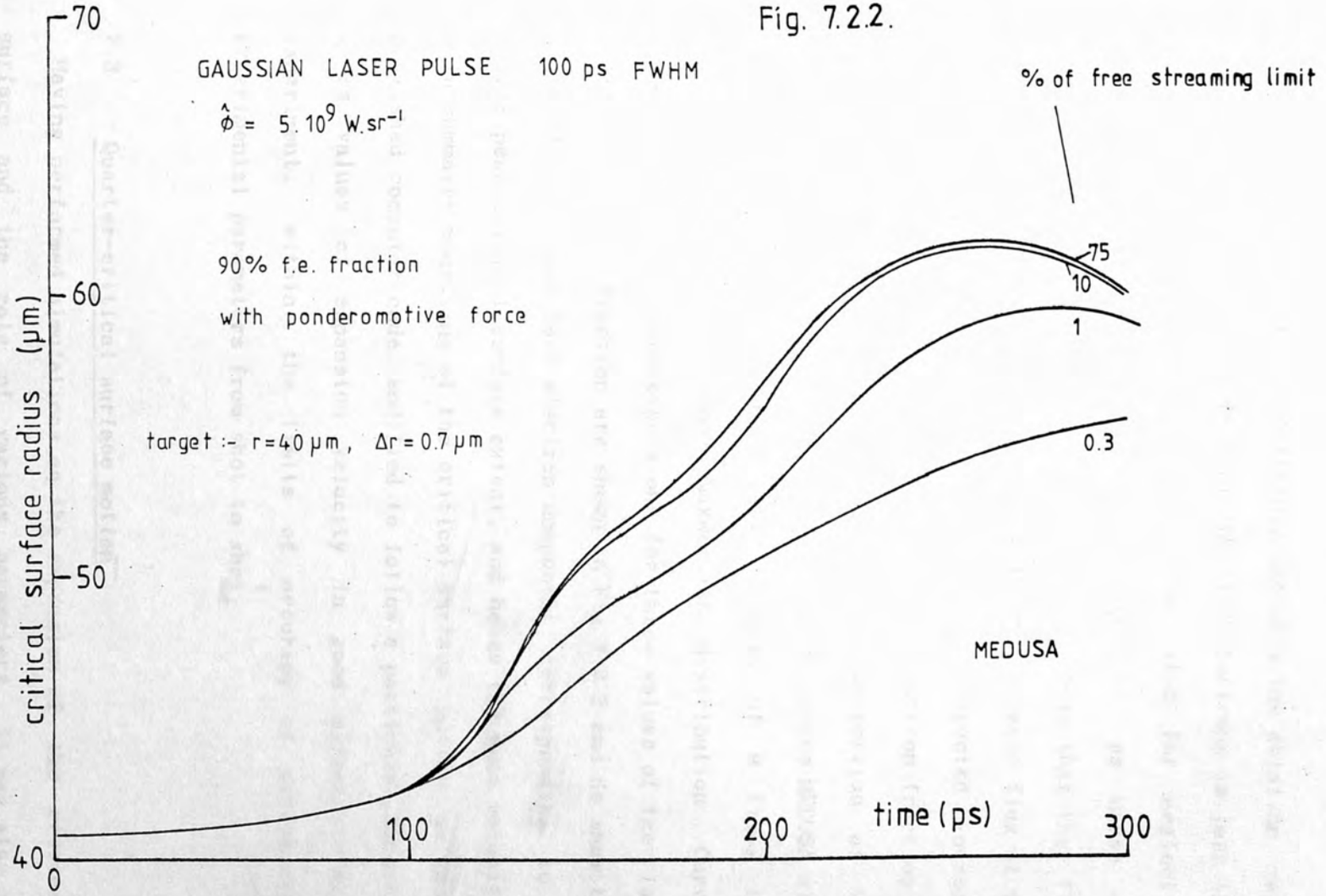

critical surface expansion simulations - μ-balloon target, variable thermal flux limit.

in fast electron flux will certainly increase the ablation rate, but only if the mean free path of the fast electrons is less than the core diameter. This criterion is also valid for neglecting the core preheat due to fast electrons, as Morse and Nielson predict from their model[21], which also shows that the flux in the pellet core must be less than 1% of the laser flux at the critical surface for negligible preheat. So an expected increase in expansion velocity with increase in fast electron fraction is limited by the assumption that only a limited proportion of the energy may be responsible for mass ablation, since MEDUSA also has a suprathermal distribution with a mean of 9 times the temperature of the thermal Maxwellian distribution. Curves showing critical surface expansions for three values of the fast electron energy fraction are shown in Fig.7.2.3 and do show the trend of the larger fast electron component corresponding to a larger peak critical surface extent, and hence the mean velocity.

In summary, modelling of the critical surface motion using a published computer code, modified to follow a particular density, gives values of expansion velocity in good agreement with experiment, within the limits of accuracy of determining experimental parameters from shot to shot.

7.3 Quarter-critical surface motion.

Having performed simulations on the expansion of the critical surface and the role of various parameters, it was also of importance to do likewise with the quarter critical surface,

Fig. 7.2.3.

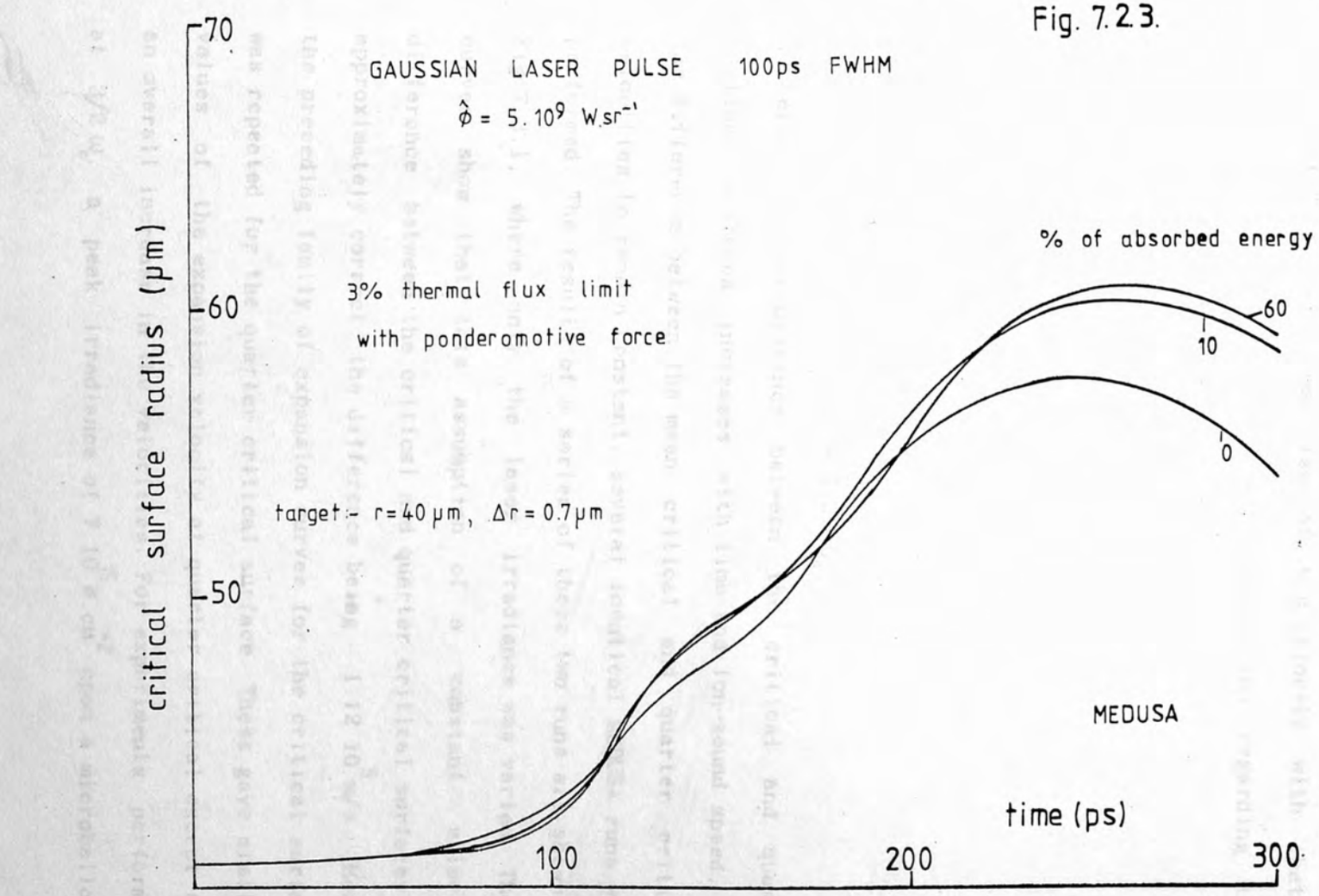

critical surface expansion simulations — μ-balloon target, variable fraction of absorbed energy given to fast electron distribution.

since this affected shifts on the three-halves harmonic emission. Since it is the mean expansion velocity of this density which is of greatest interest, comparison of this velocity with that of the critical surface can yield information regarding their relationship, since from equation 7.2.5:

$$\frac{n_e}{n_o} = \exp - \frac{z}{c_s t}$$

so that for an expanding density profile;

$$\ln\left(\frac{n_{cr}}{n_{\frac{cr}{4}}}\right) = \frac{1}{c_s t}\left(z_{\frac{cr}{4}} - z_{cr}\right)$$

$$z_{\frac{cr}{4}} - z_{cr} = 1.39\ c_s\ t = 1.39\ L_n$$

To verify that the distance between the critical and quarter critical surfaces increases with time and ion-sound speed, and the difference between the mean critical and quarter critical velocities to remain constant, several identical MEDUSA runs were performed. The results of a series of these two runs are shown in Fig.7.3.1, where only the laser irradiance was varied. These curves show that this assumption of a constant velocity difference between the critical and quarter critical surfaces is approximately correct, the difference being $1.12\ 10^5$ m/s. Hence the preceding family of expansion curves for the critical surface was repeated for the quarter critical surface. These gave similar values of the expansion velocity at quarter critical except for an overall increase in the velocities. For experiments performed at $3/2\ \omega_o$, a peak irradiance of 7.10^{15} W.cm^{-2} upon a microballoon

Fig. 7.3.1.

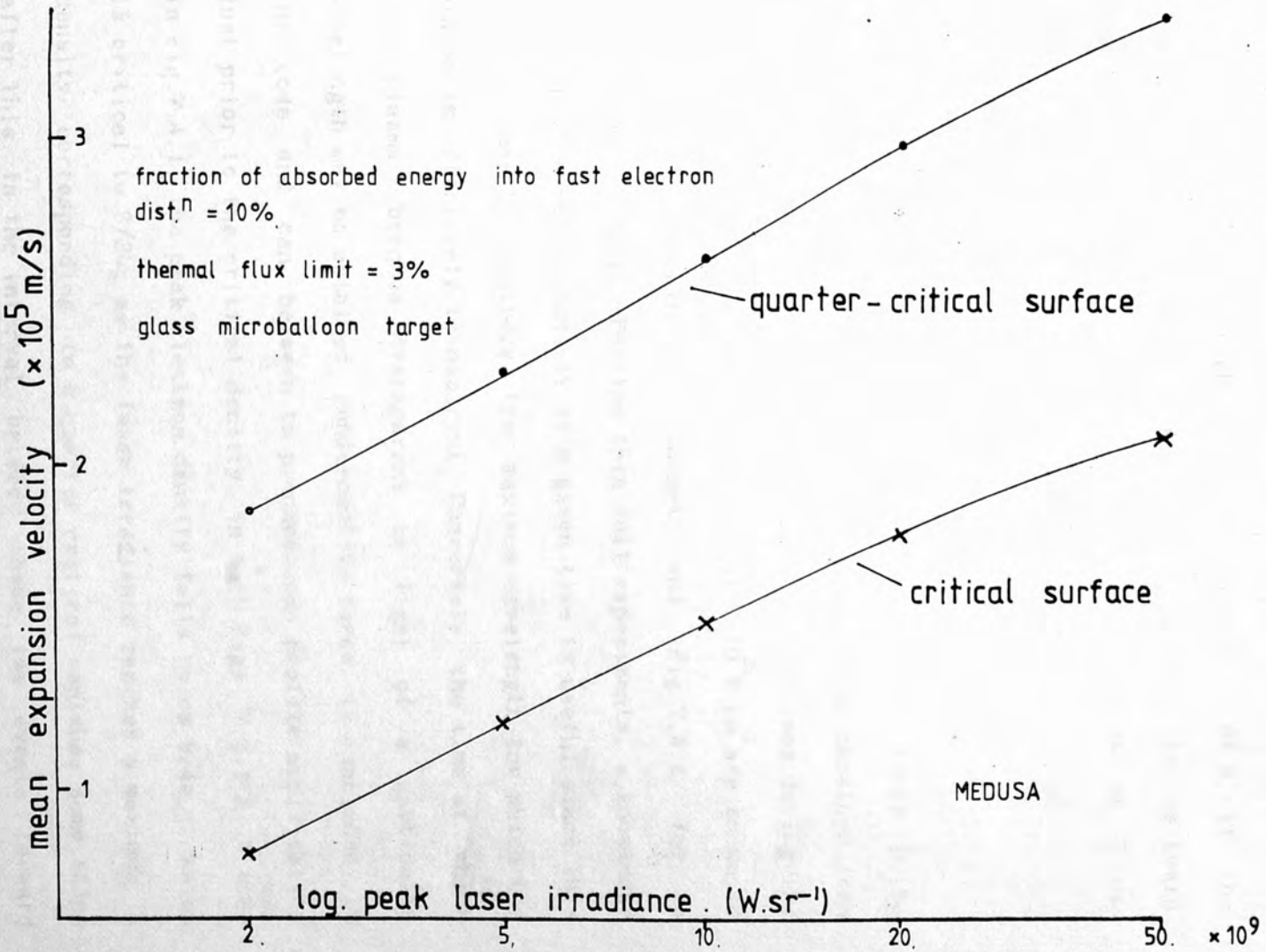
fraction of absorbed energy into fast electron dist.n = 10%
thermal flux limit = 3%
glass microballoon target
quarter-critical surface
critical surface
MEDUSA
mean expansion velocity (x 10^5 m/s)
log. peak laser irradiance . (W.sr^-1)
1
2
3
2.
5.
10.
20.
50.
x 10^9

target with a 90% fast elctron fraction and a 3% thermal flux limit yielded a quarter critical expansion velocity of $3.3.10^5$m/s, which corresponds to a blue shift of 7.84 Å if the three-halves harmonic spectrum is viewed in the backward direction. This value was used in the earlier work on $3/2\omega_o$ spectra to remove the effect of the Doppler shift.

7.4 Density Profiles.

Values of the scalelength at various times in the laser pulse and the effect of ponderomotive force were also obtained from MEDUSA. The density profiles for three different times during the laser pulse, with a peak irradiance of 7.10^{15} W.cm^{-2} are shown in Fig.7.4.1 for a thin foil target, and Fig.7.4.2 for a microballoon target. For the thin foil experiments, a knowledge of the peak electron density at a given time is useful since this maximum density controls the maximum wavelength for which the plasma is effectively transparent. Conversely, the time at which the plasma becomes transparent to light of a particular wavelength may be obtained. Ponderomotive force is included in the code and can be seen to produce some profile modification just prior to the critical density, in both Figs. 7.4.1 & 7.4.2. In Fig.7.4.1, the peak electron density falls below $9/4n_c$, which is critical to $3/2\omega_o$, as the laser irradiance reaches a maximum. A density corresponding to a quarter critical vanishes some 100ps after this. In the interval between these two events forward scattered $3/2\omega_o$ light is observable. A similar analysis for

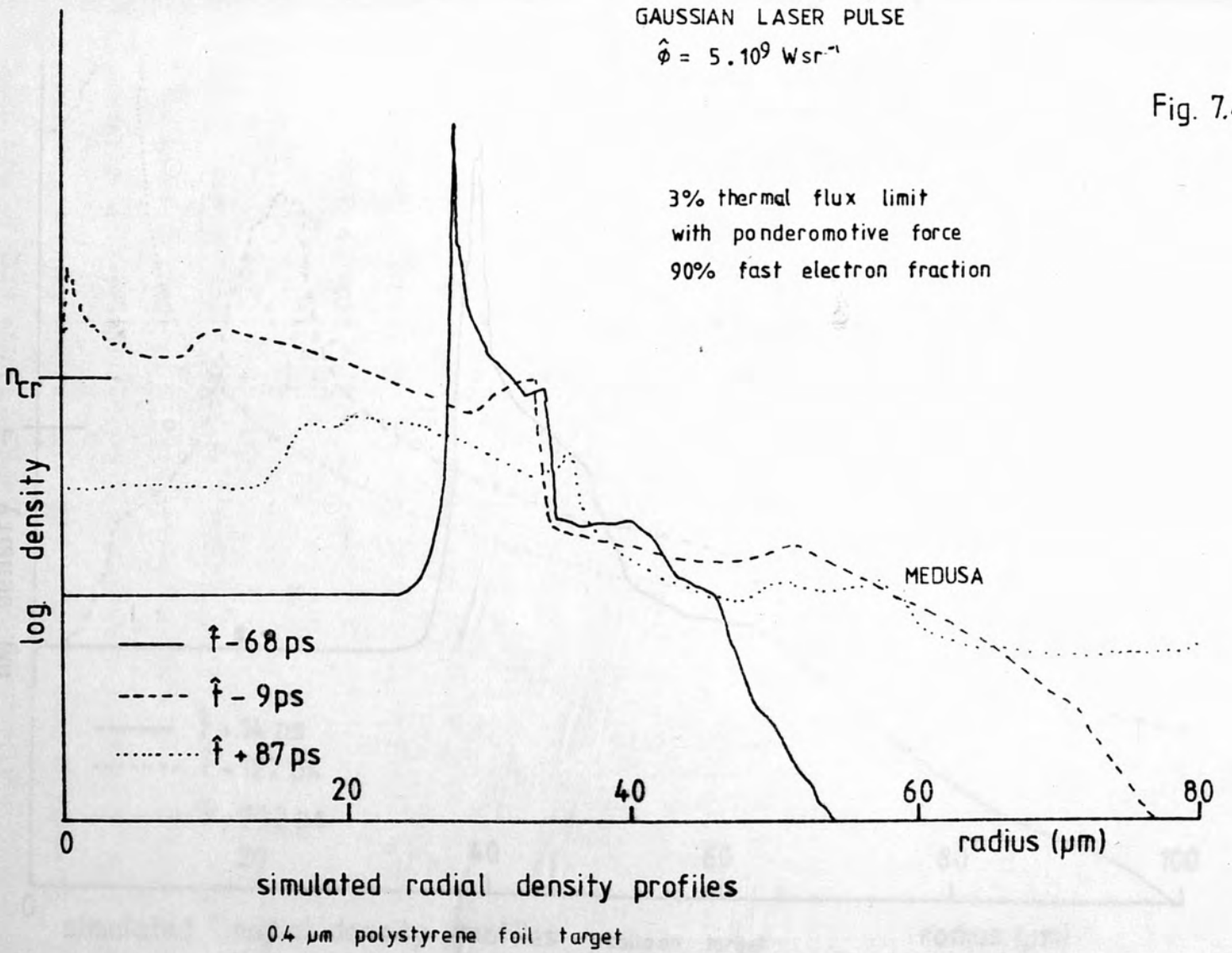

Fig. 7.4.1

simulated radial density profiles

0.4 μm polystyrene foil target

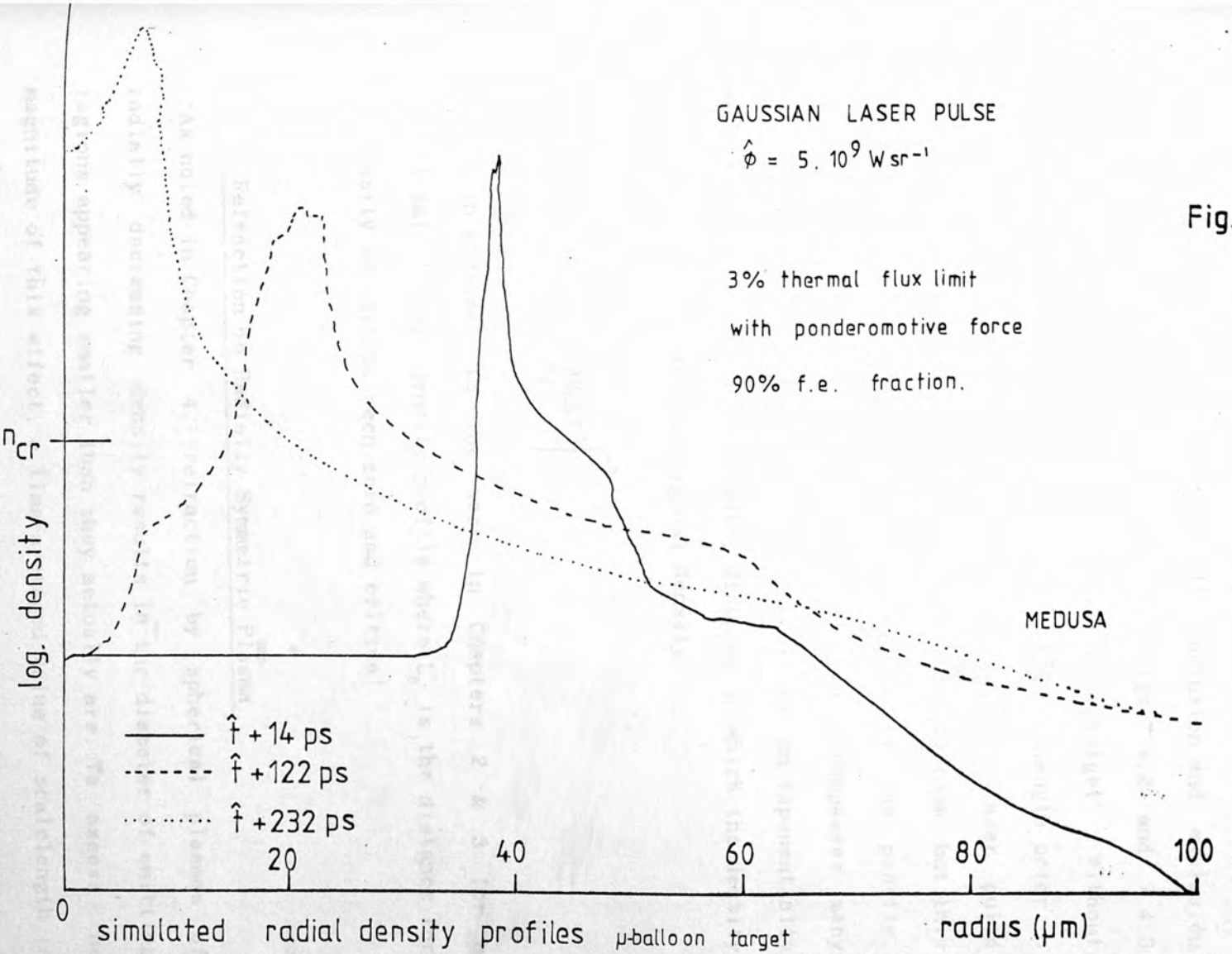
GAUSSIAN LASER PULSE
$\hat{\phi} = 5.10^9 \, W sr^{-1}$
3% thermal flux limit
with ponderomotive force
90% f.e. fraction.
n_{cr}
log. density
MEDUSA
$\hat{t}$ + 14 ps
$\hat{t}$ + 122 ps
$\hat{t}$ + 232 ps
0
20
40
60
80
100
simulated radial density profiles μ-balloon target
radius (μm)

Fig. 7.4.2.

forward scattered $2\omega_o$ light (for the time between a peak density of 4 x n_{cr} and n_{cr}) gives a duration ~70ps.

Direct comparison of the effect of the inclusion and exclusion of ponderomotive force appear in Figs.7.4.2 and 7.4.3 respectively; both for a microballoon target. Without ponderomotive force, a value of the density scalelength prior to the critical surface at a time near the peak of the laser pulse is obtained from Fig.7.4.3 as being approximately 13μm, but this value is reduced to ~1μm at a steepened portion of the profile. Since the concept of density scalelength encompasses many expressions, it is here defined appropiately for an exponentially decreasing profile, as the radial distance in which the density falls to a value e of its original density.

i.e.

$$L_n = \left(\frac{1}{n_e} \frac{dn_e(r)}{dr} \right)^{-1}$$

This is in contrast to the work in Chapters 2 & 3 for a theoretical linear density profile where L_n is the distance for the density to vary between zero and critical.

7.5 Refraction in Radially Symmetric Plasma.

As noted in Chapter 4, refraction by spherical plasmas of radially decreasing density results in the diameter of emitting regions appearing smaller than they actually are. To assess the magnitude of this effect, a time-averaged value of scalelength is assumed, and ray tracing performed to determine the actual

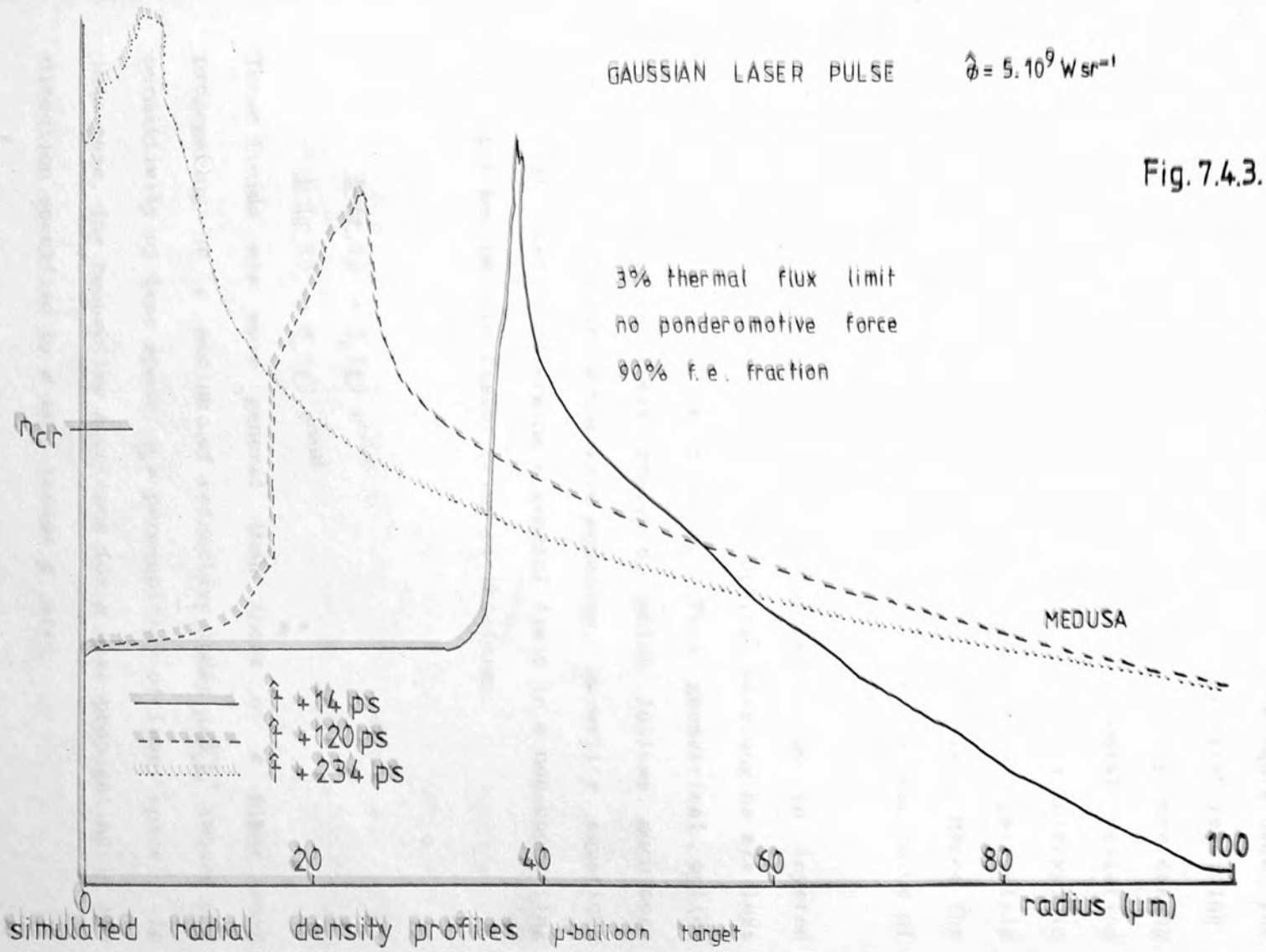

Fig. 7.4.3.

simulated radial density profiles μ-balloon target

position of the critical surface with the only variable being the position of that surface; the underdense profile remaining constant. So in this approach, an exponentially decreasing profile was assumed, and the incorporation of temporal variation in scalelength was not really necessary, since the interval in time when the Gaussian laser pulse was above the parametric threshold, and producing copious $2\omega_0$ light, was small. Hence the change in scalelength over this time was ignored, a mean value of 13.5μm being used in the code.

Born and Wolf[22] have quoted a theory for refraction in layered media, which is applicable if the optical wavelengths are less than the scalelengths; i.e. $\lambda << L_n$. This geometrical optics approximation makes their analysis, which follows, much more simple due to its use in the wave equation. Maxwell's equations are first used to determine a general field in a non-conducting isotropic medium, the fields being of the form;

$$\underline{E}(\underline{r},t) = \underline{E}_0(\underline{r})\, e^{-i\omega t}$$
$$\underline{H}(\underline{r},t) = \underline{H}_0(\underline{r})\, e^{-i\omega t}$$

These fields are more general than those of a plane wave propagating in a medium of refractive index $\mu = \sqrt{\varepsilon_0 \mu_0}$. ((where ε_0 = permittivity of free space, μ_0 = permeability of free space.)) In this case, the respective equations for a wave propagating in the direction specified by a unit vector $\underline{s}$, are:

$$E_o = \underline{e}\, e^{ik_o \mu(\underline{s}.\underline{r})} \quad , \quad \underline{H}_o = \underline{h}\, e^{ik_o \mu(\underline{s}.\underline{r})}$$

where $\underline{e}$ and $\underline{h}$ are constant and generally complex vectors. A specific case of a monochromatic electric dipole field in a vacuum, the relations are:

$$E_o = \underline{e}\, e^{ik_o r} \quad , \quad H_o = \underline{h}\, e^{ik_o r}$$

r being the distance from the dipole.

These examples suggest that in regions several wavelengths away from the sources, more general fields of the form:

$$E_o = \underline{e}(\underline{r}) e^{ikS(\underline{r})} \quad , \quad H_o = \underline{h}(\underline{r}) e^{ikS(\underline{r})} \qquad - 7.5.2$$

are represented, where $S(\underline{r})$ is a real scalar function of position and is known as the optical path, and $\underline{e}(\underline{r})$ and $\underline{h}(\underline{r})$ are vector functions of position.

With expressions 7.5.2 as trial solutions, application of Maxwell's equations can lead to a set of relations between $\underline{e}$, $\underline{h}$ and S, and for large k_o (small λ_o), S can satisfy a differential equation which is independent of the amplitude vectors $\underline{e}$ and $\underline{h}$. The three equations of most use in this respect which are shown to arise from Maxwell's equations and vector identities are:

$$\left.\begin{aligned} \nabla S \times \underline{h} + \varepsilon_o \underline{e} &= 0 \\ \nabla S \times \underline{e} - \mu_o \underline{h} &= 0 \\ \underline{e} \cdot \nabla S &= 0 \end{aligned}\right\} - 7.5.3$$

The solution of the first two of these equations is non-trivial only if the associated determinant vanishes (consistency

condition). Eliminating $\underline{h}$, they give:

$$\frac{1}{\mu_o}\left((\underline{e}\cdot\nabla S)\nabla S - \underline{e}(\nabla S)^2\right) + \varepsilon_o\underline{e} = 0 \qquad - 7.5.4$$

and using the third equation of 7.5.3,

$$(\nabla S)^2 = \mu^2 \qquad - 7.5.5$$

where μ = the refractive index, since $\mu = \sqrt{\mu_o\varepsilon_o}$.

Equation 7.5.5 is known as the eikonal equation which in general is the description of the time harmonic solutions of the wave equation. The surfaces corresponding to $S(r)$ = constant are the geometrical wave fronts.

If a light ray in an isotropic medium is at an orthogonal trajectory to the geometrical wave front, then these rays are themselves oriented curves whose direction coincides everywhere with the direction of the average Poynting vector. From the eikonal equation;

S is a unit vector ($\underline{R}$ say)

$$\underline{R} = \frac{\nabla S}{\mu} = \frac{\nabla S}{|\nabla S|} \qquad - 7.5.6$$

and if r(s) denotes the position vector of a point P on a ray, as a function of the length of arc, s, of the ray, then $\frac{d\underline{r}}{ds} = s$ and the equation of the ray may be written as

$$\mu\frac{d\underline{r}}{ds} = \nabla S \qquad - 7.5.7$$

This specifies the rays in terms of S, but it is more convenient to have it in terms of the refractive index function $\mu(r)$.

Differentiating 7.5.7 with respect to s gives:

$$\frac{d}{ds}\left(\mu \frac{dr}{ds}\right) = \frac{d}{ds}(\nabla S)$$

$$= \frac{dr}{ds} \cdot \nabla(\nabla S)$$

$$= \frac{1}{\mu} \nabla S \cdot \nabla(\nabla S) \text{ , from 7.5.7}$$

$$= \frac{1}{2\mu} \nabla((\nabla S)^2)$$

$$= \frac{1}{2\mu} \nabla \mu^2 \quad \text{from 7.5.5}$$

$$\frac{d}{ds}\left(\mu \frac{dr}{ds}\right) = \nabla \mu \qquad - 7.5.8$$

which is a general vector form for the light rays, and in particular for an homogeneous medium μ = constant and 7.5.8 reduces to

$\frac{d^2 r}{ds^2} = 0$, the light ray paths being straight lines.

To consider the case of interest here, to a good approximation the plasma formed from irradiation of a spherical target is radially symmetrical, so that the refractive index is a function of electron density, and hence radial position only.

i.e.

$\mu = \mu(r)$ - 7.5.9 The variation of the vector $\underline{r} \times (\mu(\underline{r}) \cdot \underline{s})$ is of importance here, so

$$\frac{d}{ds}(\underline{r} \times \mu \underline{s}) = \frac{d\underline{r}}{ds} \times \mu \underline{s} + \underline{r} \times \frac{d}{ds}(\mu \underline{s})$$

The first term on the RHS vanishes, since $\frac{d\underline{r}}{ds} = s$, and from 7.5.8, the second term = $r \times \nabla\mu$. From 7.5.9

$\nabla\mu = \frac{\underline{r}}{r}\frac{d\mu}{dr}$, the second term also vanishes.

Hence $\underline{r} \times \mu\underline{s}$ = constant, or more conveniently, if Θ is the angle between the position vector $\underline{r}$ and the tangent to the point r on the ray, then:

$\mu r \sin\Theta$ = constant = K along any given ray - 7.5.10

This expression is known as Bouguer's formula, and is the general equation used for ray tracing in radially symmetric refracting media. In two dimensions, with an ordinate (y) and an abcissa (z) and the angle between the local tangent to the ray and the abcissa being ϕ , then equation 7.5.10 becomes:

$$(y - z \tan\phi) \cos\phi = (y \cos\phi - z \sin\phi) = K, \quad - 7.5.11$$

This is shown diagramatically in Fig.7.5.1. Putting equation 7.5.2 in a form for use with $\sin\phi$ explicitly, using $\sin^2\phi + \cos^2\phi = 1$, and solving the quadratic gives:

$$\sin\phi = -\frac{Kz}{z^2 + y^2} \pm \left(\frac{y^2}{z^2 + y^2} \left(1 - \frac{K^2}{\mu^2 (z^2 + y^2)} \right) \right)^{1/2} \quad - 7.5.12$$

+ve and -ve denoting the sign of the abcissa (z). Successive solutions of equation 7.5.12 have been achieved with a FORTRAN computer code (TRACE). This traces rays into the plasma from various initial positions $(y_o\ z_o)$, and angles of incidence (ϕ_o), and plots the ray trajectory graphically. The position of the critical density and the density scalelength for an exponentially decreasing profile are variable parameters, and the general program was modified for particular applications. Common

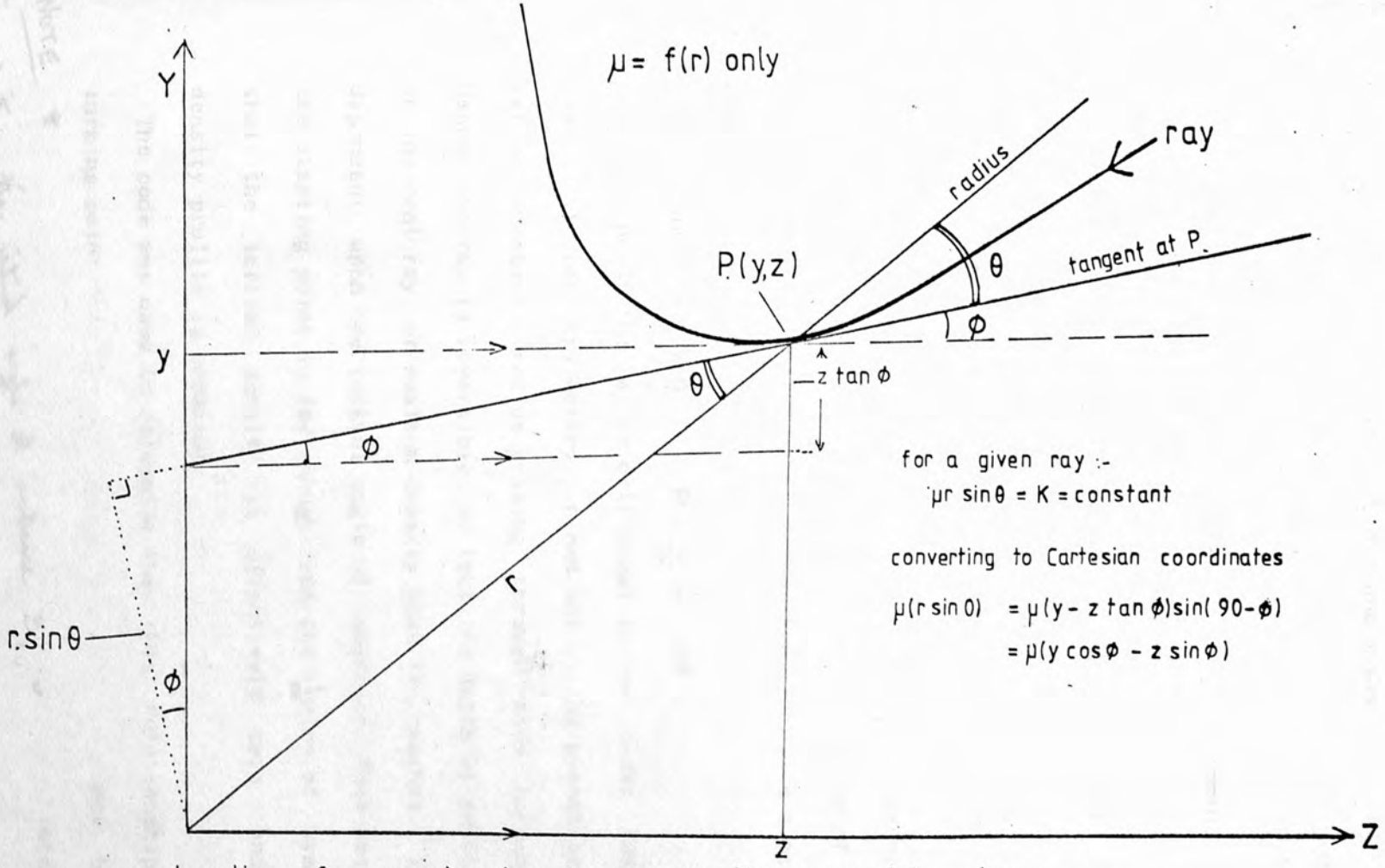

construction for ray tracing in spherically symmetric plasma

Fig. 7.5.1.

expressions for the increments in y and z are:

$$y_{i+1} = y_i \ \delta z \tan \phi$$

and

$$z_{i+1} = z_i - \delta z \quad \text{where } \delta z \text{ is the increment.}$$

whilst the density profile was expressed by:

$$n_e = n_{cr} \exp - \left(\frac{r - r_{cr}}{L_n} \right)$$, where r is the radius in question

and r_{cr} the critical radius.

When traced into an increasing density, non radially, the ray is refracted away from the local radius, until it reaches a point where it starts to be refracted away from the centre of symmetry. At this point, the turning point, the radius is a minimum, so that:

$$\frac{d}{d\Theta} \left| \mu r \sin\Theta \right| = 0 \qquad \Theta = \frac{\pi}{2} = 90^\circ .$$

At this point the ray is orthogonal to the local radius, and the total ray trajectory in and out of the plasma is a mirror reflection about a radius passing through this turning point. Hence the ray is reversible, so that the depth of penetration of an incident ray, or maximum density that it reaches, is solely dependent upon the initial angle of incidence. This assumes that the starting point is far enough from the centre of symmetry so that the initial density is effectively zero, and that the density profile is constant.

The code was used to determine the this relationship between turning point l- ... ence, but in the ... location, as

NOTE *
For clarity, the initial angle of incidence, θ_i, is defined as $\arctan\left(\frac{y}{z}\right)$ at the surface where $\epsilon_T = 0.993$

expressions for the increments in y and z are:

$$y_{i+1} = y_i \; \delta z \tan \phi$$

and

$$z_{i+1} = z_i - \delta z \quad \text{where } \delta z \text{ is the increment.}$$

whilst the density profile was expressed by:

$$n_e = n_{cr} \exp - \left(\frac{r - r_{cr}}{L_n} \right)$$, where r is the radius in question

and r_{cr} the critical radius.

When traced into an increasing density, non radially, the ray is refracted away from the local radius; until it reaches a point where it starts to be refracted away from the centre of symmetry. At this point, the turning point, the radius is a minimum, so that:

$$\frac{d}{d\Theta} \left| \mu r \sin\Theta \right| = 0 \qquad \Theta = \frac{\pi}{2} = 90^{\circ}.$$

At this point the ray is orthogonal to the local radius, and the total ray trajectory in and out of the plasma is a mirror reflection about a radius passing through this turning point. Hence the ray is reversible, so that the depth of penetration of an incident ray, or maximum density that it reaches, is solely dependent upon the initial angle of incidence. This assumes that the starting point is far enough from the centre of symmetry so that the initial density is effectively zero, and that the density profile is constant.

The code was used to determine the this relationship between turning point location and initial angle of incidence, but in the first instance it was used for critical surface location, as

determined by $2\omega_0$ light. As this light is emergent from the region of the critical surface, it is therefore emerging from an electron density a quarter that of its own critical density, and so to achieve an accurate procedure to find the true location, the following sequence was adopted. It was seen from preliminary computer runs that if $2\omega_0$ light is emitted in all directions from the critical surface, then the maximum true radius of emission compared with the observed radius (i.e. after refraction), is due to a ray which is emitted tangentially to the actual radius, and so all values of error refer to the maximum value.

The true $2\omega_0$ emitting region was determined as follows: With the critical density radius in the code set at just less than the radius of the observed emission, a ray was traced in. Since the f/no of the optics receiving the $2\omega_0$ light was not small, it was assumed that a beam parallel to the optic axis was emerging, and so initially a ray parallel to this axis was traced in. This ray is refracted until its turning point is reached.

If this turning point then corresponds within a set precision to an electron density a quarter of that for which is critical to the ray, then the result is accepted and an enhanced value of the critical surface radius is that of the turning point radius. If this turning point was outside the precision limit, then the whole density profile was moved incrementally outwards and the ray trace repeated. This sequence was performed until the result was acceptable. The fractional error between the observed and the enhanced (computed) critical surface radii as a function of

the observed radius of $2\omega_0$ light is shown in Fig.7.5.2, and values around 23% are seen.

In the case of three-halves harmonic emission generated close to a quarter critical, this corresponds to light emerging from a density one ninth of its own critical density, and so the error of radius measurement due to refraction is negligible, being less than the resolution limit of the optics used.

To determine the penetration depth of an ω_0 ray focussed onto the target, it has already been seen that for a ray incident upon a linear density profile, the turning point can be at a density far removed from the critical surface, and this density is dependent only upon the initial angle of incidence (θ) determined by $n_{TP} = n_{cr}\cos^2\theta$ This is derived from Snell's law since in plane geometry $\mu\sin\theta$ is a constant along the ray. For spherical geometry, and a more realistic density profile, determination of the depth of penetration was carried out using the ray trace code. The proximity of the turning point to the critical surface is of interest in determining the possible availability of electron plasma waves due to resonant, linear and non-linear absorption methods, and hence a maximum value of second harmonic peak frequency shift due to recombination of these waves, and the incident wave.

To use the code for this purpose, rays were traced in from a given position some distance away from the centre of symmetry so that the electron density is effectively zero and the refractive index unity. If a series of rays parallel to any one radius are

Correction of critical surface location due to refraction of $2\omega_o$ emission.

Fig. 7.5.2

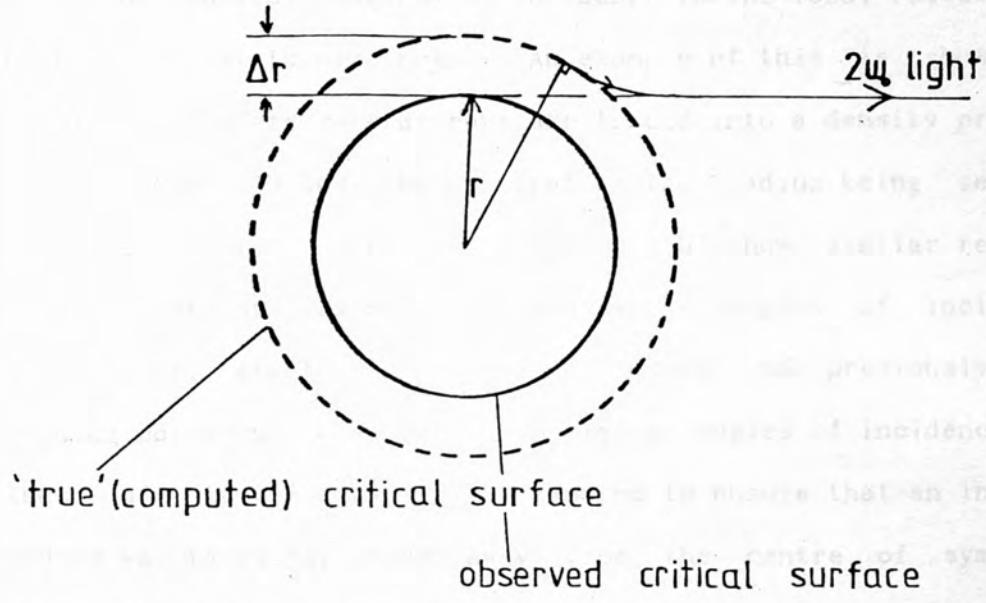

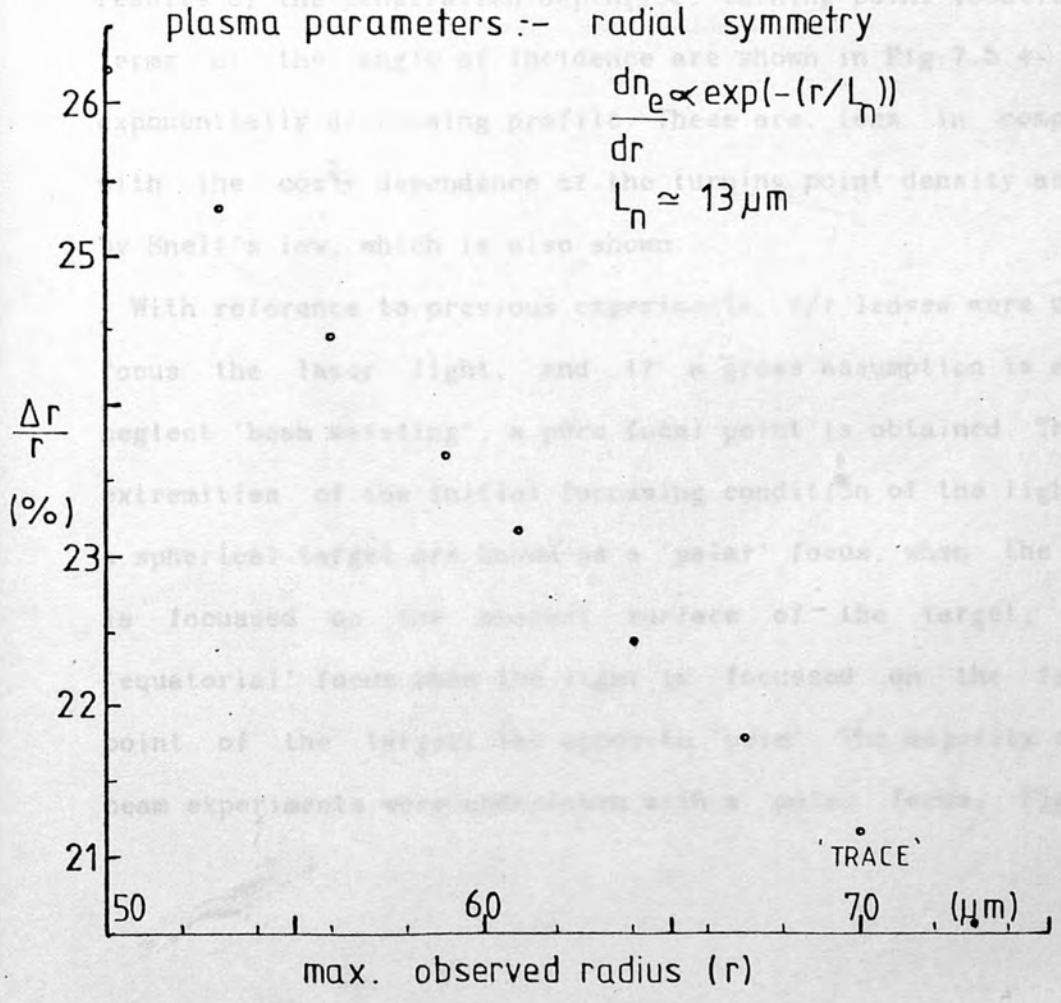

traced in towards the centre of symmetry, then they have different initial angles of incidence to the local radius, and hence different turning points. An example of this is shown in Fig.7.5.3(a) where several rays are traced into a density profile of scalelength 13.5μm, the critical surface radius being set at 50um. A similar exercise in Fig.7.5.3(b) shows similar results for incident rays, except that those whose angles of incidence are greater start at a greater radius than previously. The turning points of these rays with similar angles of incidence to those of Fig.7.5.3(a) were compared to ensure that an initial radius was taken far enough away from the centre of symmetry where the density was truly zero. Having satisfied this, the results of the penetration depth(i.e. turning point location) in terms of the angle of incidence are shown in Fig.7.5.4, for an exponentially decreasing profile. These are less in comparison with the $\cos^2\theta$ dependence of the turning point density as given by Snell's law, which is also shown.

With reference to previous experiments, f/1 lenses were used to focus the laser light, and if a gross assumption is made to neglect 'beam waisting', a pure focal point is obtained. The two extremities of the initial focussing condition of the light onto a spherical target are known as a 'polar' focus, when the light is focussed on the nearest surface of the target, and an 'equatorial' focus when the light is focussed on the farthest point of the target; the opposite 'pole'. The majority of twin beam experiments were undertaken with a polar focus, Fig.7.5.5

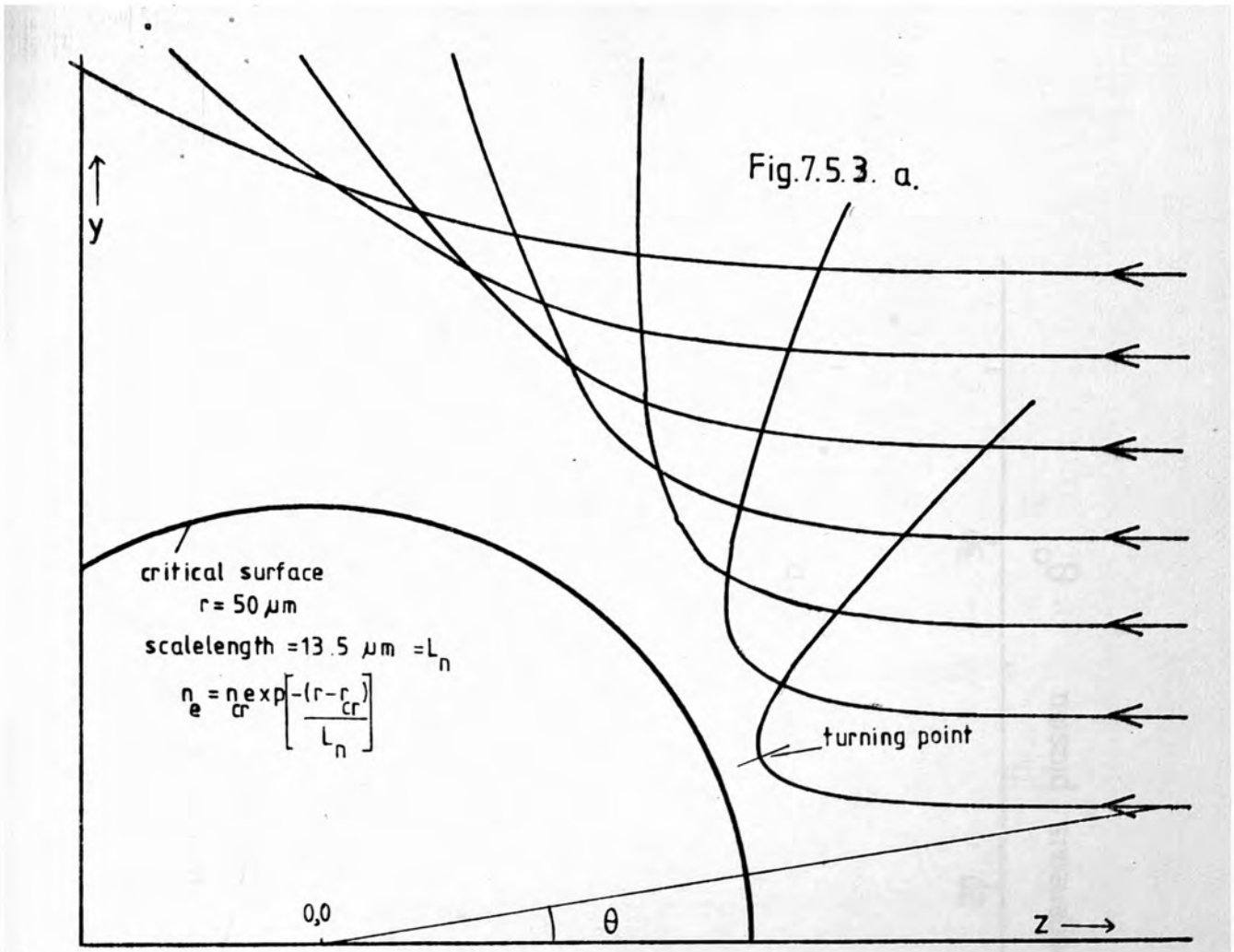
Fig.7.5.3. a.
y
critical surface
r = 50 μm
scalelength = 13.5 μm = L_n
$n_e = n_{cr} \exp\left[\frac{-(r-r_{cr})}{L_n}\right]$
turning point
0,0
θ
z

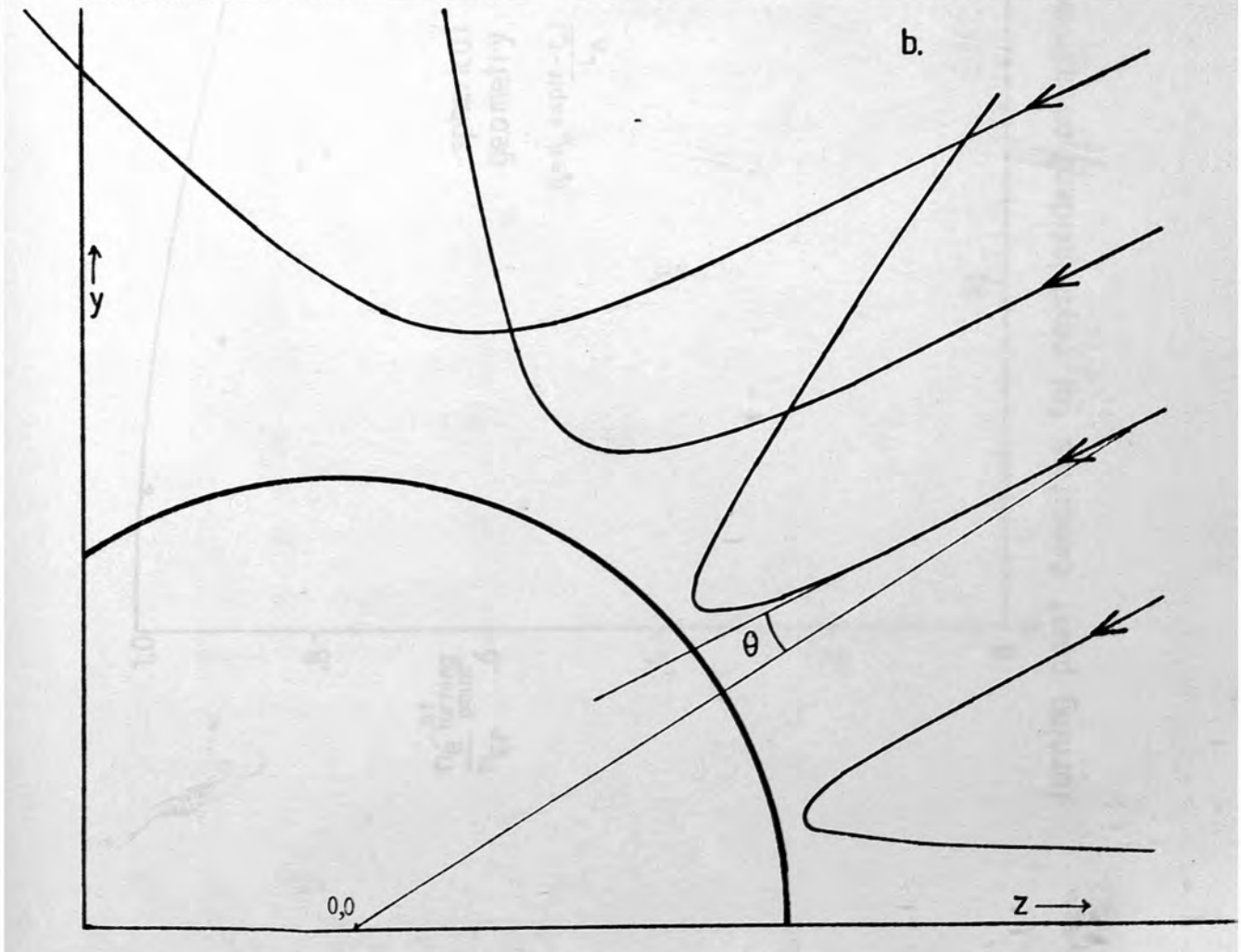
b.
y
θ
0,0
z

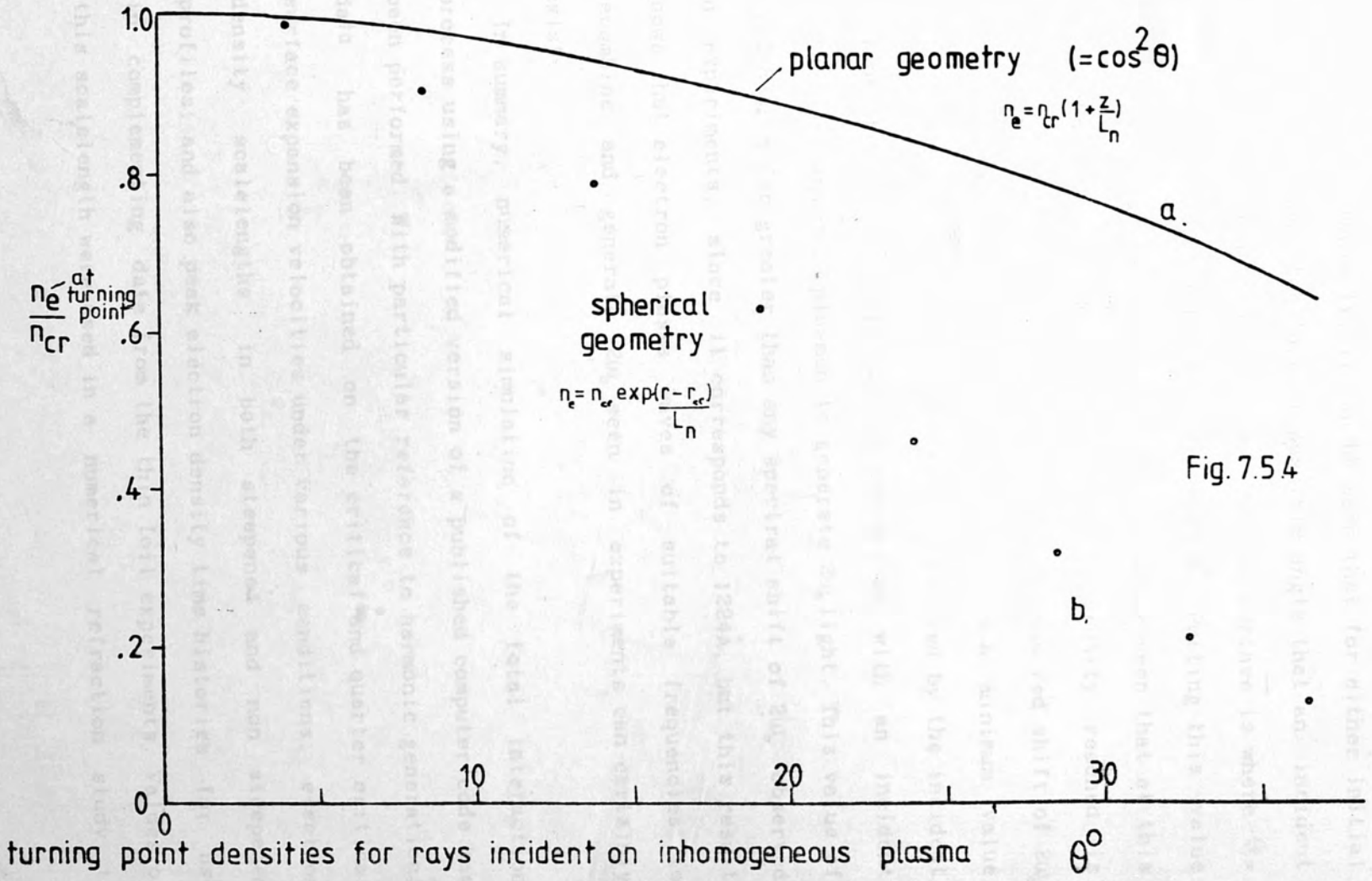

Fig. 7.5.4

turning point densities for rays incident on inhomogeneous plasma

showing the two focussing conditions diagramatically. As the plasma expands radially, it can be seen that for either initial focussing condition, the largest possible angle that an incident ray can make with the expanding critical surface is where Θ = arctan(f/no/2), which for our lenses = 26.6°. Putting this value into the spherical case of Fig.7.5.4, it can be seen that at this maximum angle, the minimum value of electron density reached is $0.39n_{cr}$. This value gives a limit to the maximum red shift of $2\omega_o$ generated by the linear process, since it gives a minimum value of the electron plasma wave frequency excited by the incident laser and hence available for recombination with an incident photon, or another plasmon to generate $2\omega_o$ light. This value of $\omega_{pe} = 0.62\omega_o$ is far greater than any spectral shift of $2\omega_o$ observed in experiments, since it corresponds to 1224Å, but this result shows that electron plasma waves of suitable frequencies to recombine and generate $2\omega_o$ seen in experiments can certainly exist.

In summary, numerical simulation of the total interaction process using a modified version of a published computer code has been performed. With particular reference to harmonic generation, data has been obtained on the critical and quarter critical surface expansion velocities under various conditions; electron density scalelengths in both steepened and non steepened profiles; and also peak electron density time histories for use in complementing data from the thin foil experiments. Values of this scalelength were used in a numerical refraction study to

observe the effect of refraction upon observed harmonic light, and also to determine the position of the turning point of incident light under various conditions. The results obtained in these numerical studies have been used in context with previous experimental data and has considerably improved the accuracy of observed spectral and spatial details due to taking the effects of Doppler shift and refraction, respectively, into account.

Fig. 7.5.5.

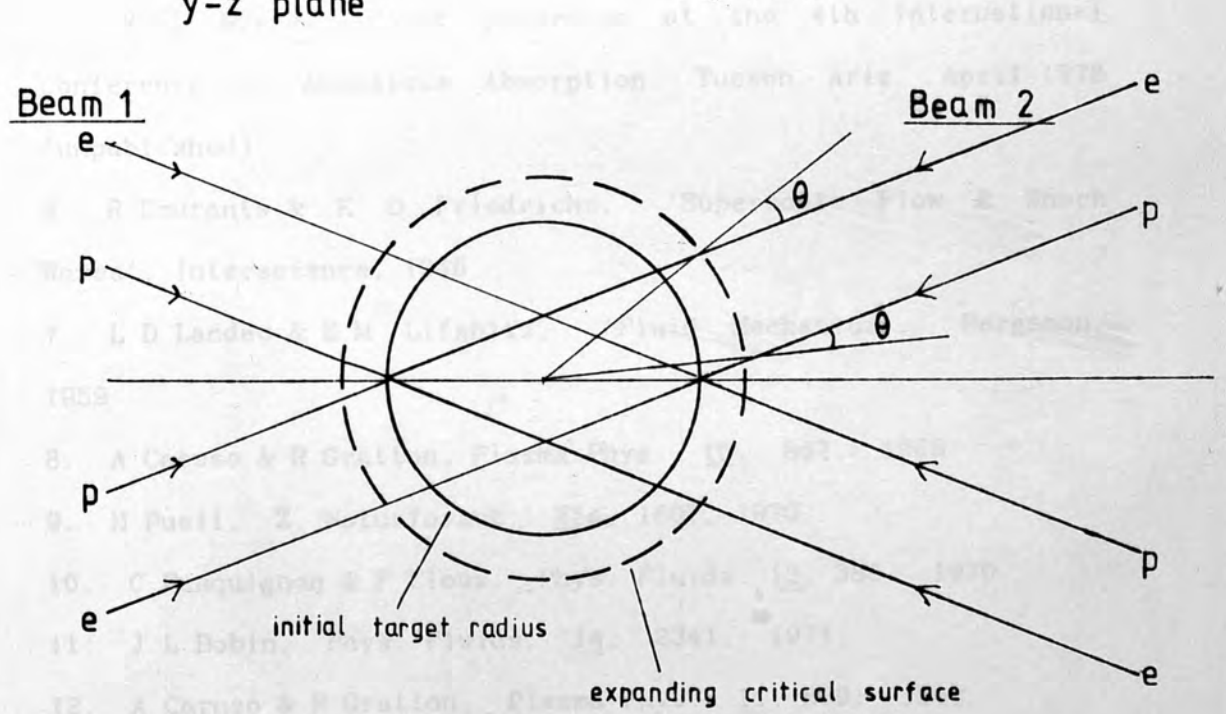

p - beam extremities for 'polar' focus.

e - " " " 'equatorial' focus.

Initial focussing conditions

Chapter 7 - References.

1. MEDUSA - A 1-d numerical model for laser fusion calculations. Culham Laboratory Report CLM R130, HMSO 1973 J P Christiansen, D E T F Ashby & K V Roberts.

2. OLYMPUS - A standard package for initial value FORTRAN programs, Culham Laboratory Report CLM P373 HMSO J P Christiansen & K V Roberts.

3. MEDUSA - A 1-d laser fusion code. Culham Laboratory Report CLM P374 HMSO J P Christiansen, D E T F Ashby & K V Roberts.

4. R G Evans, Rutherford Laboratory Report No.RL-78-039 Section 3.5.1

5. R L Morse, Paper presented at the 4th International Conference on Anomalous Absorption, Tucson, Ariz. April 1978 (unpublished)

6. R Courants & K D Friedrichs, 'Supersonic Flow & Shock Waves', Interscience, 1948

7. L D Landau & E M Lifshitz, 'Fluid Mechanics', Pergamon, 1959

8. A Caruso & R Gratton, Plasma Phys. 10, 867, 1968

9. H Puell, Z. Naturforsch. 25a, 1807, 1970

10. C Fauquignon & F Floux, Phys. Fluids, 13, 386, 1970

11. J L Bobin, Phys. Fluids, 14, 2341, 1971

12. A Caruso & R Gratton, Plasma Phys. 11, 839, 1969

13. H Saltzmann, J. Appl. Phys. 44, 113, 1973

14. K A Brueckner & S Jorna, Rev. Mod. Phys. 46, 2, 1974

15. D R Gray, J D Kilkenny, M S White, P Blyth & D Hull, Phys. Rev. Letts. 39, 20, 1977

16. S Jackel, J Albritton & E Goldman, Phys. Rev. Lett. 35, 15, 1977

17. A Raven & O Willi, Phys. Rev. Lett. 43, 4, 1979

18. R Fedosejevs, I V Tomov, N H Burnett, G D Enright & M C Richardson, Phys. Rev. Lett. 39, 15, 1977

19. W C Mead, W L Kruer, J D Lindl & H D Shay, Bull. Am. Phys. Soc. 20, 1246, 1975

20. K A Brueckner, Phys. Rev. Lett. 36, 677, 1976

21. R L Morse & C W Nielson, Phys. Fluids. 16, 909, 1973

22. M Born & E Wolf, 'Principles of Optics', 4th ed. Pergamon 1970

-Chapter 8-

Conclusions.

8.1 The work presented in this thesis has given new information on the interaction of high intensity laser radiation with matter. The interactions have been studied through observations of the induced optical emission which occurs at the second and three halves harmonic frequencies of the incident laser light. These observations offer a valuable non-perturbing diagnostic technique provided that parameters of the observed light can be adequately related to plasma parameters. Hence experiments have sought firstly to clarify and confirm existing theoretical understanding of harmonic generation, and secondly to extend measurements of harmonics as a diagnostic, by performing measurements in five areas which may be summarised as follows.

1. Localised electron temperature.

At sufficiently high irradiances, the $2\omega_0$ radiation following the parametric decay instability can be used to determine electron temperature due to the position of the spectral peak, as seen from the theory of Silin. Taking into account the effect of Doppler shift by observing the expansion velocity and using numerical simulation methods to improve accuracy has given an electron temperature of typically 0.75keV. This is in good agreement with that obtained from MEDUSA simulations, and from X-ray absorber foil data. A difference in $2\omega_0$ spectral peak position between the linear and non-linear generation schemes due to the excited ion acoustic wave in the latter case has been

observed. This occured with thin foil targets or those with high Z so that the laser irradiance at critical was largely below threshold. However, in nearly all experiments this threshold was exceeded, and in confirmation the features of linear generation, (emission along the path of reflected light, and preferential p-polarised $2\omega_o$ light) were not found.

At quarter critical, the electron temperature was determined from the separation between the peaks of the blue and red shifted components of the $3/2\,\omega_o$ spectra. However, in this determination, a degree of uncertainty exists since there are four possible recombination schemes, (Fig.5.3.1.b), giving two grossly different expressions for electron temperature dependence on spectral separation. Values of $T_e \sim 1.9$ eV obtained from the Barr theory for specularly reflected or Brillouin scattered photon/plasmon and $T_e \sim 3.5$ keV for the incident photon/plasmon and three plasmon recombination schemes are high when compared with the .9 keV determined from absorber foil X-ray data, but may reflect on a mean value if a suprathermal electron component is included.

2. Density scalelengths.

From $3/2\,\omega_o$ backscattered spectra, a method for determining spatially averaged density scalelengths has arisen, which is much less dependent upon the actual recombination mechanism. All the mechanisms essentially give a forward scattered blue shifted spectral peak and a backscattered red one, so that for a massive target, the blue shifted peak in backscatter has travelled from

$n_{cr}/4$ to $9/4n_{cr}$ and returned, having been partially absorbed on route. On the assumption of a linear absorption coefficient, density scalelengths between 10 and 25 μm have been obtained, in excellent agreement with both numerical simulation and experimental interferometric density profile studies.

3. Critical and Quarter-Critical surface motions.

These have been studied to determine the Doppler shifts on harmonic spectra generated within expanding density profiles. It has been shown that observation of the expanding critically dense surface need not be experimentally time-resolved in order to determine a value of this velocity. Instead, only a knowledge of the peak critical surface extent is required, and numerical simulation can provide a value for the time over which this surface is expanding, and separately determine the refractive deviation of the emerging light. Hence the accurate radial increase per unit time can be evaluated in order to give a time averaged value of the expansion velocity. Numerically too, the influence of increased irradiance and changes in thermal flux limit and fast electron energy fraction on the expansion velocity have been studied to simulate experimental conditions as far as possible.

For the three halves harmonic, optical imaging has shown this to occur in 'bursts', localised in space and time, as confirmed by experiments involving achromatic optics, which ruled out any effects due to chromatic aberration, and temporal resolution, respectively.

4. Temporal development of plasma waves at ω_o and $\frac{\omega_o}{2}$

The most significant new information has been the observation of pulsation of both the second and three halves harmonic within the laser pulse duration. For the second harmonic, these bursts are also spectrally resolution limited, but this is not the case for the three halves harmonic, where a complete 'two component' spectrum occurs in each burst.

With the $2\omega_o$ spectra, estimates can be made on the minimum growth rate of the parametric instability, over the leading edge of a single burst. The rate of change of $2\omega_o$ intensity is $\sim 4.10^{12}\ s^{-1}$ after film calibration, and taking notice of the fact that the streak camera has a limited dynamic range of about 20. As seen in Chapter 3 from Nishikawa's theory, the growth rate of the instability is $2.8\ 10^{14}\ s^{-1}$, and this is in agreement with that

$$\gamma_{max} = \frac{1}{3}\left(\frac{m_e}{m_i}\right)^{1/3}\omega_{pe} \quad \text{— max. growth rate}$$

observed. Further experiments would require the camera to have a greater dynamic range, although greater temporal resolution could be achieved at the expense of spectral resolution.

The total spectral width of the $3/2\omega_o$ time resolved feature decreases with time. This may either be due to a corresponding drop in electron temperature, or, as shown in Section 6.6. a change in the relative propagation directions of the two plasmons from the two-plasmon decay. The latter is more probable, due to the density profile modification as seen in other experiments, which forces the plasmons to propagate at a greater angle to each

other with time. For both the $2\omega_0$ and $3/2\,\omega_0$ time-resolved spectra, pulsation was attributed to the growth and decay of excited waves; the alternative being that of an unstable region moving across the 'field of view' at calculated velocities greater than the expansion velocity, and hence less probable.

5. Thin-foil experiments.

The new technique of using thin-foil targets for harmonic studies has enabled some directional information to be obtained on the emitted spectrum. For $2\omega_0$, no difference in spectral composition between forward and backward scattered light was noticed. and a small shift between the two spectra gave an indication of critical surface motion before burnthrough. In the case of the $3/2\,\omega_0$ spectra, differences were noticed, and show a lack of a blue shifted peak in the backscattered direction. This observation is in agreement with theory but does not distinctly determine a single recombination scheme, as all four are possible. However, the existence of a definite red peak in the backscattered direction points to the mechanisms of incident photon/plasmon and three plasmon recombination to be the more probable.

In conclusion therefore, many new characteristics of harmonic emission have been observed, and related to plasma phenomena, such that the high potential of harmonic light as a plasma diagnostic technique has been usefully explored.

Appendix A.

A.1 Maxwell's equations.

$$\nabla \times \underline{E} = -\frac{d\underline{B}}{dt} \qquad - 1$$

$$\nabla \times \underline{H} = \varepsilon_o \frac{d\underline{E}}{dt} + \underline{J} \qquad - 2,\ \varepsilon_o = \text{permittivity of free space.}$$

$$\nabla . \underline{E} = \frac{p_q}{\varepsilon_o} \qquad - 3,\ p_q = \text{charge density}$$

$$\nabla . \underline{B} = 0 \qquad - 4$$

Also, $\underline{B} = \mu_o \underline{H}$, where $\underline{B}$ = magnetic flux density & μ_o = permeability of free space.

A.2 General wave equation from Maxwell's equations.

From equations 1 & 2:

$$\frac{dp_q}{dt} + \nabla . \underline{J} = 0 \qquad - \text{equation of continuity}$$

$$\underline{J}(\omega) = \underline{\sigma}(\omega) . \underline{E}(\omega) \qquad - \text{generalised Ohm's law}$$

where σ, the conductivity, is in general a tensor, and is assumed dependent on angular frequency but independent of the amplitudes of $\underline{E}$ and $\underline{H}$, for small amplitude waves.

Introducing a dielectric tensor as:

$$\varepsilon = 1 + \frac{\sigma}{i\omega\varepsilon_o}$$

and assuming that $\underline{E}$ and $\underline{H}$ vary in time and space as exp $i(\omega t - \underline{k}.\underline{r})$, where $\underline{k}$ is the propagation vector, it can be shown from equations 1, 2 & 4 that

$$\nabla \times \underline{E} = - i\mu_o \omega \underline{H} \qquad - 5$$

$$\nabla \times \underline{H} = i\omega\varepsilon_o \varepsilon \underline{E} \qquad - 6$$

$$\nabla . \underline{B} = 0$$

Taking the curl of equation 5 and substituting for $\underline{H}$ gives the

wave equation:

$$\nabla \times (\nabla \times \underline{E}) = \mu_o \varepsilon_o \omega^2 \varepsilon . \underline{E}$$

or alternatively, as $c^2 = (\mu_o \varepsilon_o)^{-1}$

$$\underline{k} \times (\underline{k} \times \underline{E}) + \left|\frac{\omega}{c}\right|^2 \varepsilon . \underline{E} = 0 \qquad - 8$$

This is the general wave equation for possible waves in a plasma, and if a solution exists then the determinant (|D|) of the coefficients of the components in $\underline{E}$ must vanish, if $\underline{E}$ is not zero. This equation, |D| = 0, is known as the dispersion relation, and is the relationship between ω and $\underline{k}$.

For a particular example, in an isotropic medium, ε is a scalar and is known as the dielectric constant, and for a transverse wave in this medium, $\underline{k} . \underline{E} = 0$

Therefore the wave equation becomes $\frac{c^2 k^2}{\omega^2} = \varepsilon_r$,

so that $k^2 c^2 = \omega^2 \varepsilon_r$, for a transverse wave in an isotropic medium.

Appendix B.

The Central Laser Facility of the Science Research Council.

A scientific case to establish the above Facility was formally made in November 1974, by several university physicists and members of the SRC active in laser-plasma research, after national and international interest in the interaction of high power laser radiation with matter necessitated a laser system approaching the 'state of the art', and hence unavailable to individual university groups. This Facility was approved, and subsequently set up in existing buildings at the Rutherford Laboratory, using a system based on neodymium doped glass and YAG

as the active medium; its output being of wavelength 1.06 μm. Single beam operation was achieved in mid-1976, and the first twin beam target shot in April 1977, each beam then giving a maximum of 150GW in a 100ps FWHM Gaussian pulse. Subsequent Facility development now permits operation of two interaction areas with either two or six beams, in separate experiments. Work presented here was performed with the Facility in its initial configuration of single/twin beam operation, and the laser suite at this time is represented schematically in Fig.B.1 The 16mm diameter Yag mode-locked oscillator and the preamplifier were run continuously on a 1/3 Hz rep. rate for thermal stability, and a single pulse switched out of the mode-locked train with a Pockels cell. Several stages of amplification use Nd doped glass rods of increasing diameters, and the final stages, after the beam was split for twin beam operation, use Brewster angle glass discs, of 108mm clear aperture, and 'pumped' circumferentially. For initial single (East) beam work the final disc amplifier was not used, as only low powers were required. The final beam direction for this single beam operation is indicated by a '1' in Fig. B.1, and the East and West twin beams by '2's, after passage through the disc amplifiers.

The target room.

From the air-conditioned and dust-free laser suite, the beams passed directly into the target room and were deflected to arrive simultaneously at the target plane along opposing directions of a common axis (z). The target chamber itself was spherical and ~1m

in diameter with several optical access ports in different planes. A schematic of the chamber with the two focussing lenses shown, appears in Fig. B.2. The majority of diagnostic equipment external to the chamber was situated on the East beam side, as shown in the diagram of the initial experimental arrangement in the target room, in Fig B.3. Facility for a second or fourth harmonic probe beam or a separate ruby laser probe made use of the North/South axis at 90° to the axis of irradiation. The harmonic probe beams were generated in the laser room by frequency doubling a small portion of the main beam using temperature stabilised AD*P crystal(s). Focussing of the target prior to a shot was performed by using a CW YAG laser, and imaging the retroreflected light from the target onto an infrared vidicon which provided an image on CCTV monitors. The focal spot size, as seen as a bright circle on the monitor, was adjusted to be a minimum for optimum focus, Subsequent adjustment was made for the effect of thermal 'zooming', and also for any required difference in the focussing condition.

Focussing lenses.

The main focussing lenses used were of two varieties, the more recent one (ICOS) only became available during the course of this work and consequently was only used in later experiments. The lenses used initially, (SORO, France) were of singlet construction, plano convex, and had a central, non-cylindrical hole to prevent breakdown. A cross-section of this lens is shown in Fig. B.4. The lens design developed subsequently (ICOS),

permitted a smaller focal spot size to be obtained, and uses two elements; one component with spherical surfaces, and the other aspheric. No central hole was found necessary with this design, as a cross-section in Fig. B.5 shows, and also the design was figured for both 1.06 and 0.53μm, so that the lens could be used for experiments with the fundamental laser wavelength, and also those with frequency doubled incident light @ 0.53μm.

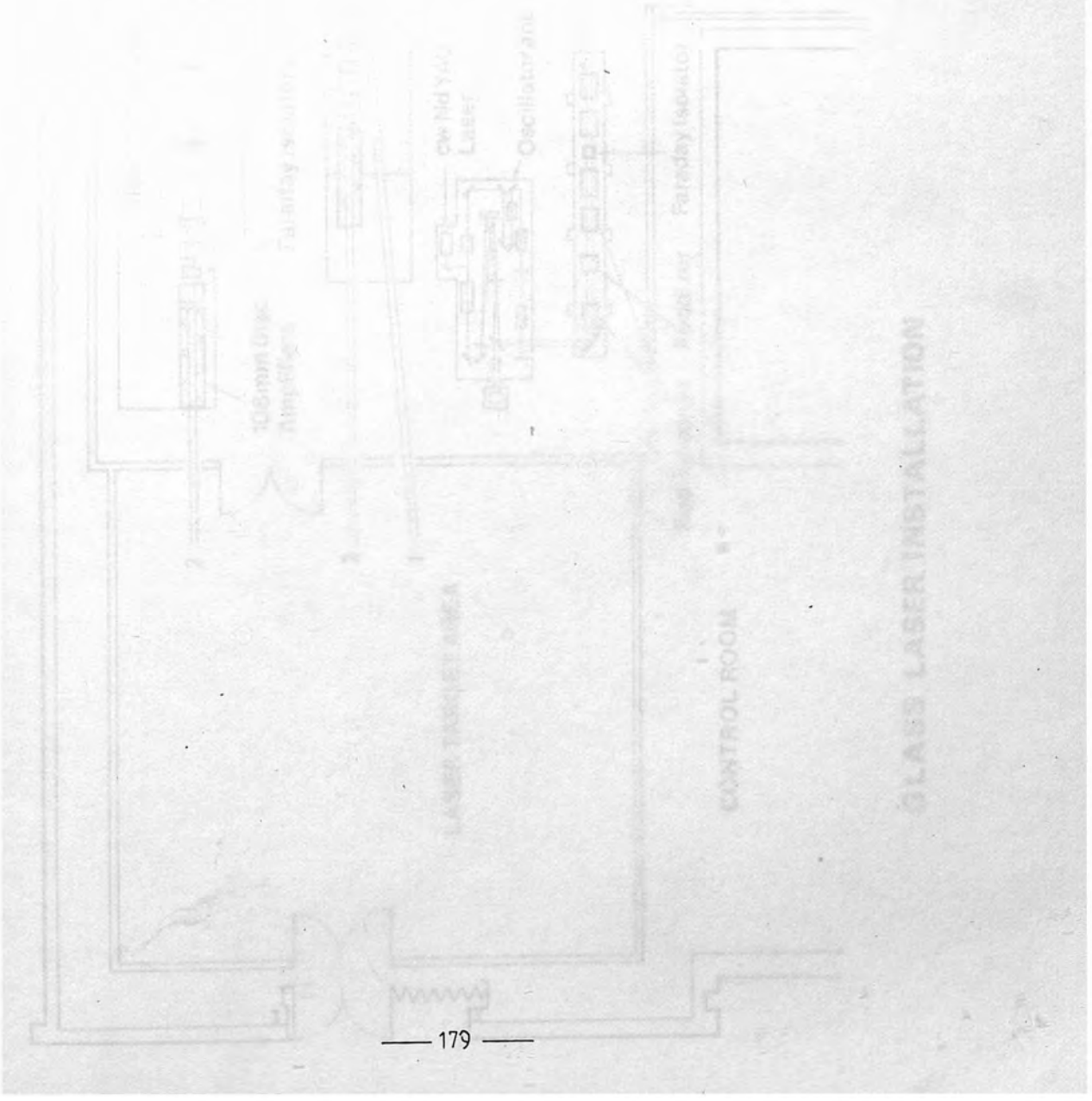

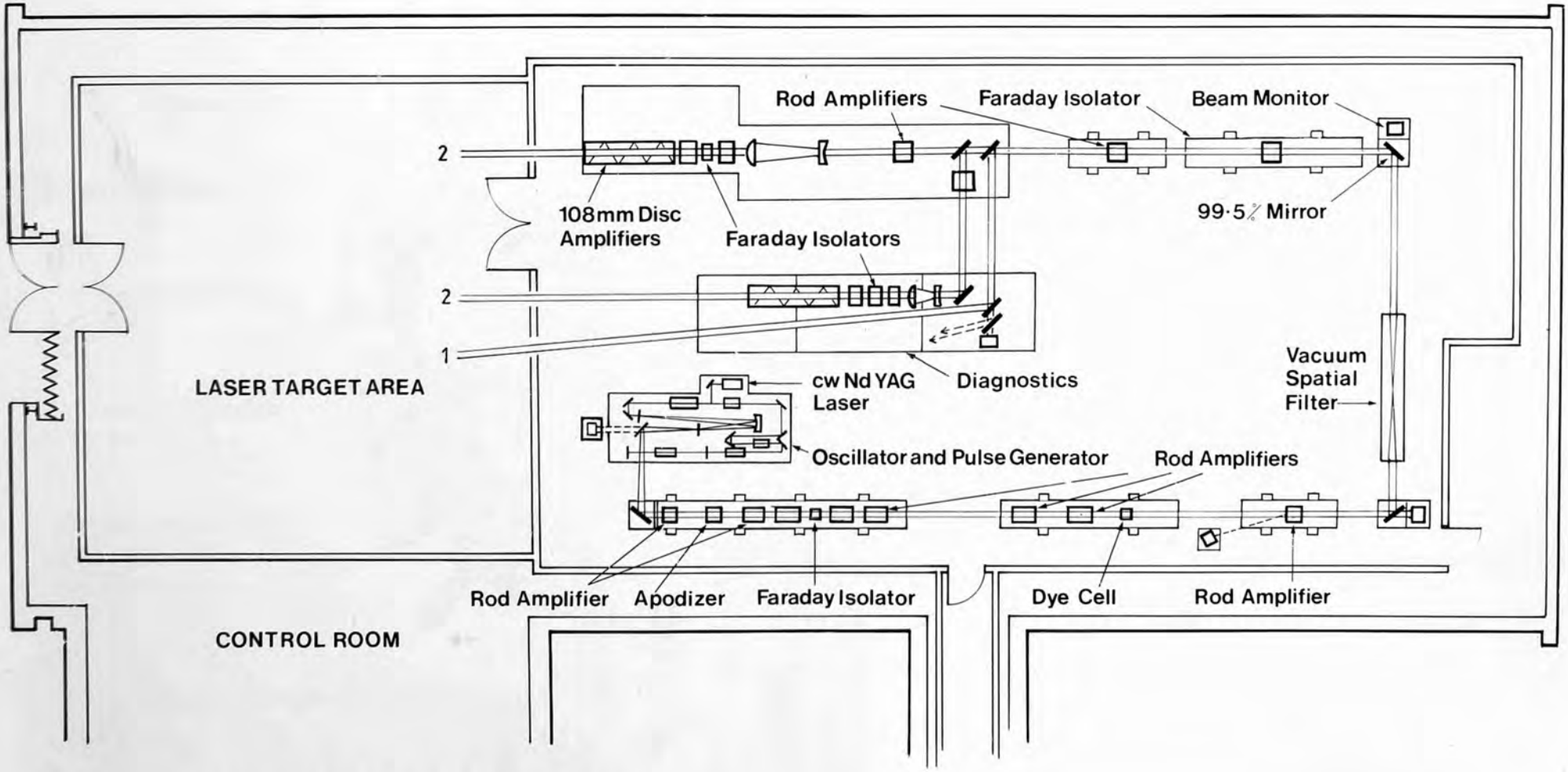

GLASS LASER INSTALLATION

Fig. B1

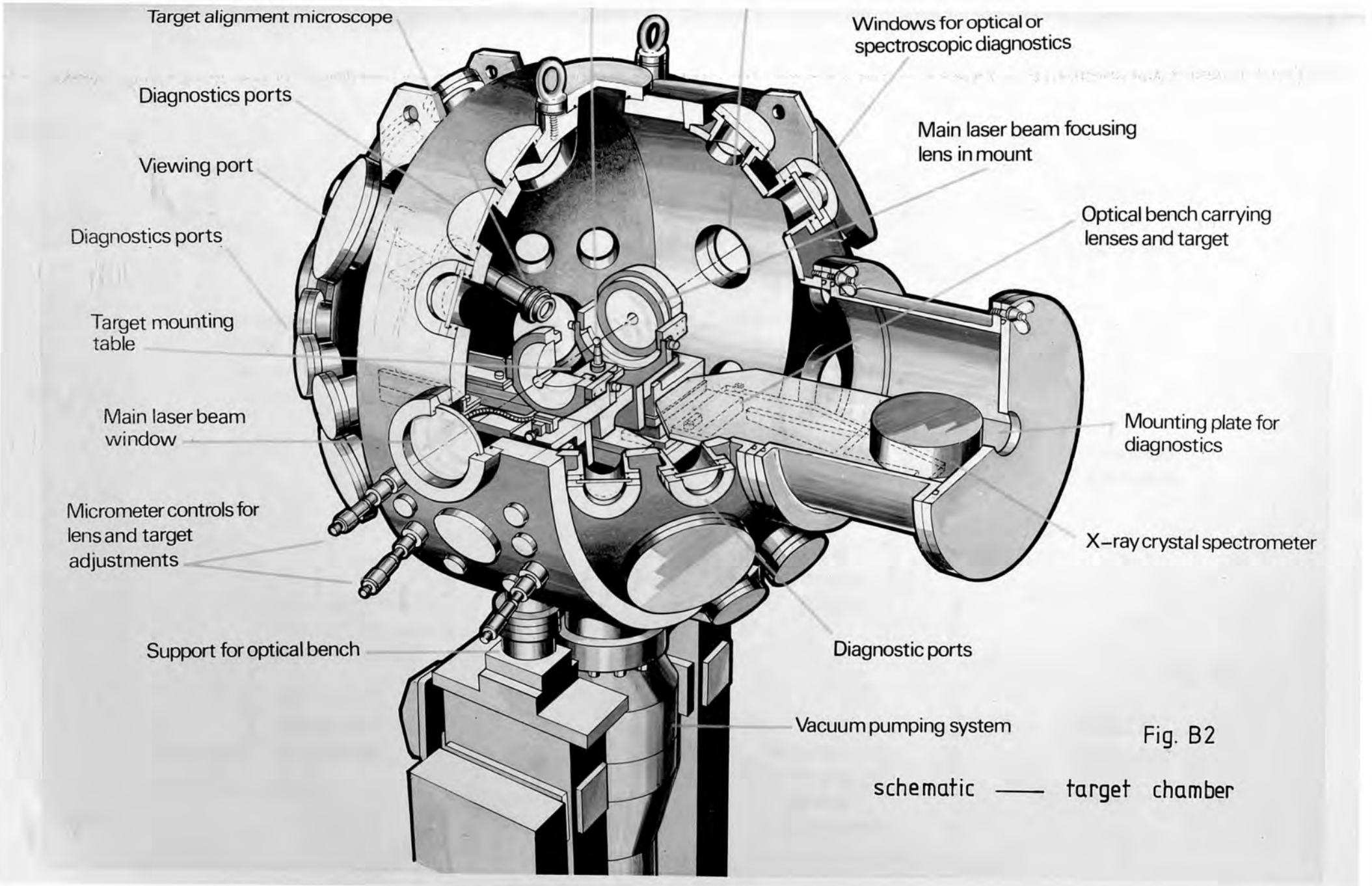

Fig. B2

schematic —— target chamber

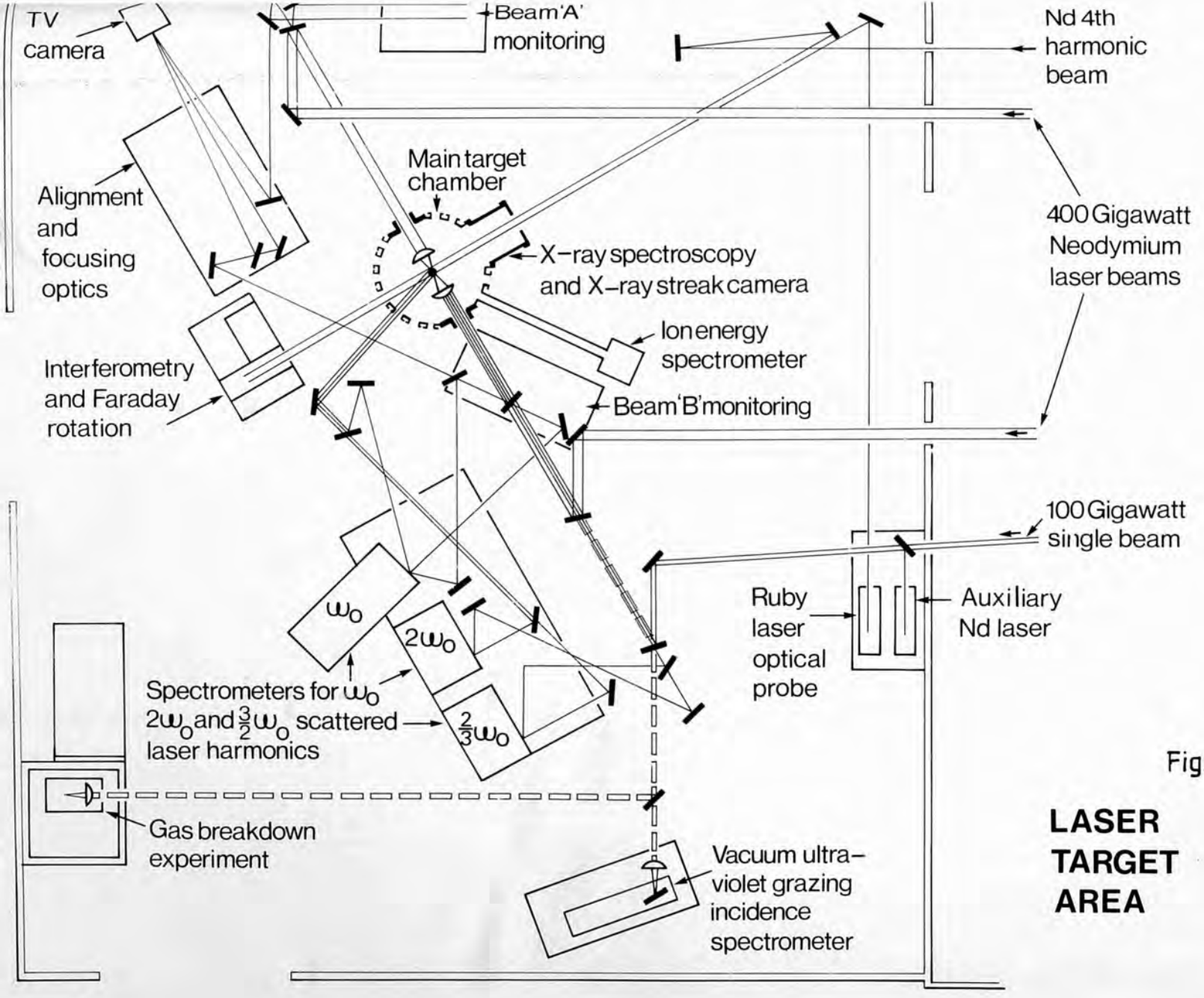

Fig. B3

LASER TARGET AREA

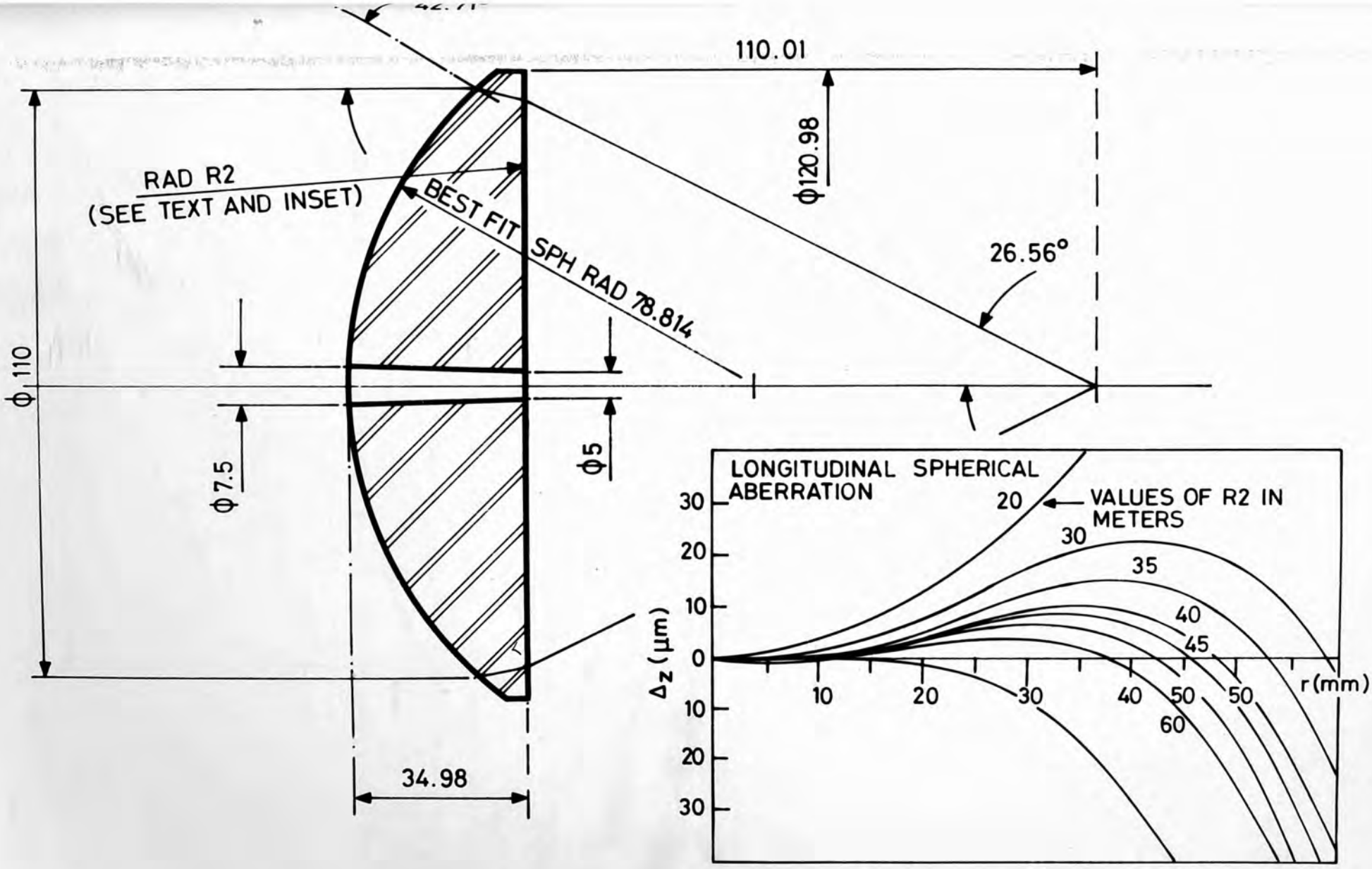

Fig. B4 schematic — SORO lens

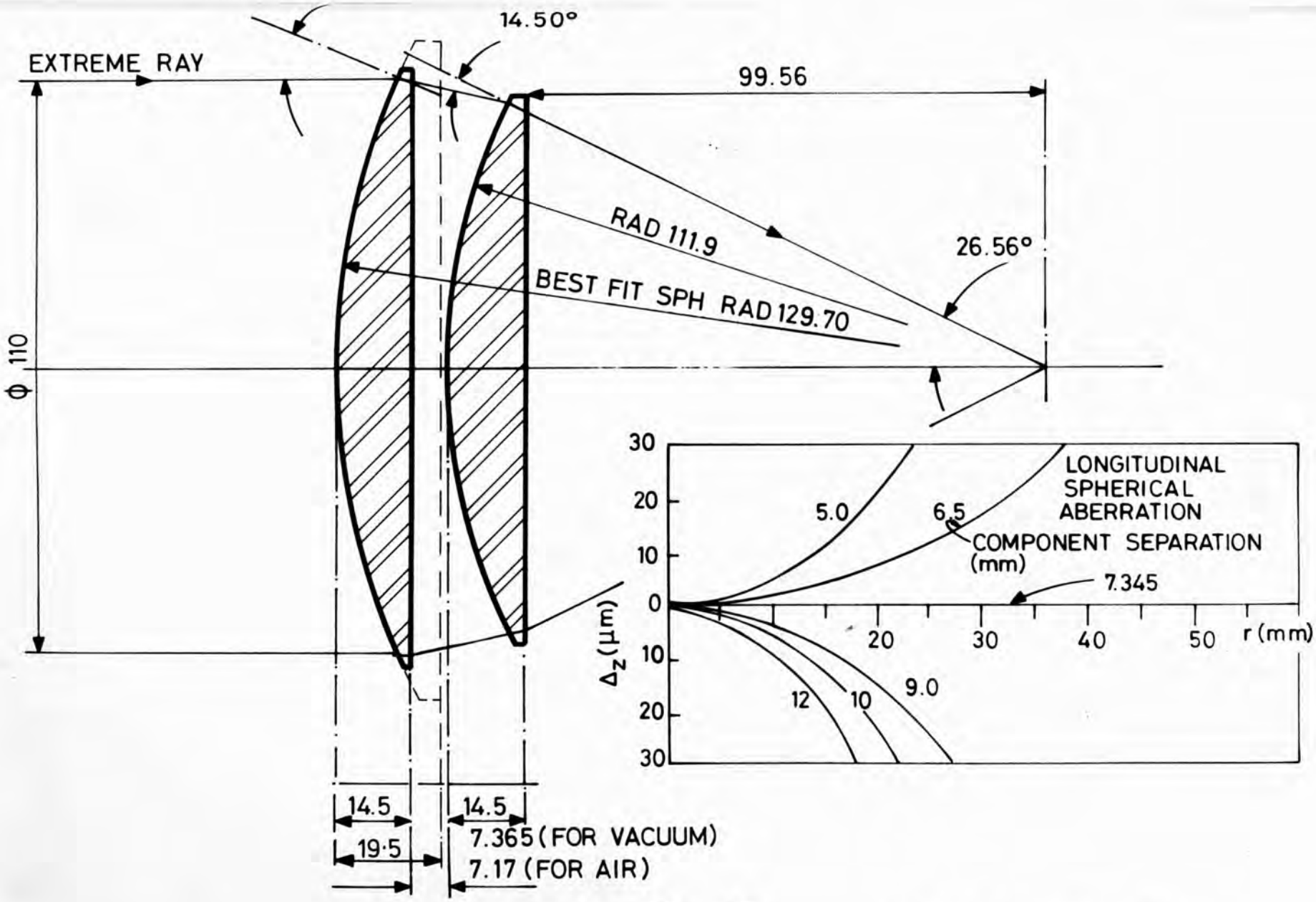

Fig. B5 schematic — ICOS lens

Nomenclature.

SI (MKS) units unless otherwise stated.

A – Mass No.

Å – Ångstrom (10^{-10} m)

B – magnetic flux density

c – velocity of e-m wave in vacuo

c_s – ion sound speed

D – 1. displacement vector, 2. determinant

e – electronic charge

E_o or E_i – peak electric field of incident laser beam

f – thermal flux limit, $(0 < f < 1)$

F – ponderomotive force

G – parameter defined in equation 3.2.3

h – Plancks constant

$\hbar$ – " " $/2\pi$

H_o – peak magnetic field

i – $\sqrt{-1}$

I – intensity, (I_o = peak intensity)

Im, – imaginary

I_ω – spectral intensity

J – current density

k – wave number

k_a – linear absorption coefficient

k_B – Boltzmann's constant ($J.ev^{-1}$)

k_s or $k_{3/2}$ – scattered $3/2\omega_o$ wave number

k_o – incident laser wave number

K – either: 1. phase mismatch,
2. imaginary part of complex refractive index,
3. parameter used in equation 5.2.6.
4. constant of an optical ray, $= \mu r \sin\Theta$

K_e – coefficient of electron thermal conduction

L_n – linear density scalelength

$m_{e,i}$ – electron (ion) mass

$n_{e,i}$ – electron (ion) density, ($no.cm^{-3}$)

Nd – neodymium (w.r.t. Nd doped glass or YAG as a lasing medium)

q – $(k_o L_n)^{2/3} \sin^2\Theta$

Q – thermal flux across unit area, or a boundary

r – radial distance

r_o – initial radius

Re – real; as opposed to imaginary

s – length of arc of a ray

S – optical path

$T_{e,i}$ – electron (ion) temperature, (eV)

u_o – peak amplitude of electron oscillating in an electric field

v_o – " velocity " " " " " " "

v_e or v_{th} – electron thermal velocity

v_{ph} – phase velocity

x – horizontal dimension

y – vertical dimension

z – horizontal dimension along axis of irradiation

Z – Effective charge

Greek.

$\beta - \sqrt{3\ v_e/c}$

γ – growth rate

δ, Δ – as prefix = small increment, or width, respectively

ε_o – permittivity of free space

ε_t – dielectric constant, (subscript 't' is that of a transverse wave)

θ – angle

λ_o – wavelength of incident laser

λ_s – Debye shielding distance, $= (\varepsilon_o k_s T_e / n_e e^2)^{1/2}$

Λ – Spitzers coefficient, $= \bar{n}/p_o$ where p_o is the value of the impact parameter such that deflection in the orbital plane is 90°

μ – real part of complex refractive index

μ_c – complex refractive index

μ_o – permeability of free space

ν_{ei} – electron ion collision frequency

$\nu_{ed,id}$ – electron (ion) wave damping rate

ρ_q – charge density

σ – conductivity

$\tau = \sqrt{q} = (k_o L_n)^{1/3} \sin\theta$

ϕ – angle, $\phi(\tau)$ – function in Fig.2.3.1

ω_o – angular frequency of incident laser light

$\omega_{pe,pi}$ – electron (ion) plasma frequency

Reprinted from:

OPTICS COMMUNICATIONS

Volume 27, No. 3, December 1978

TIME RESOLVED SPECTROSCOPY OF SECOND HARMONIC EMISSION FROM LASER IRRADIATED MICROBALLOONS

P.D. CARTER and S.M.L. SIM
Dept. of Physics, Royal Holloway College, University of London, Egham, Surrey, TW20 OEX, UK

T.P. HUGHES
Dept. of Physics, University of Essex, Colchester, Essex, CO4 3SQ, UK

pp. 423–425

NORTH-HOLLAND PUBLISHING COMPANY–AMSTERDAM

TIME RESOLVED SPECTROSCOPY OF SECOND HARMONIC EMISSION FROM LASER IRRADIATED MICROBALLOONS

P.D. CARTER and S.M.L. SIM
Dept. of Physics, Royal Holloway College, University of London, Egham, Surrey, TW20 OEX, UK

T.P. HUGHES
Dept. of Physics, University of Essex, Colchester, Essex, CO4 3SQ, UK

Received 25 August 1978

Time resolved second harmonic spectra from glass microballoons irradiated by neodymium laser pulses ($\sim 10^{16}$ W cm^{-2}, $\sim$ 100 ps) have been recorded with a resolution of $\sim$ 10 ps in time, $\sim$ 1 Å in wavelength and $\sim$ 10 μm in the target plane. Intense, time and wavelength resolution-limited spots appear, whose origin has not yet been explained.

Observations of spectrally and spatially resolved econd harmonic emission from laser produced plasnas have been reported by several authors [1–6]. These have provided information about possible interction processes and have been used to determine denity scale lengths near the critical surface. Time resolvd backscattered emission studies have also been reorted [7,8]. We present here time resolved observaions, with a spectral resolution of ~1 Å and temporal esolution of ~10 ps, of the spectrum of radiation mitted near the second harmonic wavelength from lasmas produced by two opposing Nd laser beams $I_0 \sim 10^{16}$ W cm^{-2} $\Delta t \sim 100$ ps) incident on D-T illed glass microballoon targets.

From earlier work [9], a typical time integrated econd harmonic system is shown in fig. 1, with a redhifted peak and asymmetric broadening mainly to the ed. The total width is approximately 30 Å. The radiaion was collected by one of the $f/1$ singlet lenses used o focus laser light on the target, and relay lenses proluced a magnified image on the slit of the 0.5 m gratng spectrograph. The limited solid angle illuminating he 1200 line mm^{-1} grating restricted the spectral reolution to about 0.3 Å.

To study the evolution of the spectrum in time, an lectrophotonics Photochron II streak camera with an -20 photocathode was optically coupled to the out-

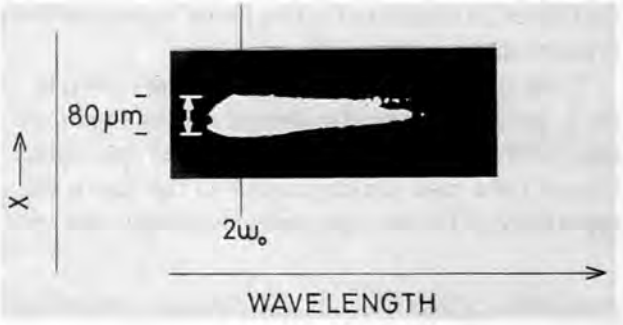

Fig. 1. Typical time integrated second harmonic spectrum $\Delta\lambda \sim 30$ Å.

put plane of the spectrograph, as shown in fig. 2. The singlet lenses were replaced with aspheric focussing doublet types. The size of the image on the spectrograph entrance slit was further increased which reduced the spectral resolution to ~1 Å, but gave good time resolution: although the time resolution of the camera alone (~5 ps) was determined by the camera entrance slit width, that of the entire system was limited by the range of path lengths in the spectrograph to 10 ps. The spatial resolution in the target plane was limited by the $f/1$ lens to about 10 μm at 5320 Å. The streak data were recorded photographically on Kodak type 2485 film. Separate exposures of the 5461 Hg I line

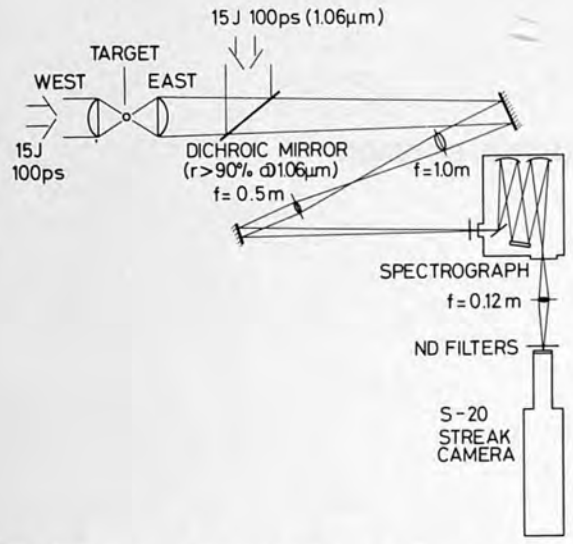

Fig. 2. Experimental layout for time resolved studies.

were taken with the spectrograph at different wavelength settings to define accurately both wavelength and dispersion. The temporal calibration was made using an air-gap etalon with 50% and 100% mirror reflectivities, in conjuction with a mode locked dye laser in an auxiliary experiment.

Three typical time resolved spectra are shown in fig. 3. They display similar spectral widths and broadening to those seen in the time integrated spectrum. However, the most striking feature of the data is the appearance of intense, spectrally and temporally resolution-limited, emission spots in the $(t\lambda)$ plane. The majority of the intense spots lie in a region corresponding to a small blue shift (~ -4 Å). (There is some tentative indication that regular patterns of spots occur.)

The results are open to various interpretations. Existence of the spots cannot simply be attributed to Doppler shifts unless the plasma flow is oscillatory due to some hydrodynamic instability. Such an instability may be produced by the ablation flow across the density step, at critical density produced by the ponderomotive force of the laser beam. Another explanation for the pulsed second harmonic emission is that individual plasma waves grow on picosecond timescales and saturate by "wave breaking", producing fast electrons [10]. The fast electrons may then modify the plasma dielectric function and change the plasmon frequency for a constant density and wave number, thus shifting the second harmonic emission frequency. The observations might also be due to spatial motion of several descrete emitting regions through the source area observed, with a speed $\gtrsim 10^8$ cm s^{-1}; or to rapid variations in the direction of emission in a narrow pencil from a stationary source, possibly associated with rippling of the critical density surface [11].

The authors are grateful to the Science Research Council for support and for the use of the Rutherford Laboratory Laser Facility. They would also like to thank Dr. R.G. Evans for valuable discussions, Dr. E.

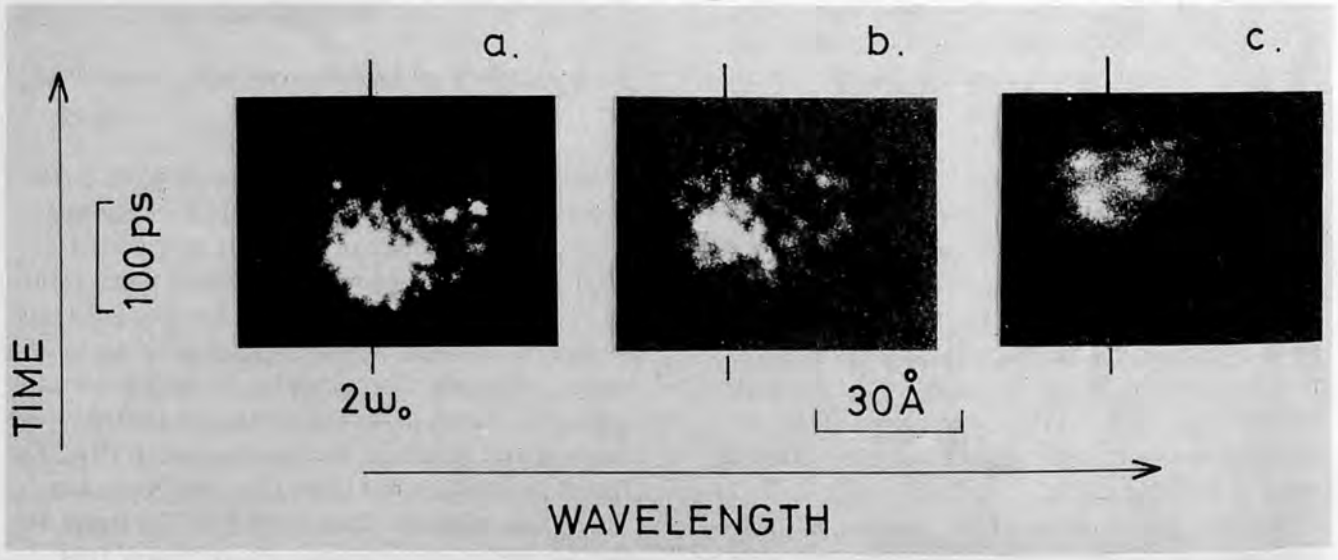

Fig. 3. Typical time resolved second harmonic spectra showing resolution limited emission "spots".

R. Wooding for guidance and other members of the Rutherford Laboratory Laser Division for assistance with the experiments.

References

[1] J.L. Bobin, M. Decroisette, B. Meyer and Y. Vitel, Phys. Rev. Lett. 30 (1973) 594.
[2] S. Jackel, B. Perry and M. Lubin, Phys. Rev. Lett. 37 (1976) 95.
[3] O.N. Krokhin et al., JETP Lett. 27 (1975) no. 1.
[4] E.A. McLean, J.A. Stamper, B.H. Ripin, H.R. Griem, J.M. McMahon and S.E. Bodner, Appl. Phys. lett. 31 (1977) 12.
[5] K. Eidman and R. Sigel, Phys. Rev. Lett. 34 (1975) 799.
[6] C. Yamanaka, T. Yamanaka, T. Sasaki, J. Mizui and H.B. Kang, Phys. Rev. Lett. 32 (1974) 1038.
[7] B.H. Ripin, J.M. McMahon, E.A. McLean, W.M. Manheimer and J.A. Stamper, Phys. Rev. Lett. 33 (1974) 634.
[8] V.Yu. Bychenkov et al., JETP Lett. 26 (1977) no. 6.
[9] SRC, Rutherford Laboratory report LD/78/04.
[10] J. Albritton and P. Koch, Phys. Fluids 18 (1975) 1136.
[11] R.A. Cairns, private communication.

Reprinted from:

OPTICS COMMUNICATIONS

Volume 32, No. 3, March 1980

MECHANISMS FOR THREE-HALVES HARMONIC EMISSION FROM LASER-PRODUCED PLASMA

P.D. CARTER *, S.M.L. SIM and E.R. WOODING

Department of Physics, Royal Holloway College, University of London, Egham, Surrey TW20 0EX, UK

pp. 443–446

NORTH-HOLLAND PUBLISHING COMPANY - AMSTERDAM

MECHANISMS FOR THREE-HALVES HARMONIC EMISSION FROM LASER-PRODUCED PLASMA

P.D. CARTER *, S.M.L. SIM and E.R. WOODING
Department of Physics, Royal Holloway College, University of London, Egham, Surrey TW20 0EX, UK

Received 14 May 1979
Revised manuscript received 19 October 1979

Three halves harmonic emission from thin foil targets irradiated with high power ($>10^{16}$ W cm^{-2}) Nd laser pulses is reported. Spectral differences between forward and backscattered $3\omega_0/2$ emission are seen, explained by plasmon/photon and three plasmon recombination.

Parametric processes are expected to play an important role in the collisionless absorption of high intensity laser radiation incident upon plasma, particularly with regard to current pellet-fusion schemes [1–4]. These processes are characterised by a threshold, determined by damping and loss due to convection and non-wave matching in inhomogeneous plasma. On exceeding this threshold various plasma wave phenomena can grow from thermal noise giving rise to stimulated scattering or collisionless absorption of the incident wave. One such process is the two-plasmon ($2\omega_{pe}$) instability, where the incident wave "decays" into two electron plasma waves of nominally half the angular frequency of the laser light [5,6], viz.

$$\omega_0 \rightarrow \tfrac{1}{2}\omega_0 + \tfrac{1}{2}\omega_0, \qquad t \rightarrow \ell + \ell,$$

where t denotes a transverse wave and ℓ a longitudinal plasma wave.

This process is of interest since it occurs at an electron density corresponding to a quarter of that where the local plasma frequency equals the laser frequency ($\omega_{pe} = \omega_0$), and can absorb energy before it reaches this critical surface.

The production of harmonic emission from laser-produced plasmas occurring at three halves the incident laser frequency ($\frac{3}{2}\omega_0$) observed in several experiments [7–9] may be directly attributed to the two-plasmon instability. As suggested by Avrov et al. [10], plasma waves of frequency $\frac{1}{2}\omega_0$ may recombine in two ways to generate emission around $\frac{3}{2}\omega_0$. Either three plasmas may coalesce amongst themselves, or alternatively a single plasmon may recombine with an incident photon to give a similar $\frac{3}{2}\omega_0$ photon either,

$$\tfrac{1}{2}\omega_0 + \tfrac{1}{2}\omega_0 + \tfrac{1}{2}\omega_0 \rightarrow \tfrac{3}{2}\omega_0, \qquad \ell + \ell + \ell \rightarrow t', \qquad (1)$$

or

$$\omega_0 + \tfrac{1}{2}\omega_0 \rightarrow \tfrac{3}{2}\omega_0, \qquad t + \ell \rightarrow t'. \qquad (2)$$

If these two schemes are responsible then it is also shown that each one will give rise to a different spectrum. These two different spectra are independent of laser intensity, but are dependent upon the angle (θ) between the incident laser wave-vector and the direction of observation. Plasmon photon recombination will produce a spectrum with two sidebands of equal intensity and equally shifted to the blue and red directions of the true harmonic frequency. The spectral difference between these two wings is a maximum when θ = either θ° or 180° since

$$\delta\lambda_{3/2}^{\ell t} \simeq \pm 2.04 \times 10^{-3}\, \lambda_0 T_e \cos\theta,$$

where $\delta\lambda$ is the wavelength shift from $\frac{3}{2}\omega_0$ in metres, λ_0 is the incident wavelength in metres and T_e is the electron temperature in keV.

For the three-plasmon recombination however, two

* Present address: Materials Physics Division, AERE Harwell, Didcot, Oxon OX11 0RA, UK.

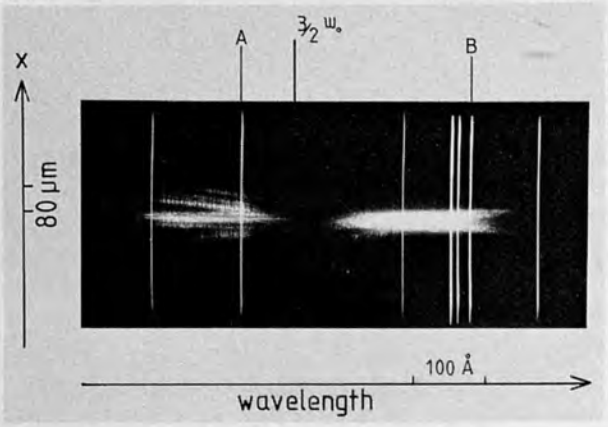

Fig. 1. $\frac{3}{2}\omega_0$ spectrum for 80 μm diameter microballoon target ($E_i \sim 15$ J, $\Delta t \sim 100$ ps) displaying red and blue shifted satellites. Calibration lines from Hg/Cd/Zn lamp. Effective wavelengths: A – 7017.24 Å; B – 7326.56 Å; C – 7070.9 Å (fig. 3 only).

sidebands of equal intensity are also produced except that the red-shifted one is backscattered ($90° < \theta° < 180°$) whereas the blue-shifted one is forward scattered ($0° < \theta° < 90°$), since for this mechanism

$$\delta\lambda_{3/2}^{3\ell} \simeq 2.13 \times 10^3 \lambda_0 T_e \cos\theta.$$

At the laser intensities used in our experiments, the latter process is expected to predominate, and an experimentally obtained $\frac{3}{2}\omega_0$ spectra obtained in backscatter from a microballoon target ($I_0 > 10^{16}$ W cm^{-2}) appears in fig. 1. The laser energy was $\simeq 15$ Joule in a 100 ps pulse (fwhm). This spectrum clearly shows two peaks, one red-shifted and the other blue shifted. However, the blue wing is far less intense than the red since in being forward scattered, it is reflected from its own critical surface ($\frac{9}{4}n_{cr}$ with respect to the incident laser) and returns, encountering absorption as it does so.

To add further weight to this theory, an experiment was performed where the target was a thin (0.08–1.0 μm) foil of polystyrene. During irradiation, the laser light will "burn through" the plasma formed from the foil and this means that a peak electron density greater than $\frac{9}{4}n_{cr}$ cannot exist for long after the plasma is formed, since it becomes underdense rapidly. Hence observation of the $\frac{3}{2}\omega_0$ emission in the forward

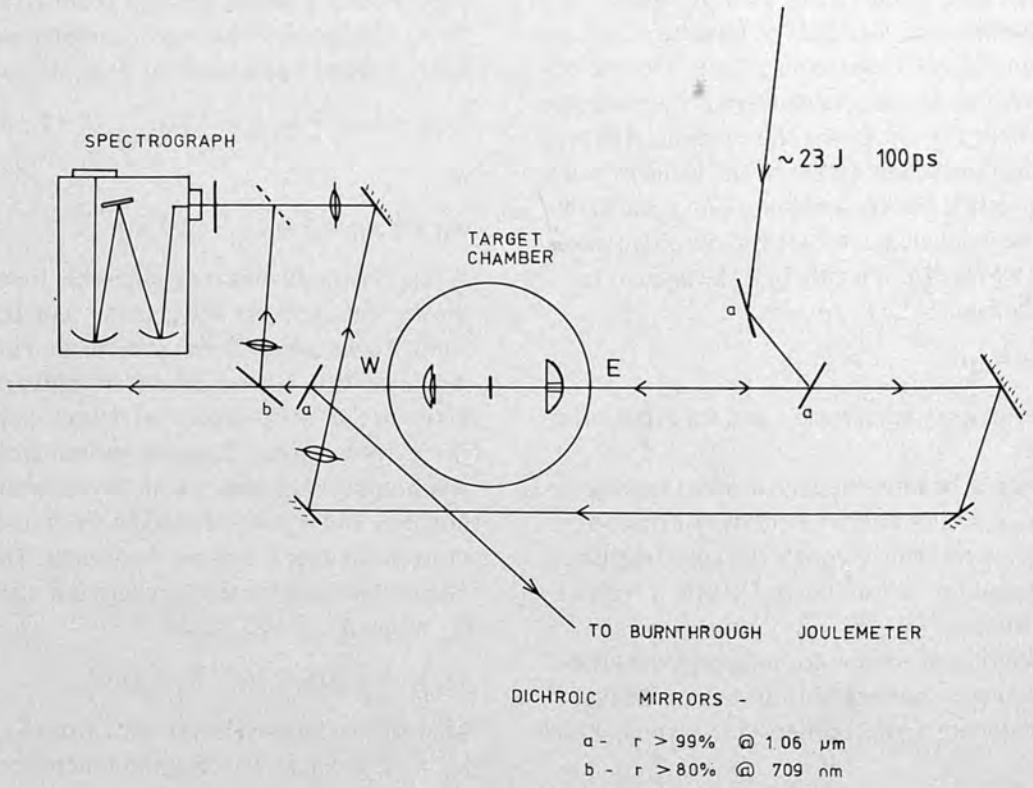

Fig. 2. Experimental arrangement for viewing forward and backward $\frac{3}{2}\omega_0$ emission from a thin foil target.

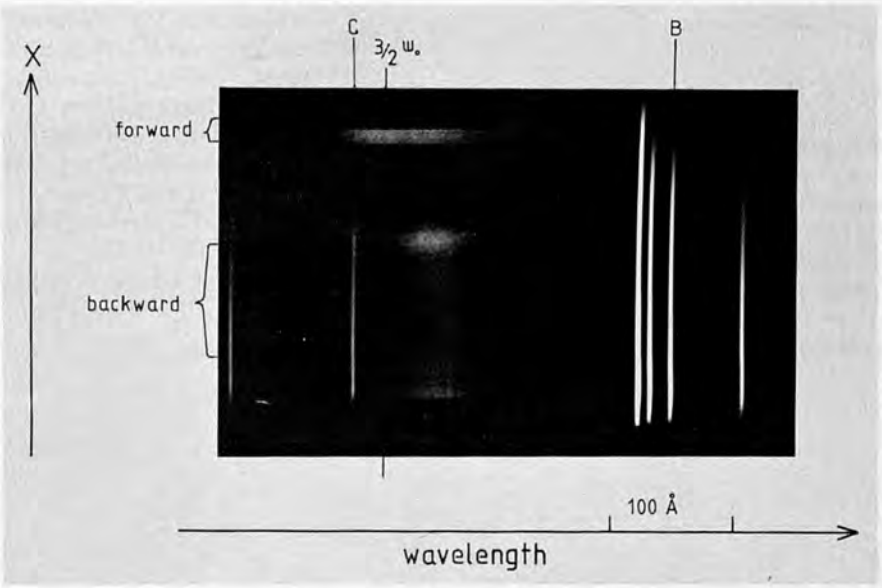

Fig. 3. Typical forward and backscattered $\frac{3}{2}\omega_0$ spectra from a 0.4 μm polystyrene foil target ($E_i \sim 24$ J, $\Delta t \sim 100$ ps).

direction should be possible. In the actual experiment, both the forward and backward directions were viewed simultaneously, and resolved on the same spectrograph, the experimental arrangement appearing in fig. 2. Dichroic mirrors were used to deflect the incident laser beam whilst at the same time remaining transmissive to light of optical wavelengths. A similar mirror reflected the remaining laser energy upon "burnthrough" to avoid damage to subsequent optics.

Spectra obtained from several thin foil targets showed that both red and blue shifted wings appear in both directions, a typical result being shown in fig. 3. However in the forward direction an almost continuous spectrum, rather than a double peaked spectrum, is observed. In general the blue shifted side was always of similar intensity to the red side and was often of greater intensity than the red. In the backward direction, allowing for chromatic aberration, the blue wing is barely detectable so that the ratio of blue wing intensity/red wing intensity is far less than that previously seen with massive targets, where a $\frac{9}{4}n_{cr}$ surface exists throughout the laser pulse duration. From Avrov, the relative intensity ratio of total $\frac{3}{2}\omega_0$ emission due to three-plasmon and plasmon-photon recombination is greater than 6×10^3; hence with the dynamic range of the recording film, three plasmon recombination is expected to be the only mechanism responsible for the observed emission. Electron temperatures determined from the peak-to-peak spectral width, due to this process, show a high value of ~6 keV for the backscattered spectrum, from a massive target, in fig. 1, whereas that deduced from the forward scattered spectrum in fig. 3 of ~1.6 keV is closer to the value of ~0.9 keV determined from X-ray absorber-foil data. So in essence, the agreement between the theory of generation of $\frac{3}{2}\omega_0$ emission by recombination of three plasmons and the corresponding observed spectra is fair, with regard for the necessity of low f/no lenses to achieve the high irradiance required. The f/1 lenses used had a collection angle of ±26.6° so that angular resolution was low. However, a previous experiment [11] performed with an underdense performed plasma heated with a CO_2 laser has also shown only a detectable red shifted wing from $\frac{3}{2}\omega_0$ emission in the backward direction.

The authors gratefully acknowledge the assistance of the staff of the Central Laser Facility and the support of the Science Research Council. They also thank Dr. R.G. Evans for helpful discussions.

Accepted for publication in Physical Review Letters

Time Resolved Observations of the Three-Halves Harmonic Spectrum from Laser-Produced Plasmas

P D Carter and S M L Sim

Dept of Physics, Royal Holloway College, University of London
Egham, Surrey, TW20 OEX, UK

H C Barr

School of Mathematics and Computer Science, University College
of North Wales, Bangor, Gwynedd, LL57 2DG

R G Evans

Rutherford Laboratory, Chilton, Didcot, Oxon OX11 OQX

Abstract

Time resolved 3/2 ω_o spectra from glass microballoons irradiated by 100 ps, 2×10^{16} W cm^{-2} laser pulses have been obtained with a temporal resolution of 20 ps and a spectral resolution of 15 Å. Pulsed emission is observed, with a pulse duration of less than the instrument limit. Both red and blue peaks appear simultaneously with their separation varying in time.

Figures 1, 2 and 3 are similar to

Figures 6.4.1, 6.5.1a, and 6.5.1c respectively.

Time Resolved Observations of the 3/2 ω_o Spectrum in a Laser Produced Plasma

In recent years much theoretical and experimental work has been performed to study the various parametric processes which occur in laser produced plasmas at high irradiances. At the quarter critical density both stimulated Raman scattering[1] and the two plasmon decay[2] can occur, and either of these can give rise to the emission of radiation at 3/2 ω_o. These instabilities at quarter critical density are probably not very important for the overall absorption of laser energy by the plasma[3], but may be responsible for the production of a significant number of fast electrons[4].

Previous observations of the 3/2 ω_o emission have been of time integrated spectra[3,5] or of the time resolved intensity[6,7]. Bychenkov et al[8] have obtained time resolved spectra with a long laser pulse and time resolution of 100 ps. We present here new observations of the time resolved spectra with high time resolution of ∿20 ps and simultaneous spectral resolution of 30 Å. The measurements were made with the Rutherford Laboratory Nd glass laser facility providing an irradiance of 2×10^{16} W cm^{-2} in a 100 ps pulse on glass microballoon targets of 50 - 90 μm diameter.

The experimental layout is shown in Fig 1. The backscattered 3/2 ω_o was collected by the F1 doublet lens, used to focus the laser light on the target. This lens produced a 60X magnified image at 3/2 ω_o on the slit of the 0.5 m, 600 line mm^{-1} grating spectrograph, the slit size of 1 mm restricted the spectral resolution to about 15 Å. The output plane of the spectrograph was then optically coupled to a Hadland Photonics streak camera fitted with an S-20 photocathode, using a dove prism to rotate the image so that wavelength would be dispersed along the streak camera slit.

Although the time resolution of the streak camera alone (∿5ps) was determined by its entrance slit width, that of the entire system was limited by the range of path lengths in the spectrometer to ∿20 ps. Photographic recordings of the streak data were made on Kodak 2485 film and separate exposures of the 5461 Å Hg I line were taken with the spectrograph at different wavelength settings to calibrate both wavelength dispersion. The sweep speed of the streak camera was calibrated in an auxiliary experiment using a mode locked dye laser and an air gap etalon with 70% mirror reflectivities.

Two typical time resolved spectra are shown in Fig 2. Both spectral streaks show that the 3/2 ω_o harmonic emission has a pulsed nature, where the duration of the pulses is less than the ∿20 ps temporal resolution of the system, with the spectrograph in second order. (Spectra showing resolution

limited bursts of <10 ps were obtained with the spectrograph in first order).

The blue-shifted and red-shifted peaks appear simultaneously but with their separation varying in time. Spectra with monotonically decreasing separation (Fig 2a) were obtained when the laser prepulse level was low ($< 10^{-5}$ times the main pulse energy) while spectra showing an increasing and then decreasing separation (Fig 2b) occurred as a result of larger prepulse levels. The blue shifted peaks appear more intense than the red shifted peaks which is the reverse of the time integrated observations[3,5]. This is probably due to the spectral response of the S-20 photocathode which falls off rapidly in the red near 7093 Å and may also be accentuated by any error between the direction of spectral dispersion and the slit of the streak camera.

The spectrum of the 3/2 ω_o emission has been calculated by Avrov[9] and by Barr[10]. The Barr theory differs from Avrov's theory in that Avrov neglects the wave number k_o of the pump wave, compared with the wave k number of the plasma waves, while Barr makes no such assumption. For the conditions of our experiment plasma waves with $k >> k_o$ are strongly Landau damped so that the Avrov theory is not applicable.

The Barr theory considers three mechanisms for the production of $3/2\omega_o$ radiation: combination of three plasma waves, combination of a plasmon with an incident pump photon or combination of a plasmon with a pump photon reflected from critical density. If only plasma waves with $\underline{k}$ close to the fastest growing mode are considered then the dominant contributions to our backscatter spectra will rise from the combination of the reflected pump wave and the plasma waves. The frequency shift of the 3/2 ω_o radiation arises from the Bohm Gross correction to the plasma frequency and is always proportional to T_e the electron temperature. For the modes of maximum growth rate the wavelength shifts of 3/2 ω_o are $\Delta\lambda_R = 19.0\ T_e$, $\Delta\lambda_B = -29.8\ T_e$, with T_e in keV and $\Delta\lambda$ in Å. For 3/2 ω_o radiation close to the laser axis $\Delta\lambda_R = 23.3\ T_e$ and $\Delta\lambda_B = -44.3\ T_e$. We have also considered the effects of Brillouin shifted reflection of the pump wave and of Doppler shifts due to the motion of the quarter critical region. These are much less than the observed shift of the $3/2\omega_o$ radiation, being of order 10Å - 20Å. Moreover the Brillouin shift is reduced to zero if the expansion of the plasma is at the sound speed.

The spectra presented here show a fairly symmetrical shift of the red and blue wings with a slightly larger shift to the red. We feel that the discrepancy between this and the simple theory may be due to rippling[11] of

either the critical or quarter critical surfaces giving rise to an uncertainty in the angular relationship of the plasma waves and electromagnetic waves. Also the Barr theory has assumed that the nine-fourths critical density layer is parallel to the quarter critical surface and this may not be the case.

The differences between the spectra of Fig 2a and Fig 2b can be explained on the assumption that the splitting of red and blue wings is proportional to the electron temperature. The threshold for two plasmon decay[2] is $(v_o/v_e)^2 k_o L > 44$ where v_o is the electron oscillatory velocity in the pump field, v_e is the electron thermal velocity, k_o is the wavenumber of the pump and L is the density scale length at quarter critical. For laser light of wavelength 1.06μm this gives $\phi(Wcm^{-2}) > \frac{2.3 \times 10^{16} T_e (keV)}{L(\mu)}$. In the case of small laser prepulse the density scale length during the rising half of the laser pulse is very small and the threshold for the two plasmon decay is exceeded only after the peak of the laser pulse as the density scale length increases. The decreasing separation of the red and blue peaks is then a reflection of the decreasing electron temperature during the falling part of the laser pulse. With a significant prepulse the initial density scale lengths are longer and threshold is exceeded earlier. The spectral separation then follows the rise and fall of electron temperature with the laser irradiance.

It may be that the pulsed nature of the 3/2 ω_o emission is due to density profile modifications caused by the pondermotive force of the plasma waves. Profile modification at the quarter critical density surface has been observed by interferometry[12] and predicted in plasma simulations[11]. Bursts of $3/2\omega_o$ emission have also been predicted from plasma simulations by Langdon and Lasinski[4] but in their simulations the bursts occurred with a period of about 0.8ps for the case of a realistic electron-ion mass ratio.

We believe that there is an alternative explanation of the bursts of $3/2\omega_o$ emission since identical temporal behaviour has been observed in $2\omega_o$ time resolved spectra[13]. There appears to be no reason why different parametric instabilities at different electron densities should be related except for the hydrodynamic expansion of the plasma. If the plasma flow across the steepened density profile[14] at the critical surface is unstable, then these density fluctuations will propagate outwards through quarter critical. Both $2\omega_o$ emission (near critical density) and 3/2 ω_o emission will thus be affected. The time scale of such a hydrodynamic instability is expected to be about

either the critical or quarter critical surfaces giving rise to an uncertainty in the angular relationship of the plasma waves and electromagnetic waves. Also the Barr theory has assumed that the nine-fourths critical density layer is parallel to the quarter critical surface and this may not be the case.

The differences between the spectra of Fig 2a and Fig 2b can be explained on the assumption that the splitting of red and blue wings is proportional to the electron temperature. The threshold for two plasmon decay[2] is $(v_o/v_e)^2 k_o L > 44$ where v_o is the electron oscillatory velocity in the pump field, v_e is the electron thermal velocity, k_o is the wavenumber of the pump and L is the density scale length at quarter critical. For laser light of wavelength 1.06μm this gives $\phi(Wcm^{-2}) > \frac{2.3 \times 10^{16} T_e (keV)}{L(\mu)}$. In the case of small laser prepulse the density scale length during the rising half of the laser pulse is very small and the threshold for the two plasmon decay is exceeded only after the peak of the laser pulse as the density scale length increases. The decreasing separation of the red and blue peaks is then a reflection of the decreasing electron temperature during the falling part of the laser pulse. With a significant prepulse the initial density scale lengths are longer and threshold is exceeded earlier. The spectral separation then follows the rise and fall of electron temperature with the laser irradiance.

It may be that the pulsed nature of the 3/2 ω_o emission is due to density profile modifications caused by the pondermotive force of the plasma waves. Profile modification at the quarter critical density surface has been observed by interferometry[12] and predicted in plasma simulations[11]. Bursts of $3/2\omega_o$ emission have also been predicted from plasma simulations by Langdon and Lasinski[4] but in their simulations the bursts occurred with a period of about 0.8ps for the case of a realistic electron-ion mass ratio.

We believe that there is an alternative explanation of the bursts of $3/2\omega_o$ emission since identical temporal behaviour has been observed in $2\omega_o$ time resolved spectra[13]. There appears to be no reason why different parametric instabilities at different electron densities should be related except for the hydrodynamic expansion of the plasma. If the plasma flow across the steepened density profile[14] at the critical surface is unstable, then these density fluctuations will propagate outwards through quarter critical. Both $2\omega_o$ emission (near critical density) and 3/2 ω_o emission will thus be affected. The time scale of such a hydrodynamic instability is expected to be about

L/v_{ia} where L is the density scale length at critical density and v_{ia} is the ion sound speed. If we assume $L \sim 3$ μm and $v_{ia} \sim 3 \times 10^7$ cm s^{-1} then the time scale of the instability is $\sim$ 10 ps which is in approximate agreement with the observations.

Acknowledgements We gratefully acknowledge the assistance of the members of the Central Laser Facility at the Rutherford Laboratory in carrying out these observations. We also acknowledge the constructive criticism of one of the referees.

Figure Captions

Fig 1. Experimental layout for time resolved 3/2 ω_o spectra.

Fig 2 (a) 3/2 ω_o spectral streak showing decreasing separation (in time) between peaks: temporal resolution $\sim$ 20 ps, spectral resolution $\sim$ 15 Å. (Curvature is due to "pincushion" distortion in the image intensifier).

Fig 2 (b) 3/2 ω_o spectral streak showing increasing, then decreasing separation in time between peaks: temporal resolution $\sim$ 20 ps, spectral resolution $\sim$ 15 Å.

References

1. D Biskamp and H Welter, Phys. Rev. Lett. 34, 312 (1975)

2. C S Liu and M N Rosenbluth, Phys. Fluids 19, 967 (1976)

3. H C Pant, K Eidmann, P Sachsenmaier, and R Sigel, Opt. Comm. 16, 396 (1976)

4. A B Langdon, B F Lasinski and W L Kruer, Phys. Rev. Lett. 43, 2, 133 (1979)

5. J L Bobin, M Decroisette, B Meyer and Y Vitel, Phys. Rev. Lett. 30, 594 (1973)

6. T A Leonard and R A Cover, 1977 Annual Report on Laser Fusion Research
   K M S Fusion Inc. Section 2 p 23

7. S Jackel, B Perry, M Lubin, Phys. Rev. Lett. 37, 95 (1976)

8. V Yu Bychenkov, Yu A Zukhorenhov, O N Krokhin, A A Rapsov, V P Silin,
   G V Sklizkov, A N Starodub, V T Tikhonchuk, A S Shikanov,
   Soviet Phys. JETP LETT. 26, 364 (1977)

9. A I Avrov, V Yu Bychenkov, O N Krokhin, V V Purtavalov, S S Rupasov,
   V P Silin, G V Sklizkov, V T Tikhonchuk, A S Shikanov
   Soviet Phys. JETP 43, 507 (1977)

10. H C Barr, Rutherford Laboratory Report RL-79-036 Section 8.3.8 p 8.12

11. A B Langdon, B F Lasinski, Laser Program Annual Report (1975)
    Lawrence Livermore Laboratory Report UCRL 50021-75 p309 (1976)

12. H A Baldis, J C Sampson, P B Corkum, Phys. Rev. Lett, 41, 1718 (1978)

13. A J Cole, R G Evans, D Gray, J D Murdoch, S M L Sim and W T Toner
    Rutherford Laboratory Report RL-79-036, Section 3.4 03.16

14. C E Max and C F McKee, Phys Rev Lett 39, 1336 (1977)